QUANTUM DOT POLYMER COMPOSITE MATERIALS FOR LIGHT MANAGEMENT IN OPTOELECTRONIC DEVICES

BY

LU XU

DISSERTATION

Submitted in partial fulfillment of the requirements
for the degree of Doctor of Philosophy in Chemistry
in the Graduate College of the
University of Illinois at Urbana-Champaign, 2017

Urbana, Illinois

Doctoral Committee:

Professor, Ralph Nuzzo, Chair
Professor, Andrew Gewirth
Professor, Paul Braun
Assistant Professor, Joshua Vura-Weis

ABSTRACT

This dissertation will highlight a path to achieve high conversion efficiency of optoelectronic devices, including photovoltaic concentrators and LED display modules. Semiconductor nanocrystals, also known as quantum dots (QDs), serve as the pivotal luminescent materials in these devices. A quantum dots encapsulation method was developed here to homogeneously disperse QDs in a transparent polymer matrix, enabling high optical quality devices and thorough investigation of light material interactions.

A luminescent solar concentrator (LSC) typically consists of a luminophore embedded in a polymer sheet with a high-performance solar cell attached at the side. In such a device, sunlight is absorbed in a luminophore, emitted into the waveguide modes of the polymer sheet, and directed to a photovoltaic cell where it is absorbed and converted to electricity. Since the area of the polymer sheet is greater than the area of the photovoltaic cell, concentration of the solar photon flux is achieved. Approaching high concentration ratio will require a luminophore with large Stokes Shift, high quantum yield, minimal overlap between absorption and emission, and a narrow emission spectrum. We have examined the performance of LSCs utilizing CdSe/CdS core-shell QDs, with significantly reduced absorption-emission overlap and long propagation distances in the waveguide. Furthermore, a distributed Bragg reflector dramatically mitigates the negative impact of scattering in the waveguide, allowing efficient photon collection and concentration ratio.

White-light LED is achieved by using a phosphor material to convert monochromatic light from a blue or UV LED to broad-spectrum white light. However, tradition yellow phosphors suffer from low color rendering index due to the broad emission spectrum of the phosphors. QDs have been proposed as better candidate than traditional yellow phosphors due to their narrow and tunable emission spectrum, and wide absorption spectrum in the UV-blue spectrum range. We have fabricated QD-polymer thin films as color conversion layers on blue LED via different methods, including spin-coating, drop casting and electrohydrodynamic jet printing. The polymer surface has been incorporated with nano-sized features to create photonic crystal structure. Up to 8 times QD excitation and emission enhancement have been demonstrated. We have also designed and fabricated QD-polymer based concentrating cavity on blue LED that acts both as color conversion layer and light concentrator. Distributed Bragg reflector and sputtered silver have been used as reflectors surrounding QD-polymer thin film. The exterior of the concentrator cavity was coated with black absorber to suppress light reflection, and a small aperture in the center allows concentrated photons to exit. High power conversion efficiency and high ambient contrast have been achieved in module devices.

ACKNOWLEDGEMENTS

During my years at University of Illinois at Urbana-Champaign, I have received help and encouragement from many people, without whom the completion of this dissertation would impossible. I am expressing my sincerest gratitude to those who have helped me tremendously.

First of all, I would like to thank Professor Ralph Nuzzo, who guided me throughout the process of my research. I am grateful for his guidance and insight into problems, as well as a good role model of a motivated scientist. I am very thankful to Professor Paul Alivisatos and Professor Paul Braun, whom I collaborated with for a large portion of my dissertation work. I am grateful to Professor Andrew Gewirth and Professor Josh Vura-Weis, for serving on my final defense committee. I also want to thank Professor Catherine Murphy and Professor Angus Rockett for serving on my prelim committee.

I would like to thank my collaborators. I would like to thank Dr. Yuan Yao and Dr. Noah Bronstein, for working with me on the luminescent solar concentrator projects. I would like to thank Dr. Gloria See for working with me on the photonic crystal projects. I would like to thank Osman Cifci, for working with me on the concentrating cavity project. I would like to thank my labmates Junwen He and Makayla Anderson, for fabrication and testing of device modules, and further collaboration on the luminescent concentrator project. I would also like to thank the Nuzzo group members for their help, encouragement, company, and friendship.

Last but not least, I would like to direct my special thanks to my family and friends, for their love and support. I give my greatest gratitude to Yifei, for his love and support. I would like to thank my parents for raising me and supporting my decision to study aboard.

TABLE OF CONTENTS

CHAPTER 1: INTRODUCTION

This chapter introduces the motivation of employing Quantum Dots in various optoelectronic applications, and the necessity of encapsulating Quantum Dots in transparent polymer materials for light management in optoelectronic devices.

1.1 General introduction to quantum dots

Quantum dots (QDs) are very small semiconductor particles, usually several to tens of nanometers in size, so small that their optical and electronic properties differ from those of bulk particles. They were first discovered in 1980, and they have been a central theme in nanotechnology ever since. Many types of quantum dot will emit light of specific wavelength if electricity or light is applied to them, and the emission wavelength can be precisely tuned by changing the dots size, shape and material, giving rise to many applications.

A quantum dot gets its name because it is a tiny speck of matter so small that it is effectively concentrated into a single point. As a result, the particles inside it that carry electricity are trapped and have well-defined energy levels according to the laws of quantum theory, a bit like individual atoms. Quantum dots are also sometimes referred to as artificial atoms, a term that emphasizes that a quantum dot is a single object with bound, discrete electronic states, as is the case with naturally occurring atoms or molecules.[1] Tiny really does mean tiny: quantum dots are crystals a few nanometers wide, so they are typically a few dozen atoms across and contain anything from perhaps a hundred to a few thousand atoms. Quantum dots exhibit properties that are intermediate between those of bulk semiconductors and those of discrete molecules. Their optoelectronic properties change as a function of both size and shape. Larger QDs (radius of 5-6 nm, for example) emit longer wavelengths resulting in emission colors such as orange or red. Smaller QDs (radius of 2-3 nm, for example) emit shorter wavelengths resulting in colors like blue and green, although the specific colors and sizes vary depending on the exact composition of the QD (Figure 1.1).[2-3]

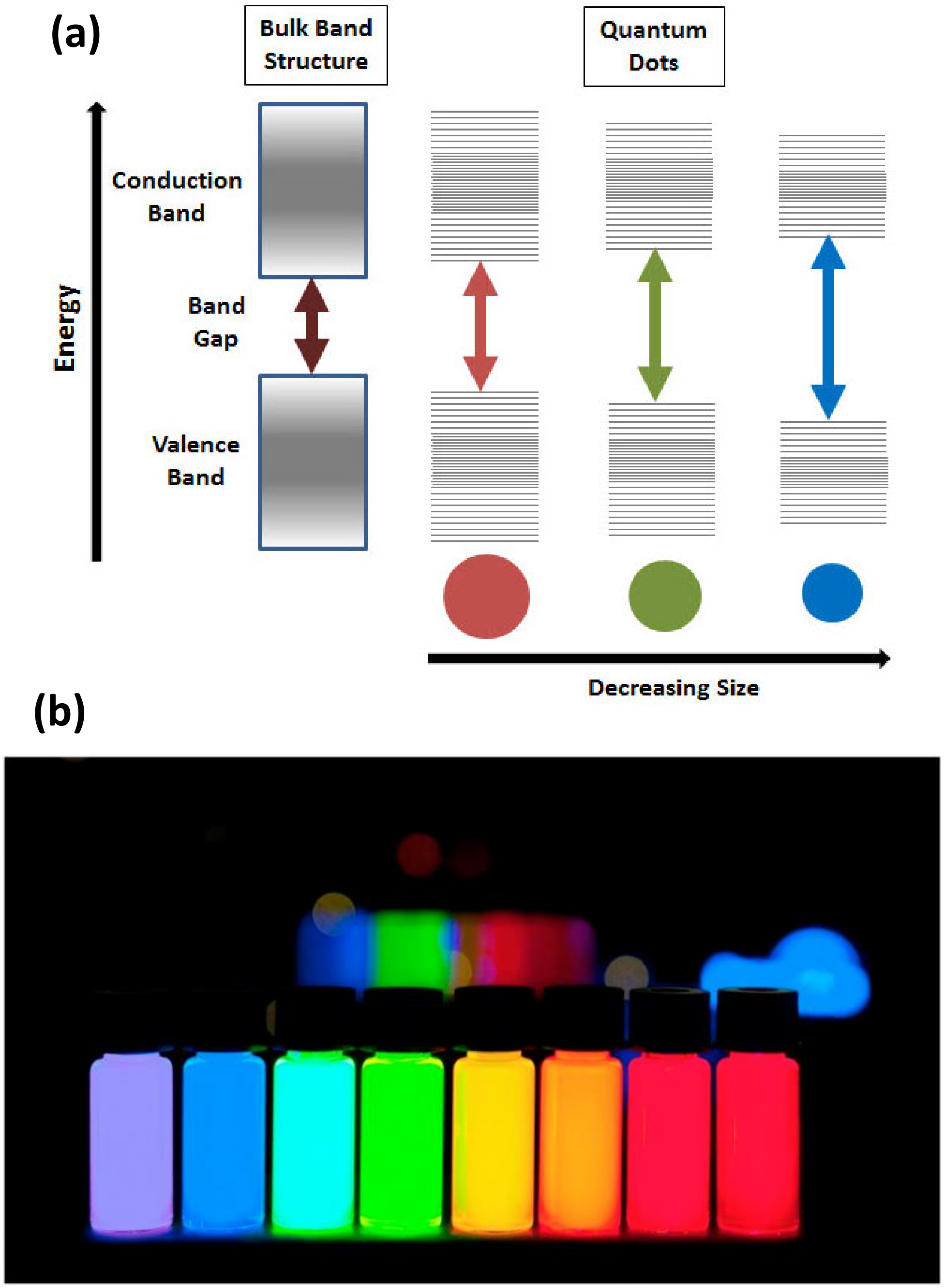

Figure 1.1

Figure 1.1 (cont.) (a) Illustration of energy levels splitting in quantum dots due to the quantum confinement effect, where semiconductor band gap increases with decrease in size of the nanocrystal. (b) Photograph of a series of quantum dots from violet to red color.

The luminescent properties of quantum dots arise from recombination of electron-hole pairs (exciton decay) through radiative pathways. However, the exciton decay can also occur through nonradiative methods, reducing the fluorescence quantum yield. One of the methods used to improve efficiency and brightness of semiconductor nanocrystals is growing shells of another higher band gap semiconducting material around them. These quantum dots with small regions of one material embedded in another with a wider band gap are known as core-shell quantum dots or core-shell semiconducting nanocrystals. Coating quantum dots with shells improves quantum yield by passivizing nonradiative recombination sites and also makes them more robust to processing conditions for various applications.[4-5]

1.2 Applications of quantum dots materials

The unique size and composition tunable electronic property of these very small, semiconducting quantum dots make them very appealing for a variety of applications and new technologies. Among them, quantum dots are particularly significant for optical applications owing to their bright, pure colors along with their ability to emit rainbow of colors coupled with their high efficiencies, longer lifetimes and high extinction coefficient. Examples include LEDs and solid state lighting, displays and photovoltaics.[6] Additionally, their small size allows for QDs to be suspended in solution which leads to possible uses in inkjet printing and spin-coating.[7]

Being zero dimensional, quantum dots have a sharper density of states than higher-dimensional structures. Their small size also means that electrons do not have to travel as far as with larger particles, thus electronic devices can operate faster. Examples of applications taking advantage of these unique electronic properties include transistors, solar cells, ultrafast all-optical switches and logic gates, and quantum computing, among many others.[8]

Furthermore, the small size of quantum dots allows them to go anywhere in the body making them suitable for different bio-medical applications like medical imaging, biosensors, etc. At present, fluorescence based biosensors depend on organic dyes with a broad spectral width, which limits their effectiveness to a small number of colors and shorter lifetimes to tag the agents. On the other hand, quantum dots can emit at different wavelength by tuning their size, are brighter and have little degradation over time thus proving them superior to traditional organic dyes used in biomedical applications.[9]

1.3 Motivations of research

In this dissertation thesis, we mainly focus on the application of QDs in optoelectronic devices, including photovoltaic solar cells and LED display technology. Application of QDs in optoelectronic devices requires proper encapsulation to maintain QDs luminescence and protect QDs from degradation. As a result, it is crucial to find a suitable matrix to encapsulate QDs without any negative effect.

This thesis is organized in the following way. In Chapter 2, we introduce the design and fabrication of QDs embedded polymer composite materials as luminescent solar concentrators. Chapter 3 introduces the addition of distributed Bragg reflectors to further increase the optical efficiency of concentrator devices, and Chapter 4 introduces the QDs enhanced output through photonic crystal structure design. The proposal and preliminary results of QD-polymer concentrating cavity for LED pixel display are described in Chapter 5.

CHAPTER 2: LUMINESCENT SOLAR CONCENTRATOR WITH QUANTUM RODS AND TRANSFER-PRINTED SOLAR CELLS

In this chapter, we examine the performance of luminescent solar concentrators utilizing CdSe/CdS core-shell seeded nanorods embedded in transparent polymer matrix. In collaboration with Paul Alivisatos research group, who synthesized these nanorods, we explored the possibility of using these quantum rods as luminophore for luminescent solar concentrators. Similar to CdSe/CdS core-shell particles, there is a small CdSe core with a large volume of CdS grown on top. However, it is possible to grow much larger volumes of CdS in the nanorod geometry than in the core-shell geometry, resulting in significantly reduced absorption-emission overlap and long propagation distances in the waveguide. We also explore the tunable geometry of the CdSe/CdS nanorod system and demonstrate that large nanorods do indeed reduce the reabsorption of luminesced photons as they travel through the film.

2.1 General introduction to concentrator photovoltaics

2.1.1 Micro silicon solar cells

Photovoltaic cells were invented to convert light into electricity in 1950's.[10] The fundamental idea was to use a semiconductor to absorb sunlight above its bandgap, which generated excited electrons. The device was structured to allow low energy electrons to pass through on one side and high energy electrons to pass through on the other side. Then an excited electron would rush out the high-energy-selective side, and be replaced by an unexcited electron on the low-energy side. This resulted in a net voltage and current that produced power. These devices were dubbed "photovoltaics" due to the light-induced voltage. The thermodynamics of photovoltaics were solved in 1961 by Shockley and Quessier.[11] Under solar illumination, the maximum possible power output of a solar cell could be calculated by knowing the band-gap of the semiconductor absorbed material. This analysis indicates that silicon is a good choice of material because of its appropriate bandgap, leading to a great deal of research developing better silicon photovoltaic cells.

As the size of the solar cell decreases, bulk recombination loss is reduced, leading to increased open circuit voltage and improved energy conversion performance. On the other hand, the increased cell surface area subjects the cell to more surface recombination. The net effect is the competition between the two factors. By careful engineering of the cell surface passivation, the efficiency of micro cells can potentially be higher. From the energy conversion efficiency aspect, micro solar cells could be beneficial, acknowledging that the energy conversion efficiency might not be optimized, compared to the highest efficiency cells on record.

With the discussion about concentrators, the factor of dimension has not been mentioned. Consider a very moderate geometric concentration ratio of 100, even with lossless interfaces and concentrator efficiency, the area of the concentrator will have to be at least 100 times larger than that of the cell. A typical bulk solar cell from a silicon wafer is 4 inches square with rounded corner from legacy of ingot cutting. The concentrator aperture will need to be at least be 40 inches on one side. For a geometric concentrator, the working distance of the concentration optical element will be on the order similar to that of the lateral dimension. So the concentrating optics with the cell will be of the dimension (40 in)3. For a concentration ratio greater than n_2, the acceptance angle is small enough to require active tracking of the sun. Moving such a concentrator plus solar module assembly would already require a significant amount of energy. If we take a step further, considering a concentration factor of 1000, then this difficulty becomes even greater. A recent review of solar concentrators shows grandeur of many different types of solar concentrators. Miniaturization of solar cells greatly relaxes the size challenge for the concentrators. Reduction in solar cell lateral dimension by a factor of 10 will decrease the system size by 3 orders of magnitude for the CPV system. This only considers system dimension and weight. For optical elements, the larger it is, the harder it is to fabricate and thus the manufacturing cost grows superlinearly with the element's size and eventually becomes unaffordable. As the solar cell itself comprises the majority of PV power generation cost, with more effective concentration, the micro solar cells can save semiconductor material for the same energy output. In other words, for the same amount of solar cell material used, more power is generated. The result is decreased cost of per unit power generated. At least from CPV point of view, micro solar cells are desired.

Crystalline semiconductor materials are usually perceived as rigid and brittle. The bending modulus of a slab object is actually dependent on the thickness and scales as thickness cubed. For very thin slab, even made of crystalline semiconductor, flexibility is also possible.[12-14] Micro solar cells within the flexible regime can access the capability of flexible module. Application such as field deplorability, fold and easy-transport, or personal backpack charger can be envisioned (Figure 2.1). Combining the pros and cons of miniaturizing solar cells, the new opportunities and challenges invite investigation of micro solar cells and the concentrators that match.

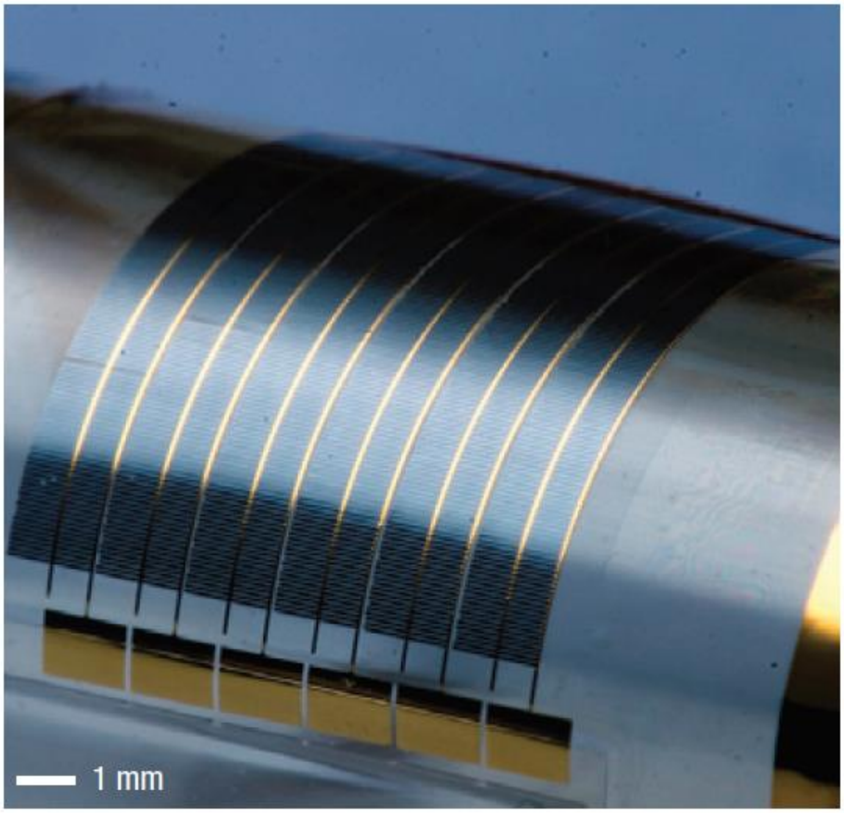

Figure 2.1 Photograph of a bent micron silicon solar cell array module.

2.1.2 Solar concentrator

One big drawback of solar power generation is the low energy area density. The solar energy covers the entire surface of the earth, so the areal average energy density is small. Plus, the energy density is also distributed to only 12 hours of insolation per day on average. For energy intensive applications, such as driving automotive and pumping laser, light concentration is needed. For the sophisticated and efficient MJ cells exhibiting high efficiency, it is desired to extract as much power as possible from each single device as they are expensive to make and it is only worth it if high intensity is incident in it and thus high power output per cell dilutes the high cost per cell. The detailed balance theory predicts that under higher flux intensity than 1 sun, the solar cell efficiency is higher than that under 1 sun, with a maximum of 40.7% for a single junction solar cell. Thus, to improve the solar cell efficiency, concentrating the sun light into smaller area is of interest energetically.

Solar concentrators can be divided into two categories dependent on if the interaction of photons with the material is elastic or inelastic. These two categories are geometric and luminescent solar concentrators. The former exploits ray optics and each photon can be reflected, refracted or scattered but photon energy does not change. The latter involves photon energy change due to interaction between incident photons and luminescent materials.

2.1.3 Geometric solar concentrator

The idea of utilizing lens arrays to concentrate parallel sunlight to a small focus point is very straight forward, but the limitation of such concentrator requires more analytical deduction. When the incident photon intensity is concentrated, the decrease in area of illumination enables us to cover less area with expensive solar cells. This decrease in translational entropy must be compensated otherwise somehow, and the answer is divergence angle. Regardless of the specific optics, the output after concentration is always more divergent than the input, as shown in Figure 2.2.[15] Figure 2.2 illustrate the concentration accompanied by beam divergence increase The concentration ratio of a imaging concentration system is where subscript 1 denotes the source and 2 denotes after concentration, I being flux intensity, n being refractive index, and θ being beam divergence angle. Consider a best scenario of θ_2 =90°, and the light source being in air, then the limit becomes if the receiving aperture, i.e., the solar cell is molded inside the lens material or index matched with the lens' refractive index n_2. One can engineer the surface of the concentrator so that all light, of all angles for diffuse light, incident on the surface can be concentrated on the output aperture where a solar cell is located, and the maximum concentration ratio simply becomes n_2. An example of such device is a hemispherical lens with the solar cell being in the center, such device does not need tracking. On the other extreme, one can reduce the acceptance angle θ_1 and thus achieve a very high concentration ratio, but such a solar cell with concentrator will require very precise tracking. With a lens material of n_2 =1.5, on a totally cloudless and dust free day, the largest solar concentration ratio is 45,000, which if achieved, is brighter than the irradiance on the surface of the sun itself.

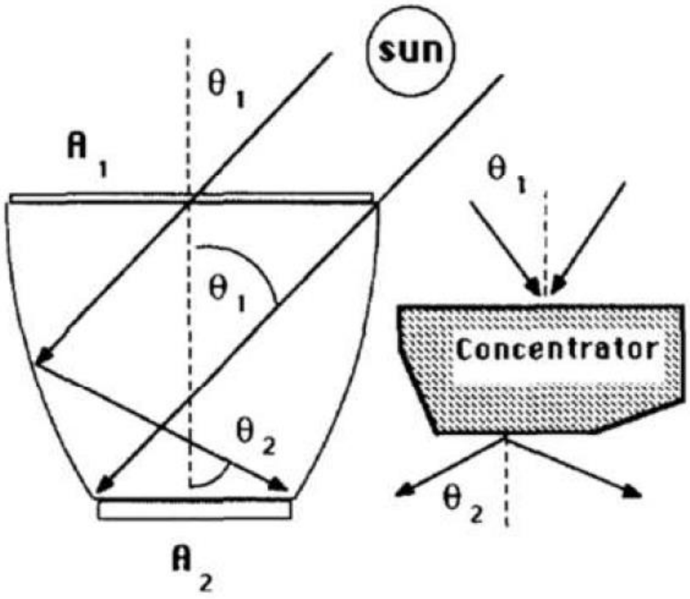

Figure 2.2 Operation mechanisms of geometric concentrators.

2.1.4 Luminescent solar concentrator

In the 1970's, semiconductor grade silicon was primarily being made for the budding microelectronics industry, and was far too expensive for photovoltaic application. Solar energy researchers responded to the economic reality of the time by proposing that solar cells could be less efficient than silicon but also dramatically less expensive.[11] One proposed method was to use fluorescent polymer waveguides to concentrate light onto traditional silicon solar cells.[16-19] These devices were initially called fluorescent planar concentrators and later became known as luminescent solar concentrators (LSC). As solar cells develop and receive more attention, the concept of LSC was proposed based on the similar principle to address the low energy area density of solar light for effective electricity generation for unit solar cell area in the late 1970s. While the economics of silicon solar panels have changed dramatically in the last several decades, LSCs may still play an important role in photovoltaic electricity production. Figure 2.3 shows photographs of different colored LSCs illuminated by solar radiation or UV light source.

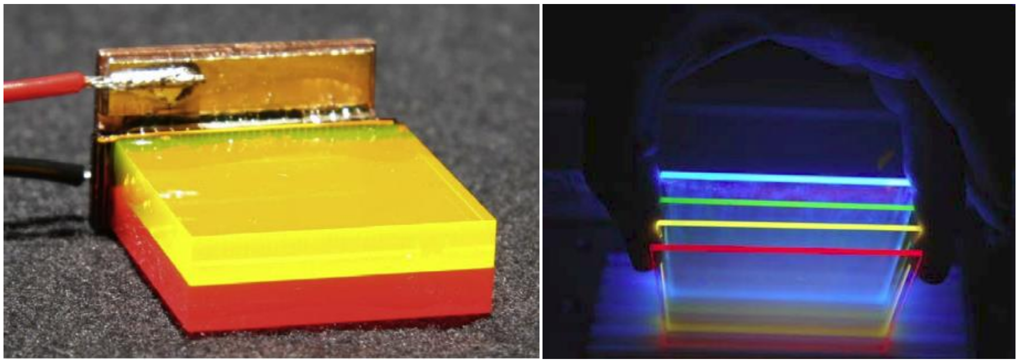

Figure 2.3 Exemplified photographs of LSC devices.

LSC consists of a single layer or multilayer polymer slabs doped with luminescent materials such as organic dyes or QDs, with solar cells embedded or attached to the sides. The luminophores absorb high energy photons and emit at lower wavelength into the polymer waveguide layer, part of which will be trapped inside the waveguide via total internal reflection (TIR) and being guided to the solar cells. LSCs can absorb both direct and diffuse incident photons, eliminating the need for any tracking system. The working mechanism of LSCs is demonstrated in Figure 2.4. Eli Yablonovitch derived a thermodynamic limit for LSC efficiency using a detailed balance principle, and concluded that the maximum concentration ratio for a planar LSC is:

$$G_f = \exp(\frac{h\Delta\nu}{kT})$$

where $h\Delta\nu$ is Stokes shift energy.[20-21] This guideline reveals two important points regarding the LSC. First of all, a LSC waveguide can have a very high theoretical concentration if engineering difficulties are solved and thus have great potential for improvement and is worth intensive research. Secondly, fluorophores with a high optical bandgap should be used as the Stokes shift is always smaller than the bandgap, thus a large Stokes shift can only be achieved if the optical bandgap is large to start with. This is unfortunately a contradicting factor for broad band absorption as the solar spectrum is broad band. At ambient temperature, for a fluorophore with a Stokes shift of 0.5 eV, the maximum concentration ratio is 4×10^8, and 2,000 for a 0.2 eV fluorophore, without any practical engineering limit. If we compromise the concentration ratio to achieve high absorption efficiency, and choose an IR emitting fluorophore that absorbs up to 1000 nm with Stokes shift of 100 nm and emits at 1100 nm, which is well suited for silicon solar cell, the maximum concentration ratio becomes 120.

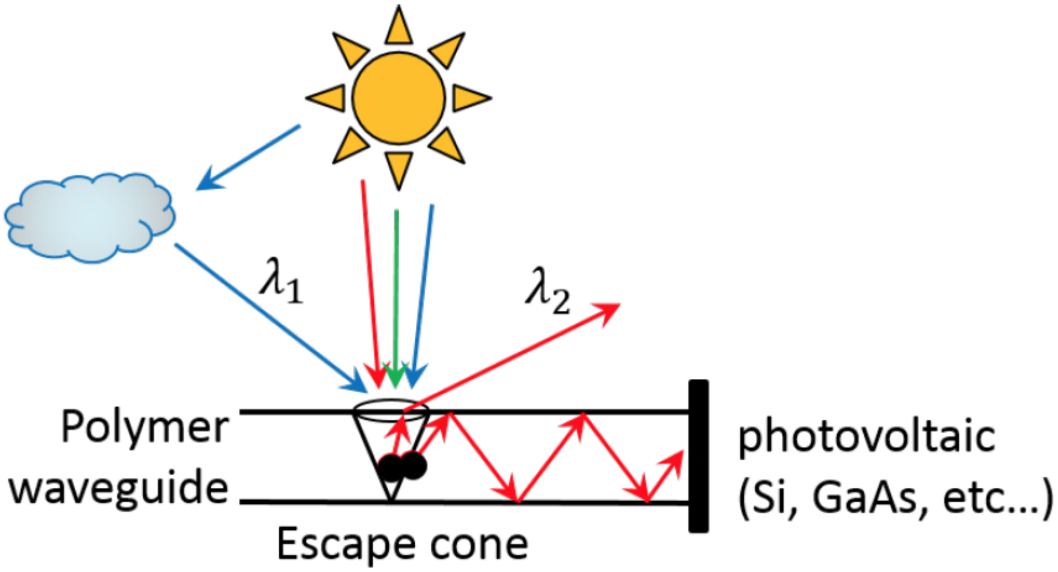

Figure 2.4 Working Mechanism of a Luminescent Solar Concentrator. Broadband and diffuse solar illumination at high enters a polymer waveguide. The high energy photons (λ_1) are absorbed by a luminophore, represented by the black circle. The luminophore re-emits the light at a lower energy, (longer wavelength, λ_2). Due to the refractive index contrast between the waveguide and the surrounding medium, most of the luminesced photons are trapped by total internal reflection. The rest impinge on the front of the waveguide at angles inside the escape cone, allowing them to couple to the air. The trapped photons travel through the waveguide some long distance and then are captured by a photovoltaic cell, which produces electricity.

However, the experimental concentration ratio achieved today is still much lower than in theory.[22] The disparity between ideal and real luminescent solar concentrators is due to incomplete trapping of luminesced light and less-than-unity fluorescence quantum yields. The root of this problem is excessive overlap between luminophore absorption and emission spectra. As a luminesced photon travels through the LSC, it may be reabsorbed by other luminophores. Every reabsorption event presents an opportunity for loss, such as nonradiative decay or emission into the escape cone. For this reason, LSC concentration ratios plateau long before the thermodynamic limit. This effect has been demonstrated by previous researchers with organic dyes and quantum dots, in microgeometries with transfer-printed silicon and GaAs solar cells, as well as studied by numerical modeling.[23-27] In order for luminescent concentrators to approach their thermodynamic limits, the luminesced light must be trapped in the polymer and directed onto the solar cell. For the most effective light trapping, a luminophore with a narrow emission spectrum and a large Stokes shift is required. Studies of light trapping have been limited by a dearth of dyes meeting these criteria. In summary, approaching the thermodynamic concentration limit will require a luminophore with large Stokes shift, high quantum yield, minimal overlap between absorption and emission, and a narrow emission spectrum.[28]

It should be noted that no matter the geometrical concentrator or luminescent concentrator, the direction of the light incident on the surface of the solar cell has been randomized, compared to the possible normal incidence directly from the sun. In the discussion of intensity ratio after and before concentration, only the flux density is considered but not the efficiency of the solar cell absorbing these photons. In other words, a solar photon reaching the surface of a solar cell is not the end of the story; rather, it is the beginning in terms of generating electricity to the outside circuit connected to the solar cell. The reflection off of the solar cell surface is a function of incident angle and wavelength, where normal incidence has the lowest reflectivity. This adds a sine factor to the observable solar cell performance enhancement for a blackbody absorber solar cell with Lambertian absorption profile.

2.2 Design of luminescent solar concentrators

Quantum dots have been considered as luminophores in LSCs due to their broad absorption spectra, high fluorescent quantum yields, resistance to photo-bleaching, and tunable absorption and emission spectra.[29] However, they have not been systematically tuned in past LSC studies to reduce the absorption/emission overlap. Single-component nanocrystals such as CdSe have significant overlap between their absorption and emission spectra and have small Stokes shifts. Core-shell materials such as CdSe/CdS utilize the separate absorption spectra of the two components to achieve lower reabsorption (Figure 2.5). While the absorption-emission overlap decreases with increasing CdS shell thickness, so does the luminescent quantum yield. Additionally, since the reabsorption is reduced by increasing the CdS shell size, a very large shell is needed. Progress has been made in the growth of thick CdS shells onto CdSe seeds, but shell thicknesses have so far been limited to around 10 nm.[30-31]

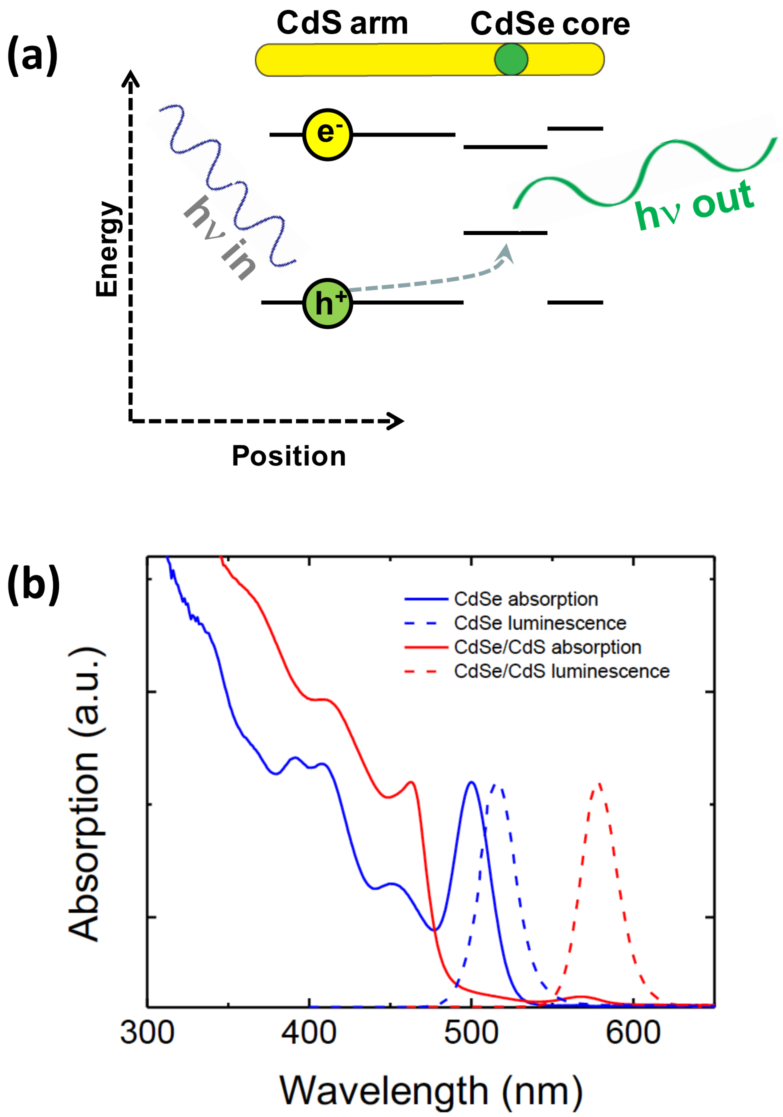

Figure 2.5

Figure 2.5 (cont.) (a) Bandgap structure illustration of core-shell QDs. (b) Absorption and emission spectra for CdSe seeds and CdSe/CdS seeded rods.

One of the main challenges in fabricating a LSC with inorganic nanoparticles is dispersing them in a polymer matrix without agglomeration or quenching of their luminescence. Earlier work by Lee et al. demonstrated that poly(lauryl methacrylate) (LMA) with a high concentration of cross-linker ethylene glycol dimethacrylate (EDGMA) may be used to form well-dispersed quantum dot-polymer composites.[32] A similar procedure has been utilized to successfully fabricate LSCs incorporating quantum dots.[33] In this part of the project, we modify the polymer formulation by reducing the cross-linker concentration to avoid stress-induced tears in the film. We also use UV initiated polymerization to promote fast polymerization kinetics and mitigate agglomeration of the nanorods. The absorption spectra, luminescence spectra, and luminescence quantum yield of the nanorods were proven to be unchanged upon integration into the polymer.

To study the performance of the LSC, a transfer-printed micro-silicon photovoltaic cell with thermal oxide passivation on the top and side walls was embedded in a 30 μm thick nanorod-polymer composite, all supported by a 180 μm thick quartz sheet.[34-35] The best performance is attained when photons can propagate long distances in the waveguide, which requires excellent reflectivity of the waveguide surfaces. For example, in a LSC with a thickness of 210 μm and a radius of 20 mm, photons traveling from the edge of the sheet must be reflected up to 100 times without appreciable loss. To obtain highly reflective waveguide surfaces, the LSC polymer sheet was formed by capillary infilling of an air gap between two smooth quartz plates. The supporting substrate was treated with an acrylate functional silane to promote adhesion, while the top plate was treated with a fluorosilane to facilitate delamination. The liquid film was then cured under UV illumination, and the top plate was removed, leaving the μ-cells embedded in a polymer sheet with a flat top surface. A schematic of the completed device is shown in

Figure 2.6(a). It is also possible to support the LSC device with flexible plastic, as shown in Figure 2.6(b). Fabrication details are given in the next section.

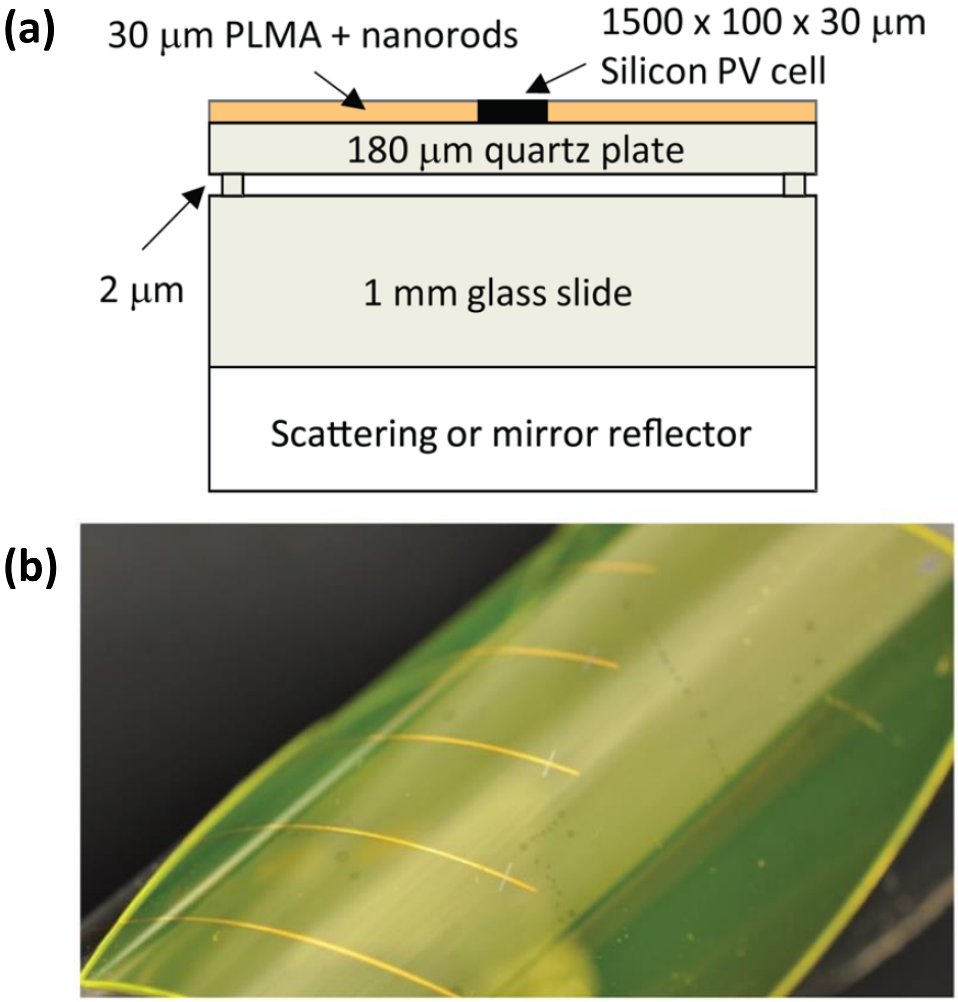

Figure 2.6 (a) vertical cross section schematic of the LSC. (b) Photograph of a fabricated device on a flexible plastic substrate.

2.3 Fabrication of luminescent solar concentrators

2.3.1 Preparation of nanorod dispersion in monomer

Lauryl methacrylate (LMA) and ethylene glycol dimethacrylate (EGDMA) were purchased from Sigma Aldrich and purified over an inhibitor removing column to remove the monomethyl ether of hydroquinone (MEHQ) polymerization inhibitor. LMA and EGDMA were mixed at a 10:1 ratio. Quantum rods in hexane solution, together with 4% volume trioctylphosphine were added to the mixture and then the solvent was evaporated with a rotovap at 40^{o}C. Photoinitiator Daracure® 1173 was added (1% volume) before polymerization.

2.3.2 Fabrication of LSC integrated with Si micro solar cell module

A 180μm coverglass was suspended on a glass substrate using 2 μm spacers and adhered at four corners using UV-curable adhesive NOA 61. 10 μm layer of partially-cured NOA61 was spin-coated on the substrate, and a micro silicon solar cell (1500 μm x 100 μm x 30 μm) was transfer-printed on it. The substrate and device were ozone activated in a UV ozone cleaner and immediately brought into 3-(Trimethoxysilyl)propyl methacrylate vapor for 1 hour to enhance adhesion between the PLMA and the substrate. Then 30 um spacer soda lime glass beads were sparsely sprinkled onto the substrate. A tridecafluoro-1,1,2,2-tetrahydrooctyl-1-trichlorosilane treated quartz plate was then secured on top of the printed cell module and spacers, with treated surface facing down. The solution of quantum rods in monomer was then capillary-filled into the cavity with the flow parallel to the long axis of the micro-cell. In inert atmosphere, the assembly was cured for 45 minutes under UV illumination. The quartz top-plate was then relieved, leaving the top surface of the micro cell and PLMA exposed. The top contact of the device is achieved by screen-printing a silver epoxy line through a stencil mask formed by aligning two sloped PDMS blocks under stereoscope and curing at room temperature for over 48 hours. The experimental procedure was illustrated in Figure 2.7.

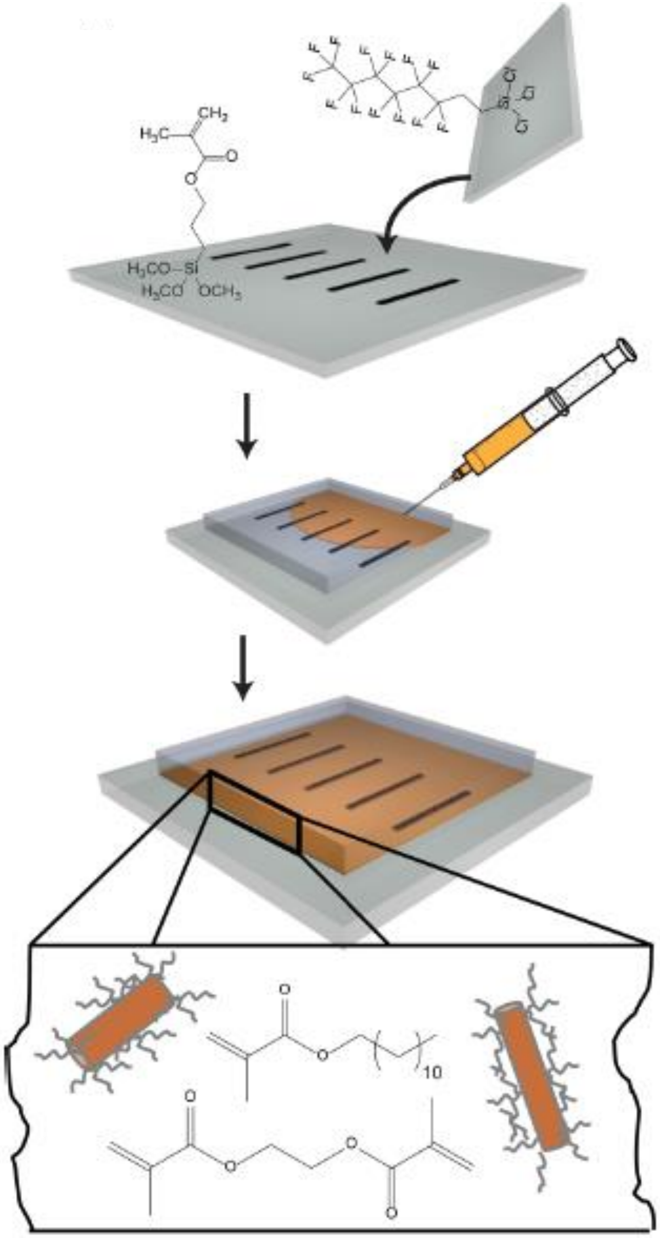

Figure 2.7 Schematic of the fabrication of the LSC device and integration with a micro silicon solar cell.

2.3.3 Optical characterization

Film absorption is characterized by a Cary 5G UV-Vis spectrometer, as well as a Cary 5000 with an integration sphere accessory, using two-beam mode with baseline subtraction. The fluorescent emission spectrum was measured on a Horiba Fluoromax fluorometer.

The photo-luminescence quantum yield (PLQY) was measured using a custom setup. The light source is an Acton Research Corp 75W xenon lamp with an Opti-Quip 1200 power supply. The monochromater is a Jarrel-Ash M-20, with a slit size set to 0.5 mm. A Labsphere RTC-060-SF integration sphere with a center sample mount is used to collect all transmitted, scattered and emitted light from the sample. The output from the integration sphere is coupled into a 200 µm FT400EMT optical fiber (Thorlabs), then into an Acton Research SpectroPro3001 spectrometer with an Acton Pixis 100 CCD camera. The detection system's spectral response was calibrated with a Labsphere halogen standard light source IRF G3 (NIST traceable). The dark current background collected over a 0.1 s integration time was recorded. The reference is taken with just the sample holder in the empty integration sphere as 100% transmitted. The sample spectrum was taken at the same condition as the dark and reference. The peak area of the transmitted signal was compared with the reference to obtain the amount absorbed and the peak area of the emission signal was compared with the reference to obtain the amount emitted. The ratio between the emitted and absorbed photons was calculated as the apparent PLQY. The experimental setup and measurement result are shown in Figure 2.8.

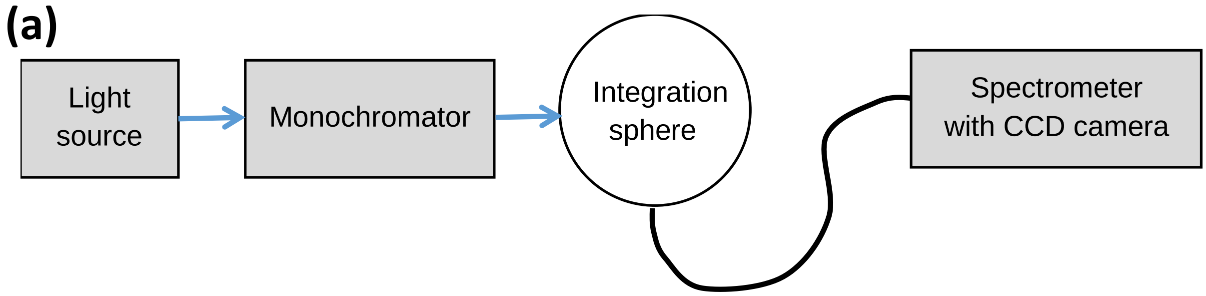

Figure 2.8

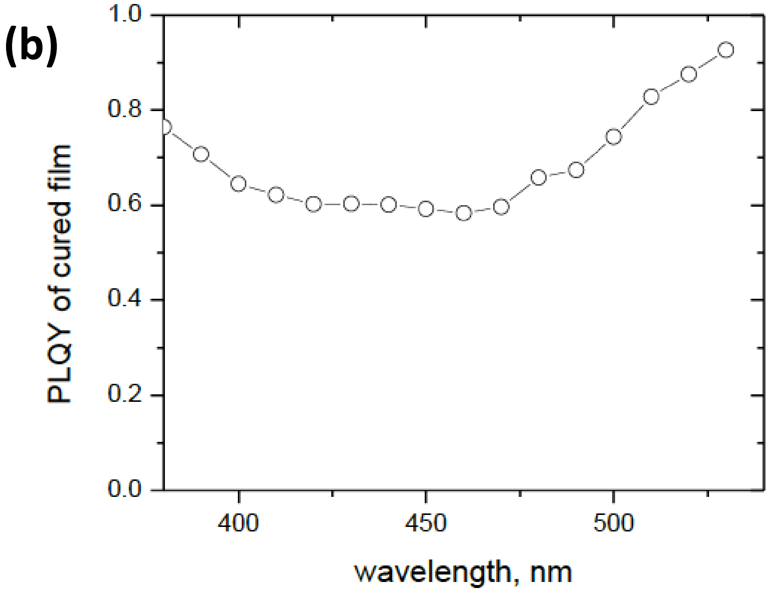

Figure 2.8 (cont.) (a) Schematic of the custom setup for film QY and trapping efficiency measurements. (b) Luminescent quantum yield of nanorods dispersed in polymer film as a function of excitation wavelength.

2.4 Optical performance of composite materials

Due to the small size of the micro solar cells, the LSC thickness should be comparable to the cell thickness, which is on the order of tens of microns, typically 15-30 µm. To achieve good light absorption for such thin film, i.e., an optical density of ~ 1 across a 30 µm film is needed. The stability of quantum rods in solution, however, becomes more challenging for high concentrations. With organic surface ligand coated nanoparticles in an organic solvent such as hexane, the suspension is kinetically stabilized. This requires good solvation of the ligand polymer brush in the solvent. Polymerization, on the other hand, reduces the mixing energy by decreasing the entropy upon polymerization, and makes the polymer a poor host for solubilizing nanoparticles. By using a neat monomer as a solvent, the quantum rods can be stabilized the same as in a small molecular solvent.

Upon polymerization, however, the kinetic stabilization is disturbed and quantum rods tend to agglomerate and fall out of the uniform dispersion. In order to combat that, the rate of polymerization related molecular immobilization, i.e., sol-gel transition, needs to be very fast compared to the rate of agglomeration of the nanoparticle in the polymerizing matrix. By using a higher percentage of bi-functional monomer, it is possible to tune the gel point to achieve fast structural formation in the polymerizing matrix and thus maintain a uniform distribution kinetically even though it is not energetically favored any more. It is found that a high crosslinker concentration, 10% +, can still maintain an agglomeration free, and thus scatter free, homogeneous film of quantum rods in polymer. The slower thermal cure makes it harder to stabilize the dispersion at a low crosslinker concentration, while at high crosslinker concentration film stress caused a saddle splay deformation. Due to these disadvantages thermal initiation was determined unsuitable and not pursued.

The film's mechanical property is dependent on the concentration of crosslinkers. The resulting film from the polymerizing monomer has a lot of stress. A high degree of crosslinking results in high rigidity and thus a more brittle film. When the film area is large and the film stress is high but the thickness is small, the great internal stress can tear the film apart. By tuning down the degree of crosslinking, the film becomes susceptible to annealing above the glass transition temperature T_g and thus can relieve some of the stress accumulated during polymerization. By changing the formulation, it is found that with a reduced concentration of crosslinker, it is easier to achieve a flat film by photo curing, and a critical crosslinker concentration of 1% is enough to form a solid film at after 30 minutes UV exposure.

During the formation of the film, it is necessary to use a relief layer to help delaminate the film from the mold surface. A silane compound tridecafluoro-1,1,2,2- tetrahydrooctyl-1-trichlorosilane (no-stick) was used. For thin films, due to the flexibility at those thicknesses, it is necessary to firmly bond the film on the substrate to retrain its shape. 3-(Trimethoxysilyl)propyl methacrylate (better-stick) was applied to the substrate to promote adhesion. This is especially important when a good contact between the solar cell surface and the polymer is needed for effective optical coupling.

To accommodate both mechanical stability and chemical dispersion stability, a crosslinker density of 10% was determined through experiments. With this composition, a nanoparticle load of as high as 4×10^{-4} M was achieved with a uniform nanoparticle distribution. The casted film can be as thick as millimeter size and as thin as micron size and remain mechanically sturdy and scattering free, as shown in Figure 2.9. The TEM graph of the polymer film shows that the nanorods are well dispersed in the polymer matrix.

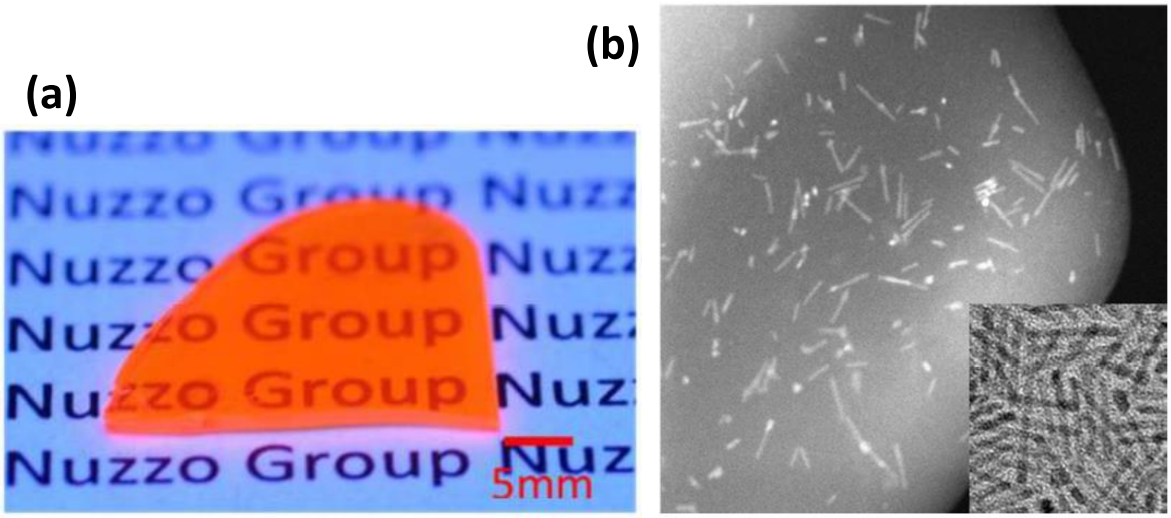

Figure 2.9 Dispersion of quantum rods in polymer host: (a) a cured block of quantum rods doped polymer block of 0.5 mm thick, under UV illumination; (b) HRTEM of quantum rods dispersion in cured polymer and in monomer before cured (inset).

2.5 Electrical performance of devices

The LSC devices were characterized by measuring the photovoltaic response of the embedded solar cell under AM1.5G illumination. Four typical curves are shown in Figure 2.10. The control device has a black absorbing back surface and no nanorods in the LSC polymer, resulting in short circuit current (J_{sc}) of 26.7 mA•cm^{-2}. The introduction of nanorods results in modest increase in the short circuit current (J_{sc} = 34.4 mA•cm^{-2}). The addition of both mirrored silver and white scattering back surfaces further increase the short circuit current (to 47.3 and 57.3 mA/cm^{-2} respectively) and result in small increases in the open circuit voltage. While it should be noted that these curves do not represent the best performance achieved in this study, the electronic properties of the cells remain consistent regardless of the LSC fabrication process, as evidenced by the consistent fill factor of around 0.7 for all devices.

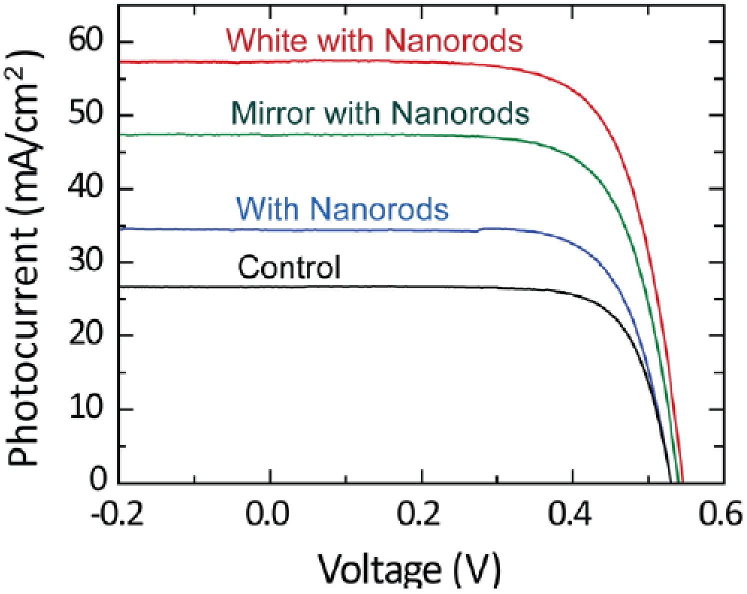

Figure 2.10 Current-voltage plot shows performance characteristics of a micro-silicon cell integrated with the LSC.

2.5.1 Effects of nanorod loading on LSC performance

Figure 1a–f shows TEM micrographs of a series of nanorods that were synthesized, keeping the CdSe seed a constant 2.5 nm diameter and increasing the final rod size from 4.1 nm × 8.8 nm in the smallest case to 9.3 nm × 78 nm in the largest case. As shown in Figure 2.11(a-g), longer and thicker rods result in a lower volume fraction of CdSe and thus lower absorption at wavelengths longer than 500 nm. Additionally, the absorption spectrum is measured in transmission mode, allowing the spectra of the largest nanorods to display scattering at energies lower than the excitonic absorption feature at 580-620 nm. Increasing nanorod size results in a red shift of the luminescence peak from 570 nm (in the smallest rods) to 610 nm (in the largest nanorods) due to reduction in quantum confinement effect. Figure 2.11(h) shows the relationship between nanorod size, luminescent quantum yield, radiative lifetime, and nonradiative lifetime. The increase in radiative lifetime with increasing nanorod volume is mitigated by an increase in the nonradiative lifetime from 79 ± 19 ns for the smallest nanorods to 494 ± 41 ns for the largest nanorods. As a result, the quantum yield does not decrease as much as one might expect, dropping from 71% for the smallest nanorods to 35% for the largest nanorods.

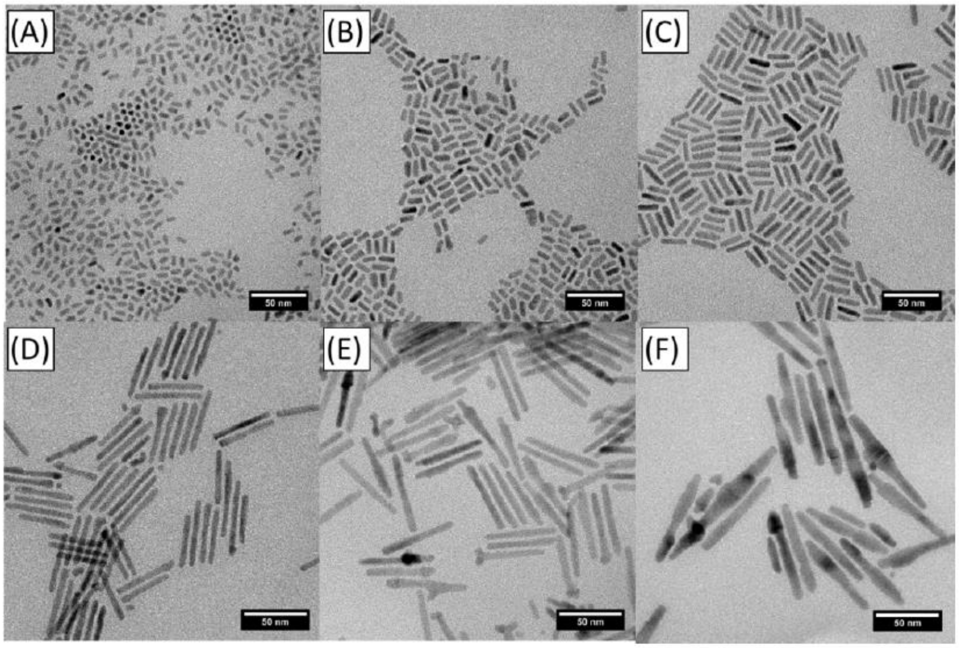

Figure 2.11

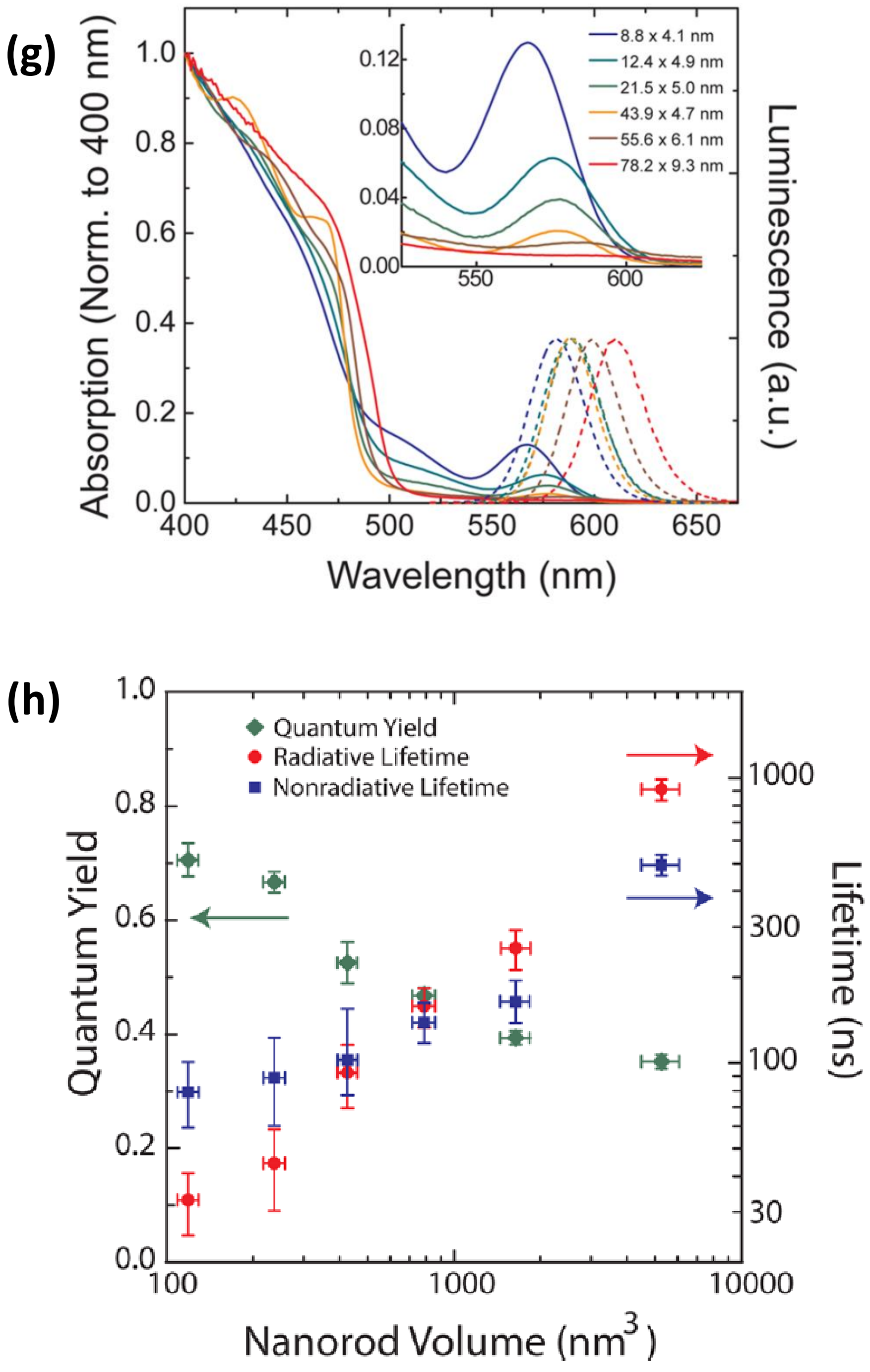

Figure 2.11 (cont.) (a-f) TEM graph of CdSe/CdS nanorods with different CdS volumes. (g) Absorption and emission spectrum of the six nanorods. (h) Luminescent quantum yield from 380 to 450 nm and radiative and nonradiative lifetimes of the six nanorods.

Figure 2.12 shows the performance of the LSC as a function of nanorod loading. The concentration as a function of incident wavelength is measured by taking external quantum efficiency measurements with the beam illuminating a 7 mm radius spot on the LSC, and normalizing to the performance of the micro solar cell measured at 600 nm in the same geometry without any luminophore and without a reflective back surface. The device with no nanorods (OD = 0) but with a reflective back surface is shown for comparison. To determine a concentration ratio, the photocurrent must be normalized. For the photocurrent vs. aperture radius data, this was accomplished by integrating the product of the AM1.5G spectrum and the blue band-pass filter transmission, and multiplying by the area of the cell and the solar cell absorption (calculated with FDTD) at the luminescence wavelength (600 nm) and normal incidence. The result is 3.495 µA.

For the spectral concentration data, which were measured on a commercial EQE setup, the illumination area of each device was held constant at a roughly elliptical 7 mm radius spot. The response of a device with a black back surface and no luminophore was measured, and the EQE at 600 nm was used as the normalization constant. The concentration can exceed 1 without nanorods but with a reflective back surface due to the angular spread of the light source in the measurement. Photons that enter the LSC at oblique angles near the solar cell can be reflected on to the solar cell. To maximize the probability that a photon travelling through the waveguide is absorbed in the photovoltaic cell, the polymer must not be much thicker than the photovoltaic cell itself, which is 30 µm. To achieve optical density of 1 in the film, approximately 0.3% of the polymer volume must be displaced by nanorods. Increasing the nanorod loading initially increases the concentration of light from the blue region of the spectrum, where the nanorods absorb, without concentrating light from the red region of the spectrum, where the nanorods do not absorb. However, above optical density 0.1, concentration of blue light decreases and concentration of red light increases because of the scattering of light in the waveguide, likely as a result of nanoparticle agglomeration. Under the UV curing polymerization scheme, increasing the EGDMA cross-linker content to 20% allows kinetic control of the polymer matrix, keeping the nanoparticles well-dispersed as evidenced by high optical clarity. These films, however, have a tendency to tear and crack, presumably due to internal stress.

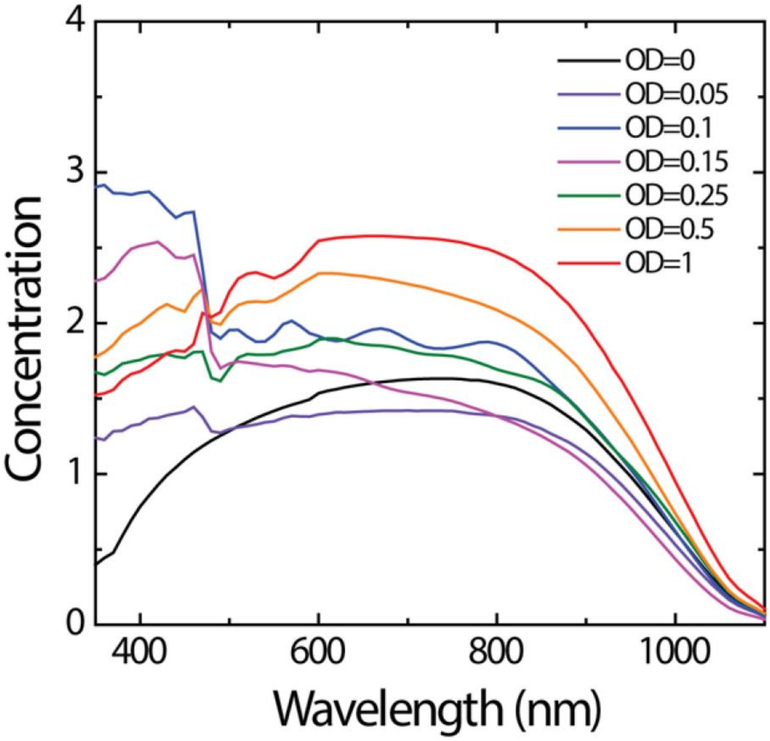

Figure 2.12 Concentration of LSC devices as a function of nanorod loadings

2.5.2 Effects of nanorod size on LSC performance

The performance of the LSC as a function of nanorod size was also investigated. Optical density for these devices was held to around 0.1 at 450 nm to avoid the scattering apparent at higher loadings (Figure 2.13(a)). This is accomplished by holding the volume fraction of CdS nearly constant. Large nanorods, then, are incorporated in fewer numbers than small nanorods. Absorption spectra of the films can be found in supporting information. Figure 2.13(b) shows the concentration as a function of wavelength for the different nanorod sizes. In all cases, the concentration of blue photons in the device follows the absorption spectrum of the nanorods; the concentration of red photons is suppressed in each case, confirming minimal scattering of light in the LSC sheet.

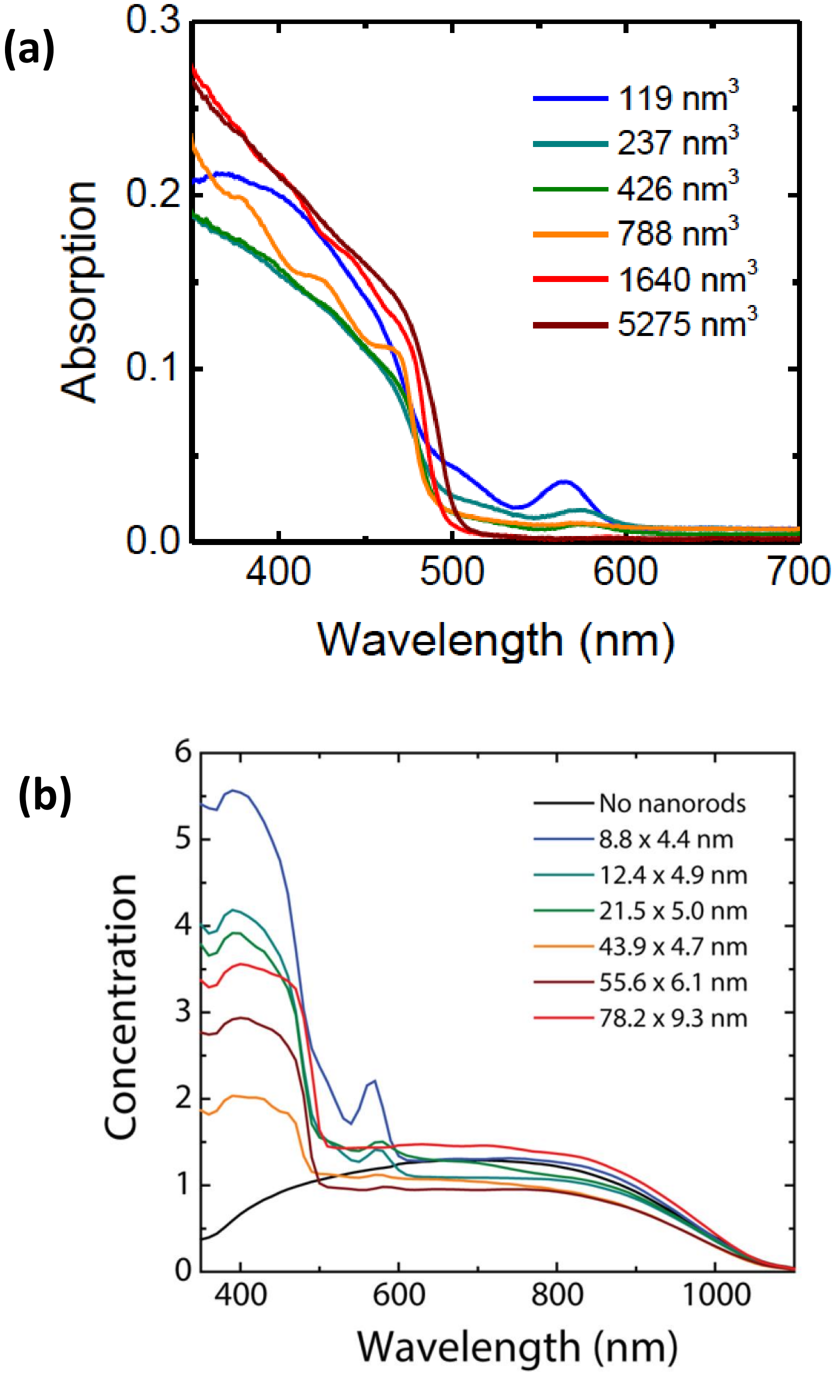

Figure 2.13

Figure 2.13 (cont.) (a) Absorption spectrum of nanorod-polymer films with different nanorod sizes. (b) Concentration of LSC device as a function of nanorod loadings

The propagation of photons inside the waveguide was characterized by illumination in a solar simulator with an aperture controlling the illumination area. A blue band-pass filter centered at 405 nm is used to isolate the luminescence of the nanorods from scattered red light. A circular aperture is centered on the silicon photovoltaic cell, and the photocurrent measured as a function of aperture radius (Figure 2.14).

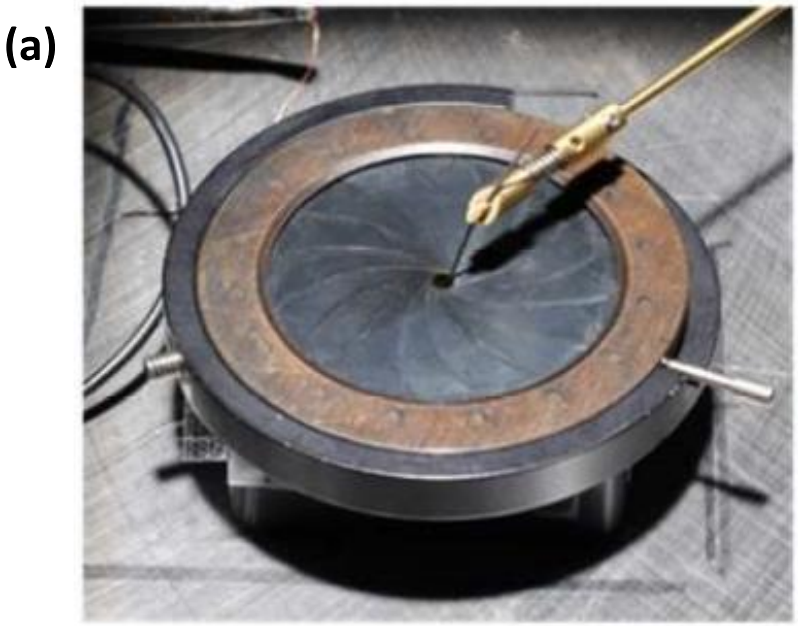

Figure 2.14

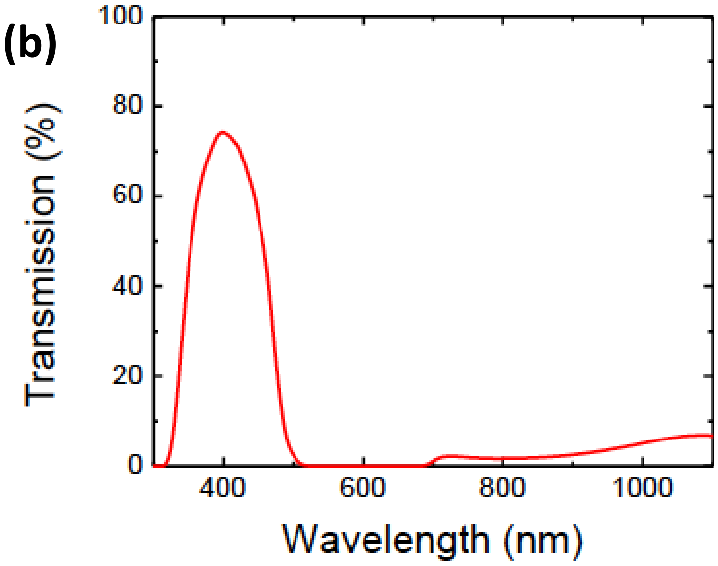

Figure 2.14 (cont.) (a) photograph of experimental measurement setup with variable aperture under solar simulator. (b) Transmission spectrum of the 400 nm band-pass filter used in the aperture study.

Figure 2.15(c) shows the results for six different sizes nanorods. The smallest nanorods show concentration that increases rapidly at small radii, but begins to asymptote at larger radii. In contrast, the larger nanorods show current that increases nearly linearly with increasing radius. The propagation of photons inside the waveguide can be approximated as an exponential decay with a characteristic length-scale known as the propagation length. Allowing for a short-propagating population of scattered photons and a long-propagating population of luminesced photons, the photocurrent is fit to the equation:

$$J_{photo}(r) = J_{max} - A_1 \exp\left(-\frac{r}{L_1}\right) - A_2 \exp\left(-\frac{r}{L_2}\right)$$

where $J_{photo}(r)$ is the measured photocurrent at an aperture radius r and the following parameters are a result of the curve fit: J_{max} is the photocurrent at infinite device size, L_1 and L_2 are propagation lengths for scattered and luminesced photons, respectively, with their associated magnitudes A_1 and A_2. This model is reasonable because the population of scattered photons must be generated on one pass through the LSC, requiring a characteristic scattering length on the order of the thickness of the LSC. As a result, scattered photons only travel a few hundred microns. In contrast, the luminesced photons have been shifted from their incident wavelength to the luminescent wavelength, allowing the different length scales for generation and propagation. The propagation length of the luminesced photons, plotted in Fig. 2.5, shows increasing propagation length with increasing nanorod volume due to the reduced reabsorption from the CdSe seed.

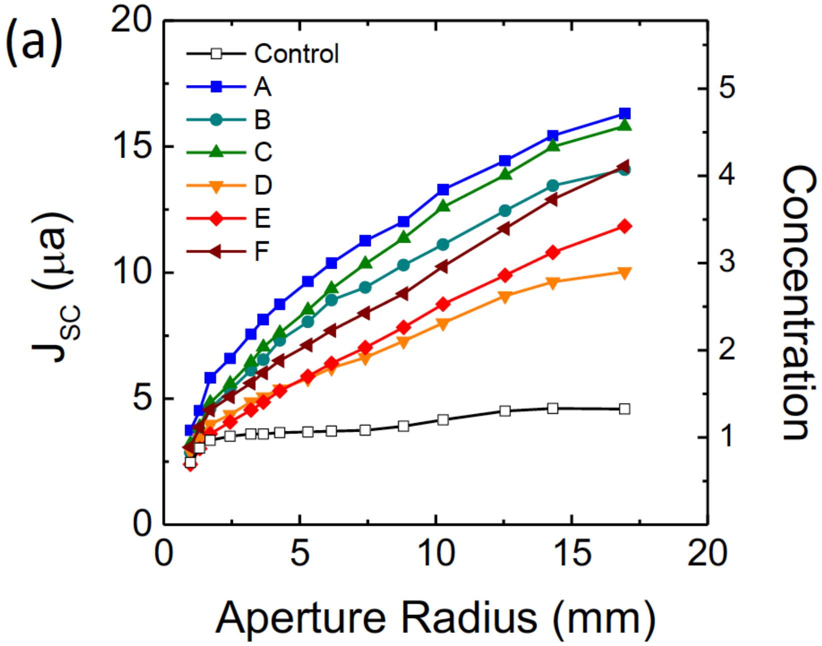

Figure 2.15

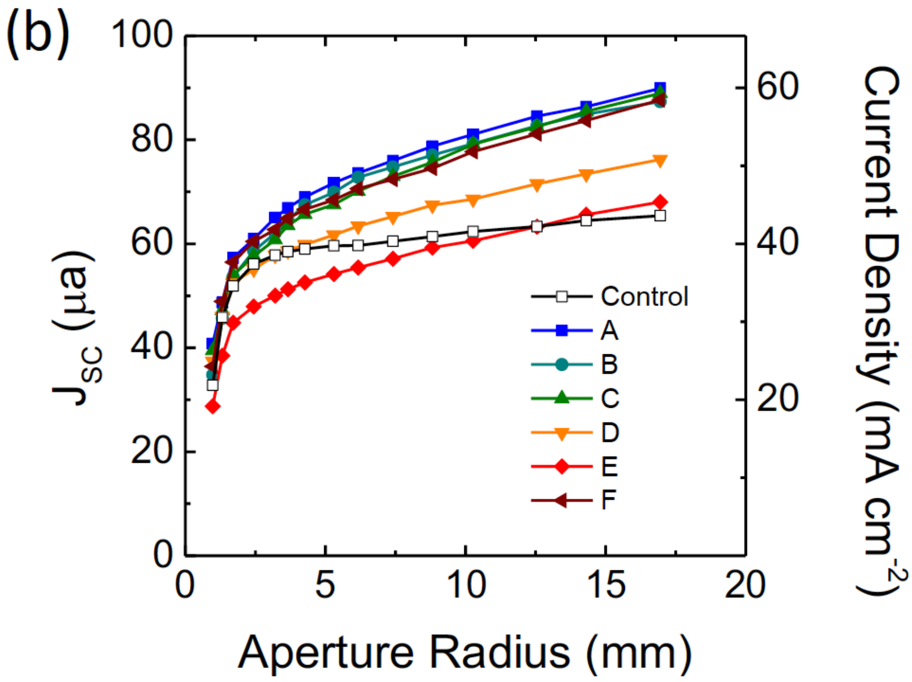

Figure 2.15 (cont.) Photocurrent dependence on aperture radius for LSC devices with different sizes of nanorods, with a white scattering back surface both (a) through a 400 nm band-pass filter and (b) under AM1.5G illumination.

As a result of the limited optical density of the films, a reflective back surface is required to increase the absorption path-length. In this study, a black anodized aluminum surface, a silver mirror, and a scattering white Spectralon surface were used. The propagation lengths in Figure 2.16 are not significantly different for the different back surfaces. A black back surface allows 1 pass for absorption, a mirror back surface allows 2 passes, and a scattering surface allows 2.2 passes for a polymer with refractive index of 1.4, as the oblique rays bend back toward normal upon refraction into the polymer. While this optical path-length enhancement is less than the $4n^2$ Yablonovitch scattering limit of 7.8, that limit is only achieved by continual randomization of photons within the polymer, which would eliminate the long-travelling waveguide modes. While it is still possible in theory to achieve luminescent concentration beyond the scattering limit in such a circumstance with the application of perfect light trapping, continuous randomization would place an extraordinary burden on the luminescent quantum yield of the luminophore and reflectivity of all surfaces. This logic also applies to highly scattering luminophores such as nanorod agglomerates and is the reason that agglomeration is detrimental to device performance.

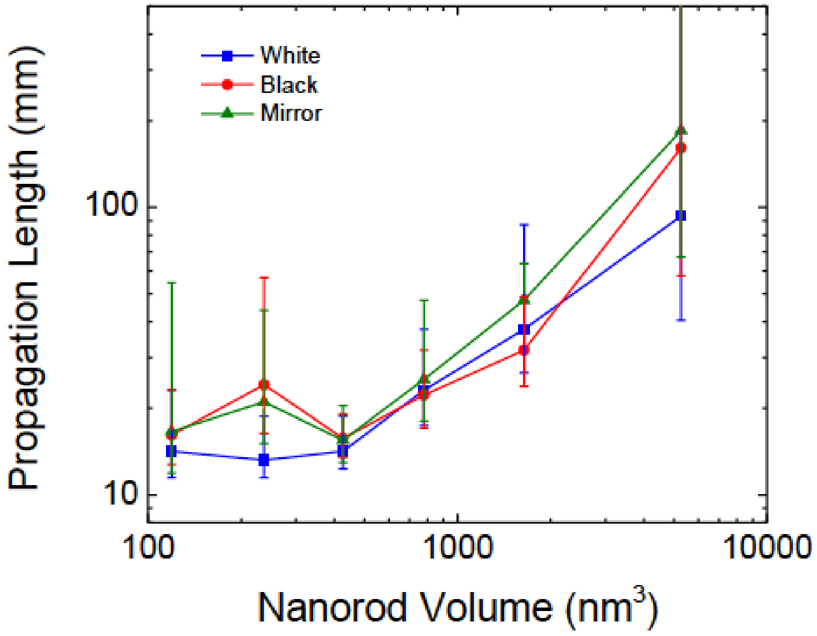

Figure 2.16 Luminescence propagation length by curve fitting with different back-surfaces.

2.6 Future directions

This investigation of CdSe/CdS nanorod luminophores for luminescent solar concentration highlights design considerations for reaching the high concentration regime. We demonstrate experimentally that increases in nanorod volume lead to increases in the propagation length of luminesced photons. We show the importance of narrow emission line widths for achieving efficient trapping of luminesced light, and the importance of efficient luminescence trapping for achieving high concentration.

Further, we show the trade-off between luminescence quantum yield and reabsorption once trapping is implemented, showing the necessity of luminophores with both low reabsorption and high quantum yield. We expect additional improvements to be made in the LSC device through synthesis of particles with bandgaps better matched to the solar spectrum, further optimization of the LSC geometry, and the utilization of a photovoltaic cell that is well- matched to the emission of the luminophore. With the design principles shown in this paper, the high concentration regime should be accessible.

CHAPTER 3: LUMINESCENT SOLAR CONCENTRATOR WITH DISTRIBUTED BRAGG REFLECTORS

Escape cone loss is one of the primary limiting factors for efficient photon collection in large-area luminescent solar concentrators (LSCs). The Stokes shift of the luminophore, however, opens up an opportunity to recycle the escaped luminescence at the LSC front surface by utilizing a photonic band-stop filter that reflects photons in the luminophore emission range while transmitting those in its absorption range. In this chapter, we examine the functional attributes of such photonic filter designs, ones realized here in the form of a distributed Bragg reflector (DBR) fabricated by spin-coating alternating layers of SiO_2 and SnO_2 nanoparticle suspensions onto a supportive glass substrate. The central wavelength and the width of the photonic stopband were programmatically tuned by changing the layer thickness and the refractive index contrast between the two dielectric materials. We explore the design sensitivities for a DBR with an optimized stopband frequency that can effectively act as a top angle-restricting optical element for a microcell-based LSC device, affording further capacities to boost the current output of a coupled photovoltaic cell. Detailed studies of the optical interactions between the photonic filter and the LSC using both experimental and computational approaches establish the requirements for optimum photon collections efficiencies.

3.1 Loss mechanisms in optical waveguide

The principal advantages of an LSC are that it operates independent of the incident irradiance angle, collects both direct and diffuse sunlight, and thus eliminates the need for precise mechanical tracking required by a geometric solar concentrator. The intention for a LSC is to replace expensive active PV materials with relatively inexpensive luminophores.[36] Recent reports from our group illustrate an unconventional geometry for LSCs whereby arrays of silicon- or GaAs-based solar microcells (μ-cells) are directly embedded in a much thinner (~30 μm) polymer matrix doped with organic or inorganic luminophores.[37-38] In this LSC system, the sidewalls and bottoms of the μ-cells are utilized to capture the luminescence while the top surfaces absorb the direct sunlight. A key feature of this layout is the large geometric gain achieved within a relatively small waveguide area due to the small dimensions of the semiconductor device. The prospective cost-effectiveness of this design follows from the low semiconductor material consumption of these light-weight devices and the capability of optimizing device spacing via a transfer-printing process.

The achievable concentration ratios and efficiencies of LSC devices have been limited historically by several loss mechanisms, including: (1) incomplete absorption of the incident illumination due to the limited spectral coverage of the luminophore; (2) a portion of absorbed photons not being reemitted, as the quantum yield (QY) of most dyes are typically less than unity; and (3) a portion of the emitted light being refracted out of the waveguide through an escape cone rather than being trapped inside it via TIR.[39-41] In addition, for luminophores with an absorption/emission band overlap, emitted photons in the TIR mode can be reabsorbed by adjacent luminescent molecules, further increasing their chances of being lost via the above-mentioned mechanisms (2) and (3). The various loss mechanisms are illustrated in Figure 3.1. These features have been discussed in previous researchers.[42-46] In this chapter, we addresses in great detail one of these issues, escape cone losses, to establish quantitative guidance for designs we have described for its mitigation.

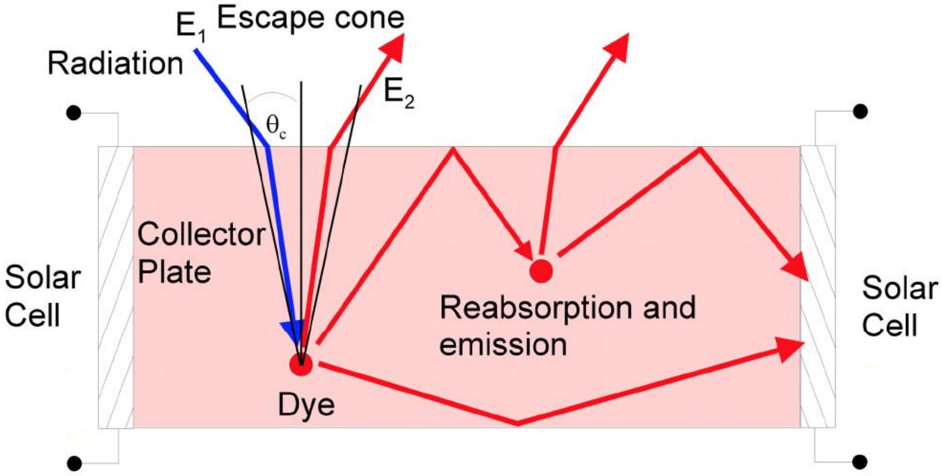

Figure 3.1 Illustration graph of loss mechanisms inside LSC waveguide.

Escape cone loss is one of the primary limiting factors for large LSC devices. As illustrated in Fig. 1, all emitted photons impinging on the internal surface with an angle smaller than the critical angle leave the waveguide and are lost. The trapping efficiency (η) in this process is determined by the refractive index of the waveguide (n):

$$\eta = \sqrt{1 - n^{-2}}$$

For a typical organic polymeric material as an example (n =1.5), η is around 74%, which means that 26% of the emitted photons are lost through the front and back surfaces. An attached backside reflector (BSR) does not change this number, as photons still leave the LSC through the front surface after being reflected at the backside. However, the Stokes Shift between the dye absorption and emission spectra opens up an opportunity to trap all of the potentially escaping photons at the front surface using a photonic band-stop filter, which reflects all the light in the dye emission range while transmitting all the light in the absorption range (see Figure 3.2).[47-49] Such an idealized filter would eliminate the escape cone losses completely. A real filter, however, will show a reduced performance for several reasons. First, as an absorption/emission overlap exists in all dye species, it is impossible to design a filter that reflects all the emitted luminescence without some measure of losses in the luminophore absorption band. Second, the reflectivity of the filter's stopband will be lower than unity and so not all light in the escape cone will be recycled.

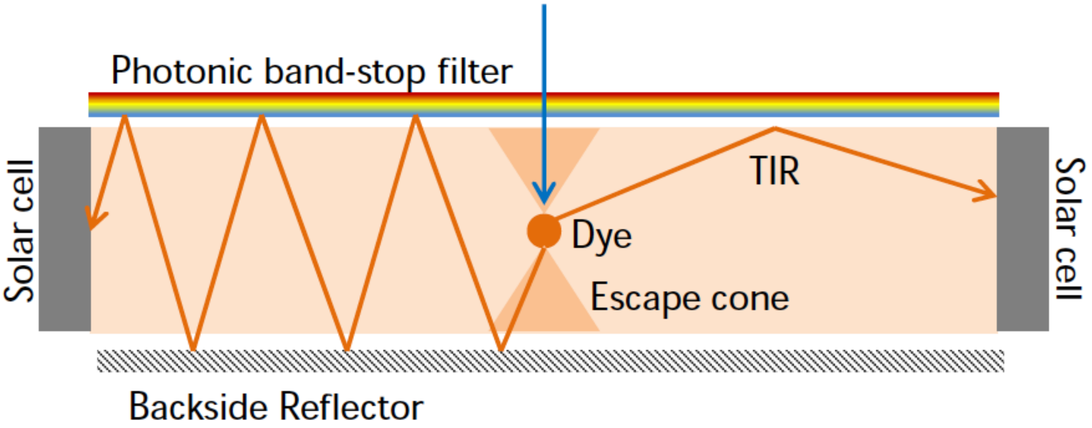

Figure 3.2 Effects of a photonic band-stop filter on top of a LSC device: the filter selectively reflects back luminesced photons in non-TIR modes and guides them to the attached solar cell to generate extra power, while allowing the transmission of light in the dye absorption range.

Finally, the most important challenge with a photonic band-stop filter originates from the dependence of reflectance on the photon incidence angle. The stopband typically is shifted towards shorter wavelengths, with a decreasing reflectivity seen for increasing incidence angles. As the directions of the luminescent photons impinging on the front surface of the LSC are isotropic, photons with oblique angles are subjected to a lower trapping efficiency with a photonic mirror as compared to ones with a steeper angle of incidence. Light with steep angles, however, results in extremely long effective path lengths within the waveguide before it reaches the solar cell. It therefore suffers more strongly from path length dependent losses, including dye reabsorption, matrix absorption, and scattering. As a consequence, the photon recycling efficiency of the top filter will be dependent on the photon incidence angles, a result of both the filter's angle dependent reflectivity and the path length dependent propagation losses.

These complexities make the demands placed on the quality of the photonic structure very high.[50] Only a filter with very low reflectance in the absorption range of the dye, a very high reflection in the emission range, and a very steep edge between these two spectral ranges has the potential to produce large/useful increases in light collection efficiency. The bandwidth and central wavelength of the filter further therefore need to be carefully designed to overcome the angle dependence of the reflectance and the resulting path length dependent loss of recycled photons. Suitable candidates for such structures include organic cholesteric mirrors[51-54], inorganic Bragg stacks[55-58], and Rugate filters.[59-63]

These optical structures are all one-dimensional photonic crystals, consisting of alternating layers of two materials with a refractive index contrast. The reflected waves at each layer boundary can interfere constructively, creating high reflectance for a certain wavelength range, the so-called a photonic stopband. These photonic structures have been used as band-stop filters directly on solar cells and LSCs to selectively reflect photons within the escape cone and to achieve enhanced photon recycling.[64-68]

3.2 Fabrication of distributed Bragg reflectors

A series of DBRs with different λ_c values was fabricated via layer-by-layer spin-coating of SiO_2 and SnO_2 nanoparticle suspensions with a subsequent calcination step to remove residual organic components, as reported by Puzzo et al.[69] The as-prepared dielectric multilayer, here supported on a quartz substrate, displays high optical uniformity over a large central region of the optic, with minimal adventitious defects, as illustrated by the optical images presented in Fig. 3.3(a). It is noteworthy that the size of the DBR is only limited by that of the underlying substrate, and could be expanded by using a larger quartz plate and optimized coating processes. A cross-sectional secondary electron microscopy (SEM) image of the fabricated DBR is presented in Fig. 3.3(b). The spin-coating method yields a periodic multilayer stack with well-defined, flat interfaces between the adjacent layers, which are critical to minimize undesired scattering/refraction and ensure excellent optical properties. The first-order stopband central wavelength (λ_c) of the DBR is determined by the Bragg equation:

$$\lambda_c = 2(n_1 d_1 + n_2 d_2)$$

where n_1 and d_1, n_2 and d_2, are the refractive indices and thicknesses of the two dielectric materials in the stack, respectively. In this fabrication protocol, the thickness of each dielectric layer can be effectively manipulated via the spin-coating speed and suspension concentration (see Fig. 3.4), generating DBRs with various values of λ_c. The reflectance spectra of the as-prepared DBRs were measured at normal incidence and are plotted in Fig. 3.3(c). The experimental spectra agree well with ones simulated using the transfer-matrix method (see Figure 3.5), confirming the high optical quality of the DBRs. The reflectivity of a DBR increases with the number of alternating layers, owning to the increasing number of constructive and destructive interferences occurring at its layer boundaries. Each DBR for which data are presented in Figure 3.3(c) consists 16 alternating layers, leading to peak reflectance values as high as 95%. These values are suitable for use in studies exploring their utility as photonic band-stop filters for LSCs. The stopbands of the DBR shift to shorter wavelengths as the light incidence angles (θ) increase, as shown by the experimental and simulated reflectance data presented in Figure 3.3(d) and (e). This effect can be seen visually by looking at the DBR at different viewing angles (Figure 3.3(a)). The angle-dependent reflectance of the DBR provides a critical constraint for the design of a LSC-DBR system, as an optimized DBR should allow high optical transmission in the dye absorption range while providing angle restriction for escaped luminescence, as discussed in greater detail in sections that follow.

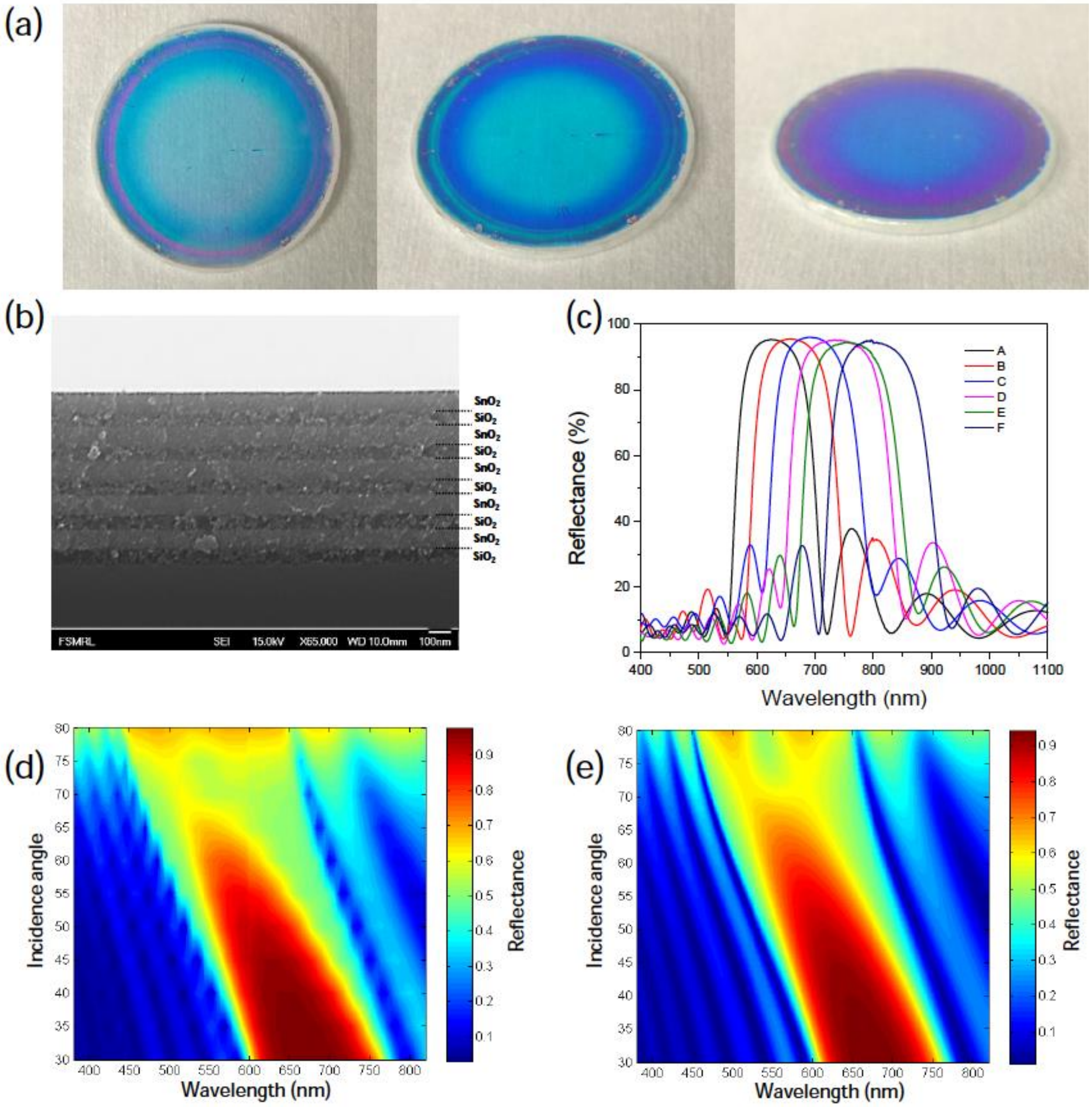

Figure 3.3 Characterization of fabricated photonic structure: (a) Optical images of a spin-coated DBR, its central region shifts from blue to purple as the viewing angles become more oblique. (b) Cross-sectional SEM image of a DBR with alternating layers of SiO_2 and SnO_2. (c) Reflectance (normal incidence) of six DBRs with various stopband positions, achieved by tuning the thickness of spin-coated dielectric layer. (d)

Figure 3.3 (cont.)

Experimental and (e) simulated reflectance spectra of a DBR, its stopband shifts to shorter wavelength range with increasing incidence angles.

3.3 Device fabrication

SiO_2 and SnO_2 nanoparticles were purchased from Sigma Aldrich (Ludox SM-30, 30 wt%) and Nyacol Inc. (15 wt%) respectively. SiO_2 suspension was diluted to the desired concentration. Each suspension was filtered through 2 μm pore syringe filter to remove any nanoparticle agglomerates. Piranha cleaned quartz discs or silicon wafers were used as substrates for the nanoparticle DBRs. The prepared SiO_2 and SnO_2 nanoparticle suspension was spin-coated sequentially onto the substrate between 2000 and 5000 rpm for 30 s until 16 layers were deposited. The relationship between spincoat speed, nanoparticle concentration and film thickness are shown in Figure 3.4. Following each layer deposition, the substrate was baked on hotplate at 400 ^{o}C for 30 min. A small opening the size of the solar cell was carved in the center the DBR with a razor blade to allow direct solar radiation on the top surface of the cell.

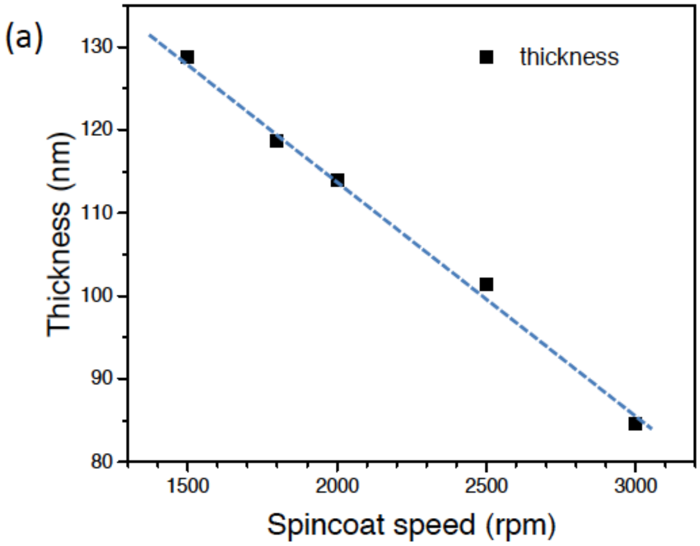

Figure 3.4

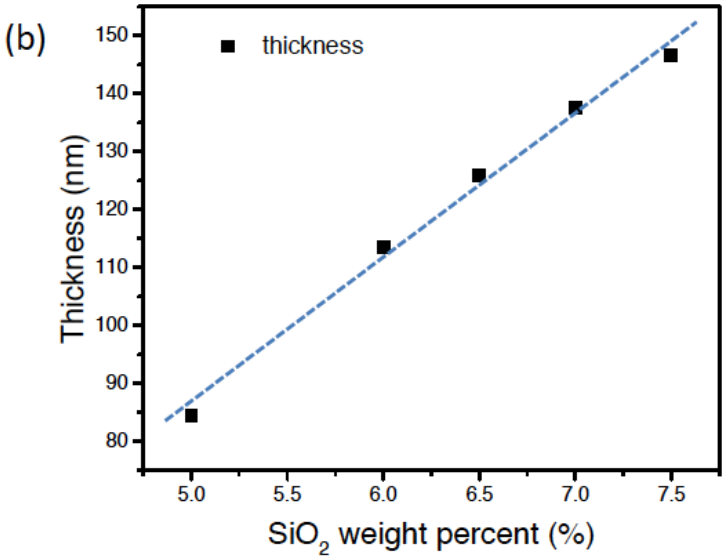

Figure 3.4 (cont.) Spin-coat recipes for SnO_2 and SiO_2 suspension. (a) The SnO_2 concentration was kept at 15 wt% while the spin speed changed between 1500 and 3000 rpm to achieve desired film thickness; (b) The SiO_2 spin speed was kept at 3000 rpm while the concentration changed between 5 wt% and 7.5 wt% to achieve desired film thickness.

Fabrication of LSC integrated with Si solar microcell: Fabrication and transfer-printing of solar microcells has been described previously. A glass substrate is prepared by spin-coating a layer of partially-cured UV-curable adhesive (NOA61, Norland) at 3000 rpm. Then 30 μm soda lime glass beads (SPI product #2714) were sparsely sprinkled onto the four corners of the substrate. A repel silane (GE health) treated quartz plate was then secured on top of the printed cell module. The solution of DCM in NOA was then capillary-filled into the cavity with the flow parallel to the long axis of the micro-cell. The assembly was cured for 20 minutes under UV, and the quartz top-plate was peeled off afterwards. The top contact of the device is achieved by screen-printing a silver epoxy (E4110, Epoxy Technology) line on two top contacts of the cell and curing at room temperature for 48 hours. The DBR was directly applied on top of the LSC device with solar cell aligned with the carved opening in the middle of the DBR. The control sample was measured with a quartz plate the same as DBR substrate applied on top to compensate for the reflectance of the quartz plate surface.

SEM images were obtained on a JOEL 7000 FE Scanning Electron Microscope. Film thickness and angle-resolved reflectance of DBR was measured using a J.A. Woollam VASE Ellipsometer. Photovoltaic characterization was performed with a Keithley 2400 Sourcemeter. The illumination source is an Oriel 91192-1000W Solar Simulator with an AM1.5G filter. Its light intensity was calibrated to one sun and monitored by a Radiant Power Meter and Probe (New Port 70260 and 70268), with a measured intensity fluctuation of ~1%. External Quantum Efficiency is measured using a Gooch & Housego OL-750 Automated Spectroradiometric System.

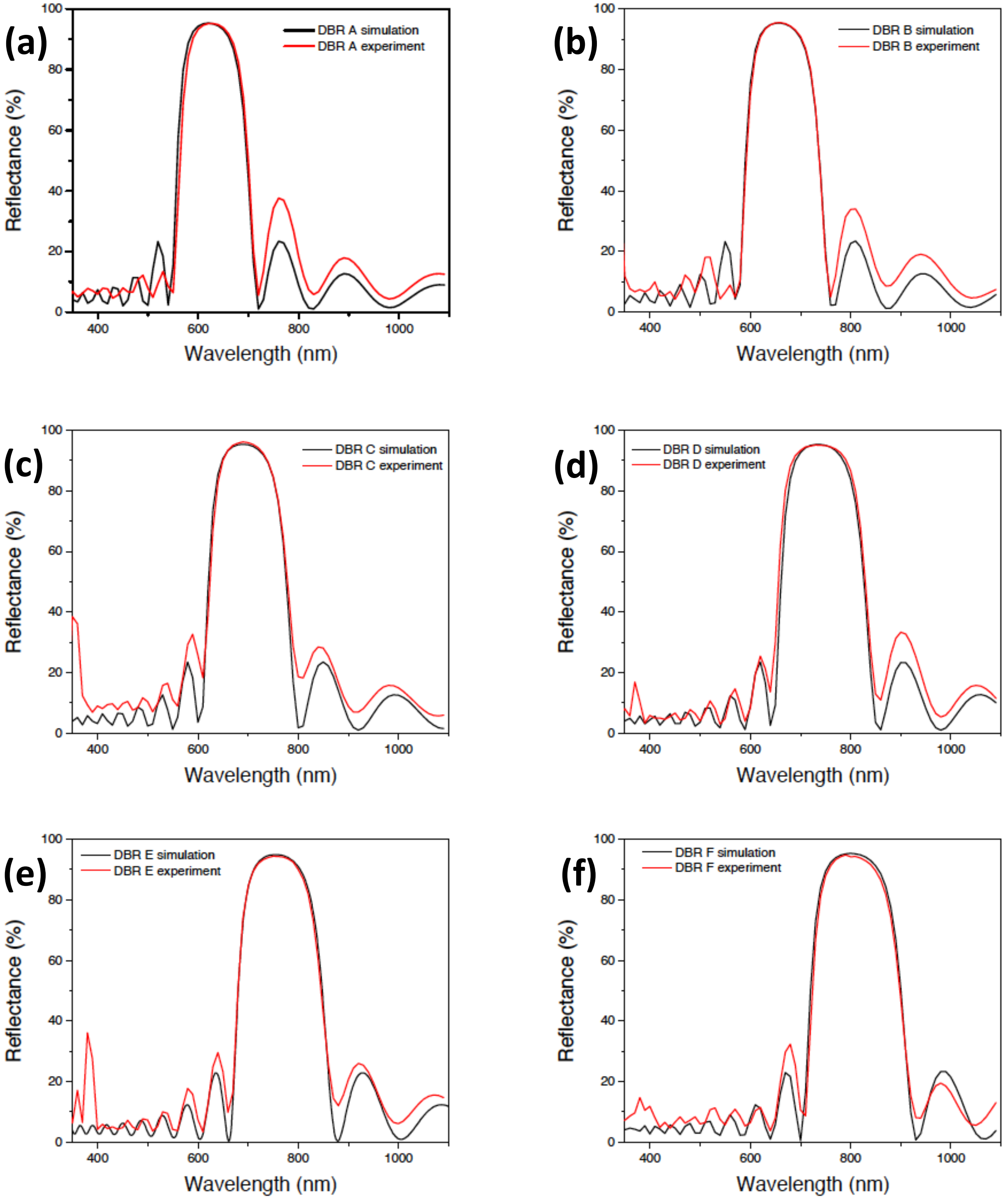

Figure 3.5 Simulated versus experimental measured reflectance of all DBRs (a-f). The simulated results were calculated using the transfer matrix method.

3.4 Device performance

3.4.1 Nanoparticle distributed Bragg reflector

The LSC system utilized in this study consists of transfer-printed silicon solar microcells42 (30 µm thick, 100 µm wide and 1.5 mm long) embedded in a polymer matrix doped with an organic luminophore (DCM), supported on a thin (180 µm thick) quartz substrate, as illustrated in Figure 3.6(a). An embedded PV microcell provides what is an essentially weakly perturbing means for measuring the photo fluxes present in the waveguide. A DBR (λ_c = 735 nm, Sample D) is placed directly on top of the LSC device with a natural air gap in-between to trap the escaped luminescence, while photons already in the TIR modes remain unaffected by the photonic structure (a cross-sectional illustration is presented in Figure 3.6(b)).

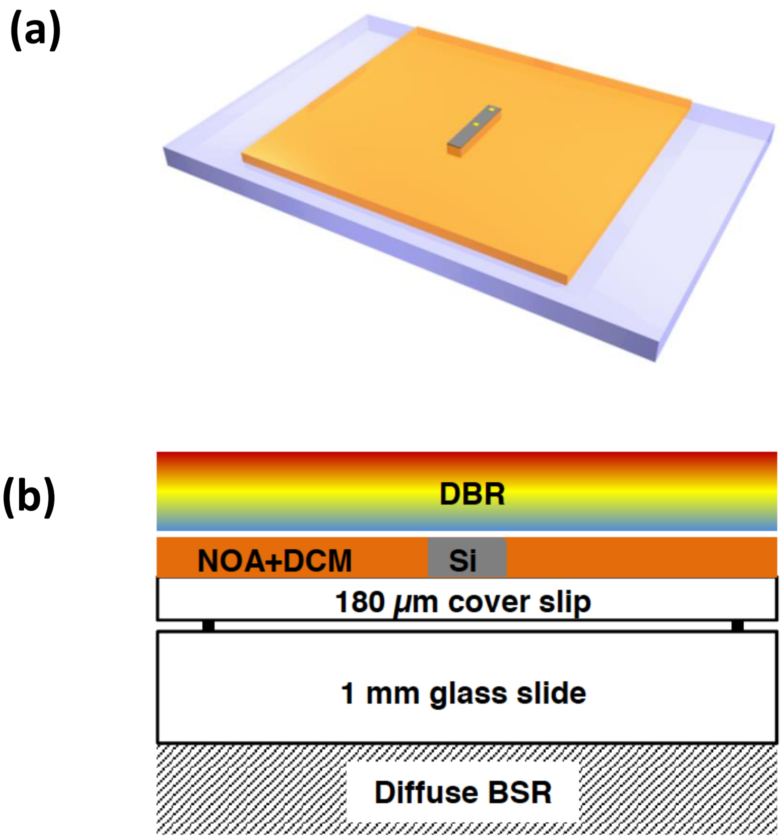

Figure 3.6

Figure 3.6 (cont.) (a) 3-D illustration of a LSC device composed of a silicon solar microcell (grey) and a polymer matrix doped with DCM (orange) supported on a thin glass substrate (light lavender); (b) Cross-sectional schematic of the LSC device with a top DBR

This particular photonic mirror is designed to allow high transmission of incident illumination within the DCM absorption range, while providing high reflectance for emitted luminescence at larger incidence angles. This can be seen in the comparison of the dye absorption/emission spectra and the DBR reflectance data presented in Figure 3.7(a): it is notable that the DBR reflectance peak matches that of the dye emission when $\theta = 60$ degrees (i.e. not at normal incidence). The relationship between dye emission and stopband frequencies in terms of the LSC performance is discussed further in the following section. With the addition of the DBR ($\lambda_c = 735$ nm), the short circuit current (I_{sc}) of the device increased 6%, from 100 µA to 106 µA (Figure 3.7(b)). In contrast, the I_{sc} of the blank control sample (no luminophore in the NOA matrix) dropped from 56.0 µA to 51.8 µA after applying the DBR, due to the fact that the DBR stopband blocks part of the incoming solar radiation that can be utilized by the microcell through non-TIR waveguiding. To isolate the luminescence recycling effects from the top photonic structure, the current output contributed from the dye emission (I_{dye}) was calculated by subtracting the I_{sc} of the blank control sample. Compared with the LSC value without a DBR ($I_{dye} = 100\text{-}56 = 44$ µA), the I_{dye} value (106-51.8 = 54.2 µA) of a LSC with DBR showed a 22% relative enhancement, indicating that otherwise escaping photons are being recycled back into the waveguide by the top photonic mirror.

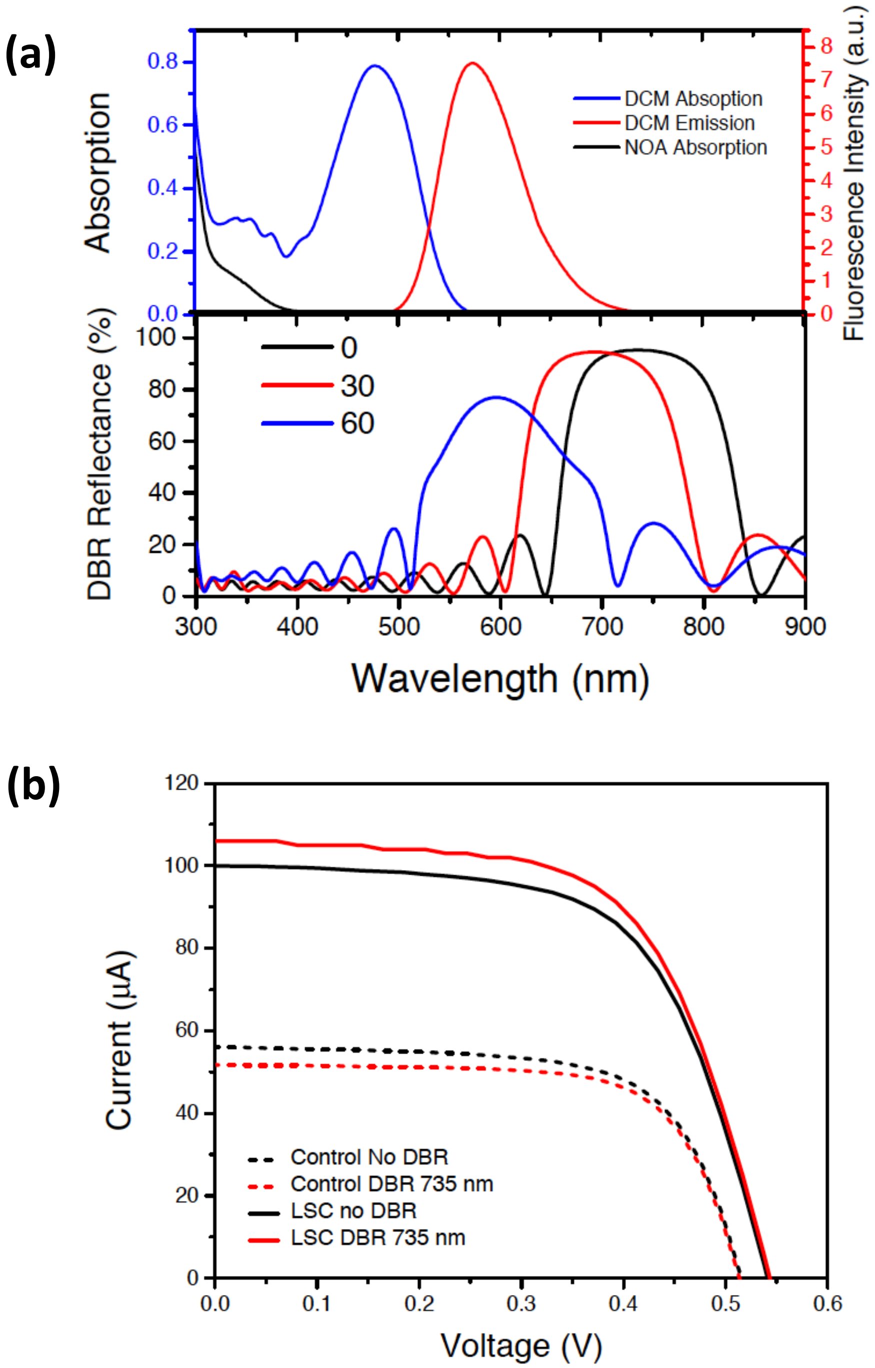

Figure 3.7 (a) Comparison between DCM absorption/emission spectra and DBR reflectance: DBR allows the transmission of dye emission at close to normal incidence, while reflects dye emission at larger incidence angles; (b) I-V curves: adding a DBR on top results in an increase of I_{sc} for a LSC device

The light management properties of the different DBRs were further elucidated by the results of the external quantum efficiency (EQE) measurements, the data for which are presented in Figure 3.8(a). The benefits from the luminophore on PV performance are highlighted by the marked blue spectrum enhancements that are seen, ones corresponding to the dye absorption (curves in red vs. black in Figure 3.8(a)). This illustrates the changing fraction of the emitted photons from the luminophore that are trapped in TIR modes and subsequently collected by the embedded solar cell in the waveguide. The DBR series A-F (reflectance data shown in Figure 3.3(c)) were placed directly on top of the LSC device. Adding photonic band-stop filters results in a significant dip in the EQE curves at frequencies corresponding to their photonic stopbands. This effect is also seen in the EQE measurements made of a blank control sample without a luminophore present when the same DBRs are applied on top (Figure 3.9). These results show that the photonic filter brings intrinsic challenges in that it blocks the part of the solar spectrum corresponding to its stop-bandwidth. This blocking of illumination results in a decrease in the short circuit current. This negative effect can be mitigated, however, by reducing the bandwidth of the DBR, with the caveat that a lessened coverage of the dye emission spectrum and will lead to a lowered luminescent photon trapping efficiency. The key point is that, for an overall positive effect, the illumination blocking loss will need to be exceeded by the current gain from the photon recycling afforded by the DBR. Experimentally, the enhanced EQE responses seen after adding a DBR are observed at two distinctive regions (Figure 3.8(a)): the first occurring on the high-energy side of the DBR stopbands (580 to 700 nm); and the second in the dye absorption region (300 to 580 nm).

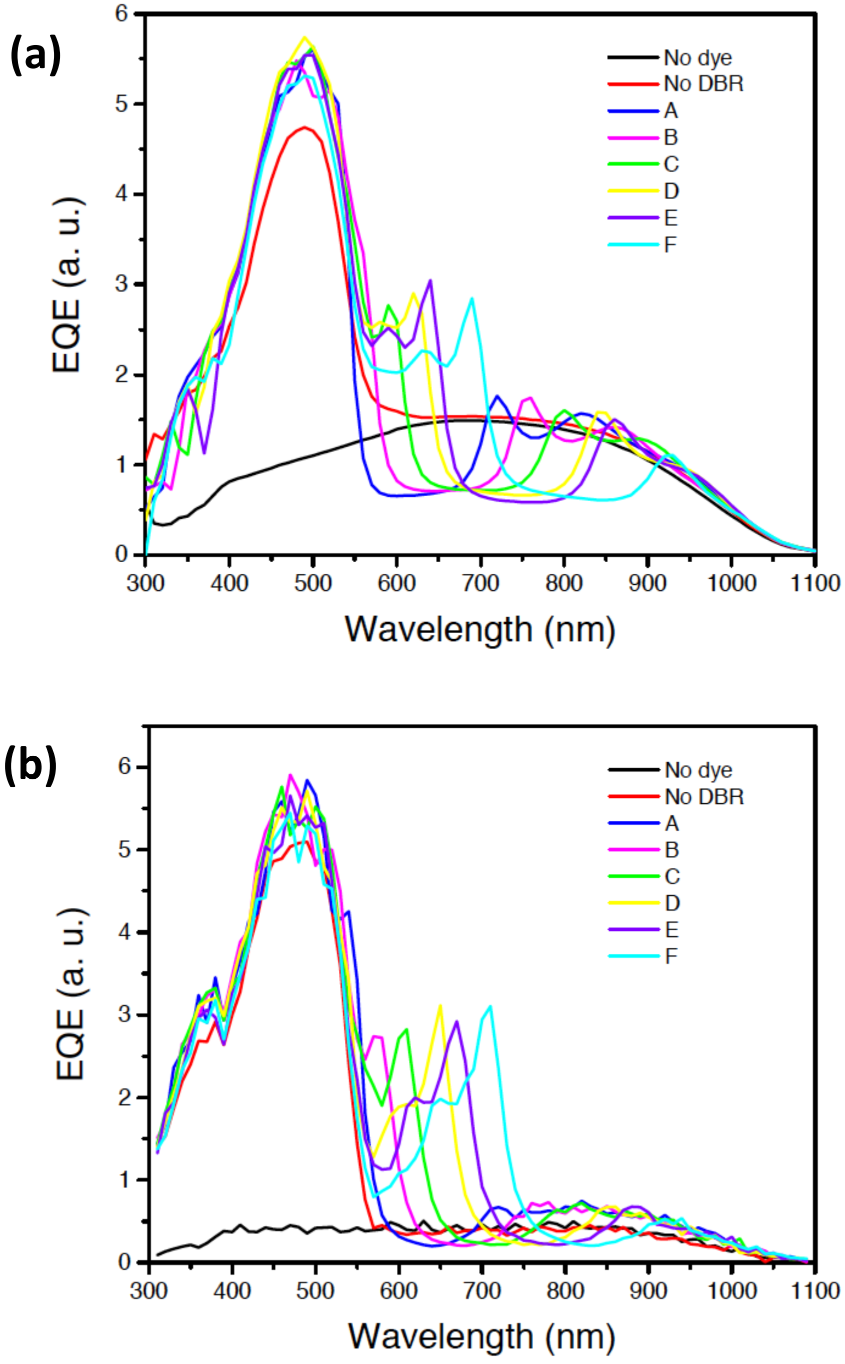

Figure 3.8 (a) Experimental and (b) Simulated EQE for a LSC device with various DBR, the photon recycling effects are evidenced by the enhancements in the blue region.

The features seen on the high energy side of the stopbands in the EQE plots are due to the angle restriction effects of the DBR on the photons reflected by the diffuse backside reflector. Here the photons transmitted through the LSC film bounce back with randomized directions, and when it reaches the top photonic mirror again, have new, angular-dependent chances of being recycled into propagating modes (non-TIR) inside the cavity between DBR and diffuse backside reflector before reaching the cell. Since the DBR reflectance blue-shifts as the incident angle increases, photons with a higher energy than DBR bandgap have a larger chance of being recycled, leading to enhanced collection efficiencies on this side of the stopband. It is important to note that this enhancement is not large enough to compensate for the total current loss due to the stopband, a conclusion further supported by the fact that all current output from a blank control sample (i.e. without luminophore) is lost in the stopband when it was coupled with a DBR. As shown in the Figure 3.9 and Table 3.1, the blue spectrum response is suppressed because there is no dye present to absorb and emit photons. The response dips corresponding to each DBR stopband and the peaks on the high energy side of the dips are identical to those of the dye-embedded LSC sample, indicating that these features are non-relevant to dye presence.

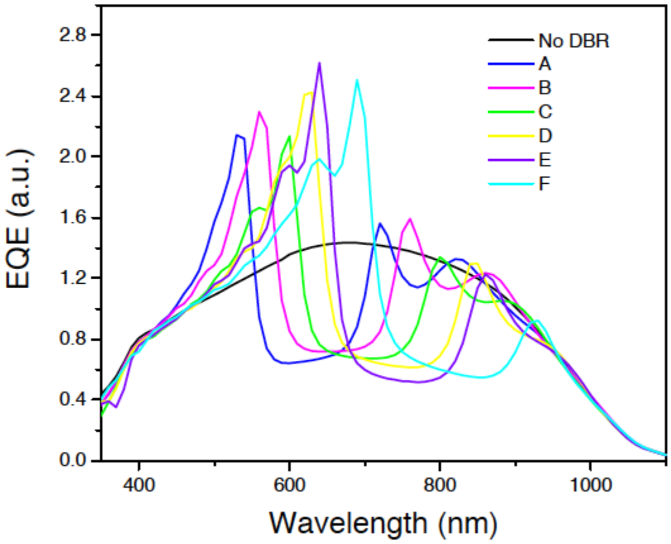

Figure 3.9 EQE measurement of the blank control sample with each DBR applied on top.

	No DBR	A	B	C	D	E	F
I_{sc} (μA)	53.34	48.89	49.36	52.17	51.77	51.19	54.44

Table 3.1 Short circuit current of the measured blank control sample with different DBR. The I_{sc} of the device with DBR are always lower than without DBR, indicating that the enhancement in the EQE curve does not compensate the dips caused by DBR blocking part of illumination.

Significant UV-blue region enhancements associated dye absorption are observed with all the DBRs (Figure 3.8(a)), as each can reflect fluorescent photons within a certain range of incident angles. As its stopband red shifts away from dye emission peak, the photons that can be reflected by the DBR will be at a larger angle of incidence. For example, the reflectance of DBR A (λ_c = 620 nm) matches the dye emission at an angle close to normal incidence, while for DBR D (λ_c = 735 nm), matches it at around 60 degrees. To assess the quantitative impacts of these effects, an integration of the EQE with excitation by the AM 1.5G solar spectrum was carried out between 300 and 580 nm (the dye absorption range) to quantify the current contribution coming from the dye luminescence for each of the different DBRs. These results are presented in Table 3.2.

λ_c (nm)	No DBR	620 (A)	656 (B)	690 (C)	735 (D)	760 (E)	800 (F)
$I_{300\text{-}580}$ (μA)	52.9	57.6	63.0	63.6	64.4	61.9	58.7
ΔI (μA)	0	4.8	10.1	10.8	11.5	9.1	5.8

Table 3.2 Calculated current contributed by photons in the DCM absorption range.

As is shown by these data, DBRs B to E have similar current outputs in this particular spectral region as compared to the control sample (see Table 1 for ΔI values, defined as the difference between the samples with and without a DBR), where Sample D performs the best, showing a relative enhancement of ~22%. For DBR A, the enhancement is the lowest as its stopband blocks the low-energy side of the absorption edge of the DCM dye. Its angle restriction property further limits its efficiency, being subject to higher path length dependent losses. The properties of DBR F are also limited for reasons that fall at the other limit. Here, the stopband red shift is too large to cover the dye emission effectively, even at very large incidence angles. As a result, the DBR reflectance drops significantly at oblique angles, which leads to a low photon recycling efficiency. To extend understandings of these optical effects, a Monte-Carlo ray-tracing model was constructed using measured material optical constants, with the reflectance for each DBR being calculated using the transfer matrix method. All of the features observed in the experimental EQE plots (Figure 3.8(a)) - stopband dips, diffuse light enhancements and the UV-blue region enhancements - are also well captured in the simulated EQE curves, as shown in the data presented in Figure 3.8(b).

The results of measurements of the total current output from the LSC device with each DBR are plotted in Figure 3.10(a) (black dots and line). The optimum system among these DBRs is that afforded by Sample D, with a central wavelength of 735 nm. From these data it is clear that the center wavelength of the DBR needs to be red-shifted substantially from the dye emission peak (600 nm) for best performance. For Sample D, the DBR stopband fully overlaps with dye emission at around 60 degrees incidence angles, indicating that the design of the photonic structure’s stopband should target photons in this range as they have the highest chance of being guided to the cell. The Monte-Carlo ray-tracing simulations affirm this interpretation. The results of simulations addressed to this point are shown plotted against the experimental data in Figure 3.10(a) (blue curve). The agreement in the general trend versus DBR central wavelength confirms the inferred trends in the efficacy of enhanced light trapping of the

LSC system. These results thus provide and affirm a theoretical guideline for designing a DBR with respect to the dye emission profile of the LSC. The relative current enhancements integrated from dye absorption range (300-580 nm) in EQE plots were plotted in Figure 3.10(b), demonstrating a similar trend to Figure 3.10(a), and further confirm the relationship between DBR center wavelength and device current enhancement.

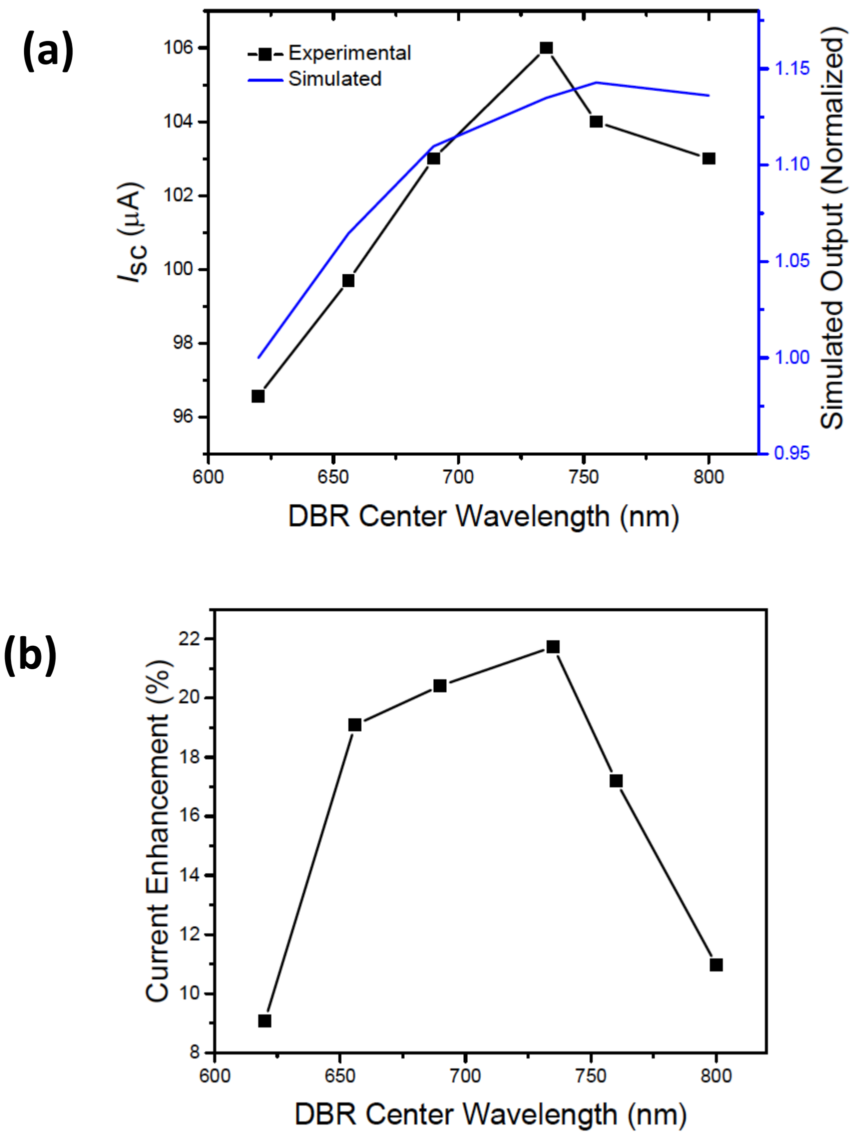

Figure 3.10

Figure 3.10 (cont.) (a) Both experimental and simulated enhancements show that the optimal stopband of DBR red-shifts from dye emission peak; (b) Relative current enhancements integrated from dye absorption range (300 to 580 nm) in EQE plots, DBR with a center wavelength of 735 nm shows the best performance.

In order to investigate light propagation behavior inside the LSC film, the device performance was also measured with a circular aperture centered on the solar cell while controlling the illumination area of the LSC device with DBR D affixed on top. The photocurrents extracted from these measurements are plotted as a function of aperture radius in Figure 3.11. At smaller aperture radii, the LSC without the DBR (black curve) performs better, as the stopband of the top photonic structure blocks incident light that can be waveguided to the device via non-TIR modes within short ranges. The DBR-LSC coupled device (red curve) exhibits a faster growth rate in the current output as the aperture area expands, outperforming the control device at larger radii. This indicates that a longer propagation distance of luminescent photons occurs inside the waveguide with a top photonic mirror being affixed, and thus illustrates a beneficial role for their use in improving performance in large LSC devices.

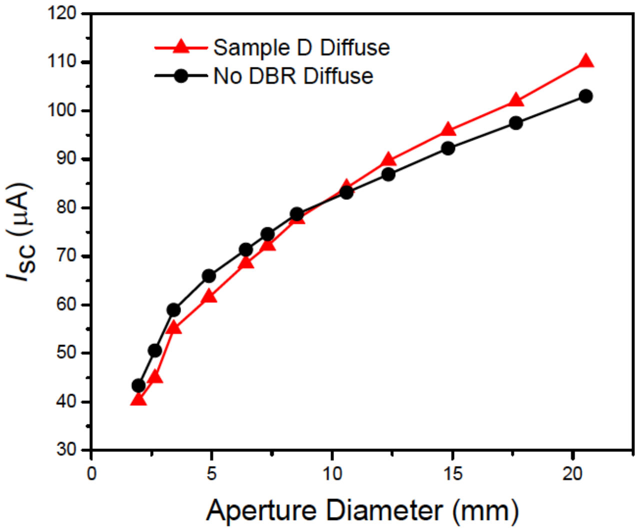

Figure 3.11

Figure 3.11 (cont.) LSC with a DBR shows faster increase in current output with increasing illumination area, indicating a longer photon propagation length.

3.4.2 High reflectivity distributed Bragg reflector

Inspired by the LSC performance enhancement by applying nanoparticle DBRs, we decided to optimize the design geometry and explore the full potential of photon recycling. On the basis of the properties of previously used QDs, we designed a distributed Bragg reflector that accepts incident blue sunlight and traps luminescence with much higher reflectivity. The DBRs were custom designed and purchased from Optical Filter Source, LLC (Austin, TX, USA). From 350 to 520 nm the photonic mirror exhibits 90% average transmission at normal incidence. Over the emission band of the lumophore, the hemispherically averaged reflectance of the mirror is 98%, with a maximum reflectivity of >99.999% at 650 nm at normal incidence. The dependence of reflectivity on angle of incidence is characterized in Figure 3.12; luminesced photons are reflected efficiently up to 60 degrees from normal, with diminished reflectivity at higher angles.

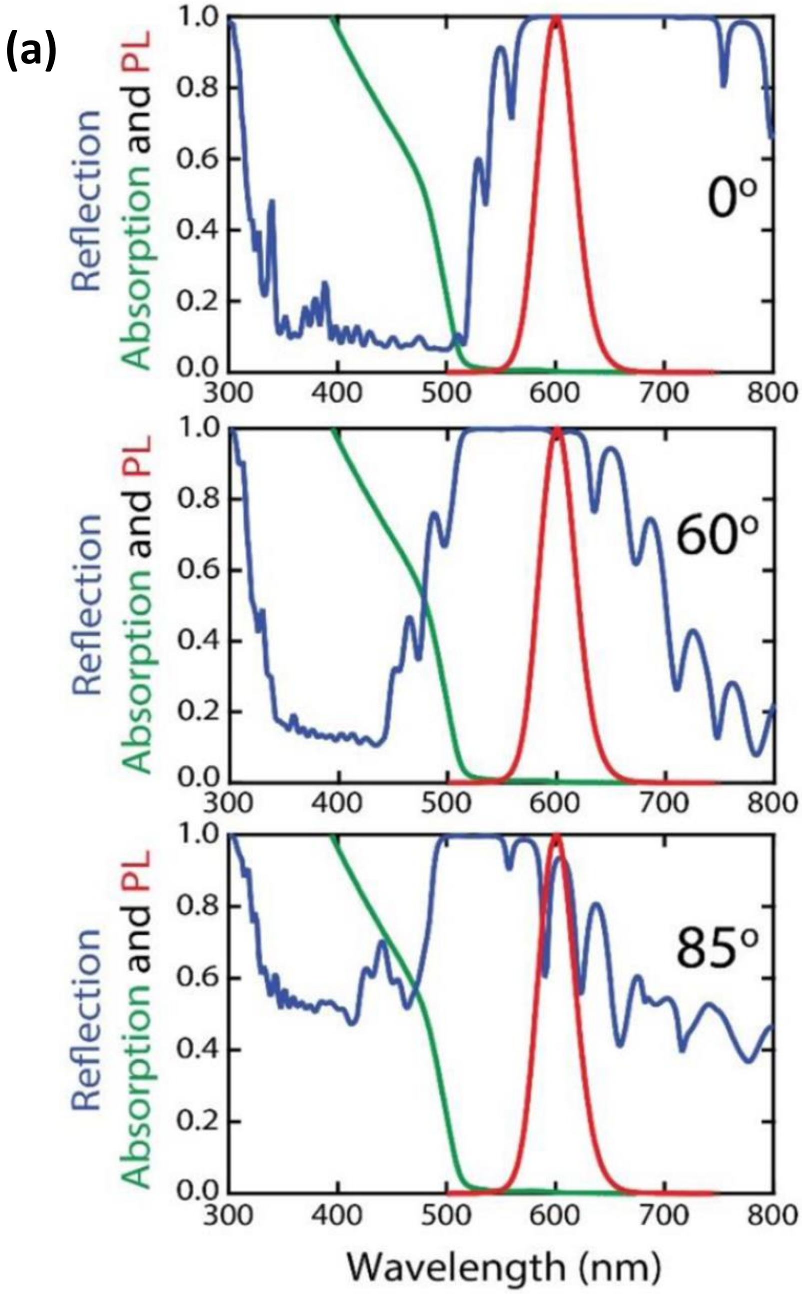
(a)
Reflection Absorption and PL
0.0
0.2
0.4
0.6
0.8
1.0
300
400
500
600
700
800
0°
60°
85°
Wavelength (nm)

Figure 3.12

(b)

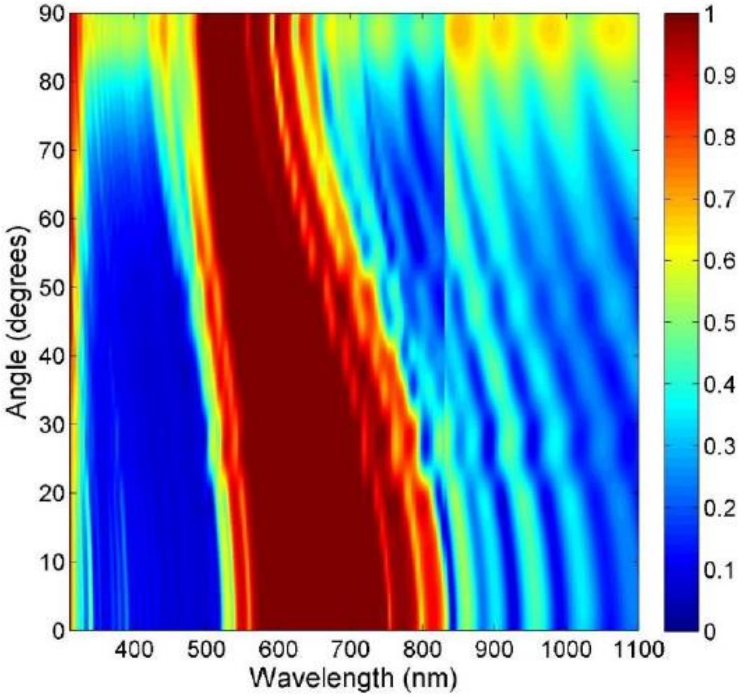

Figure 3.12 (cont.) (a) Absorption and emission spectra of the QDs as compared to the reflectivity of the photonic mirror at different incidence angles. (b) Measured DBR reflectivity as a function of angle and wavelength.

The photographs in Figure 3.13 show the effect of the photonic mirror on luminescence from the quantum dot solution under 440 nm laser illumination. In the first photograph, two mirrors are arranged in a tent over the cuvette and all luminescence is directed to the opening since it cannot pass through the mirror. In the second, the scattered blue laser light transmits through the mirror, while the luminescence from the luminophore solution is blocked.

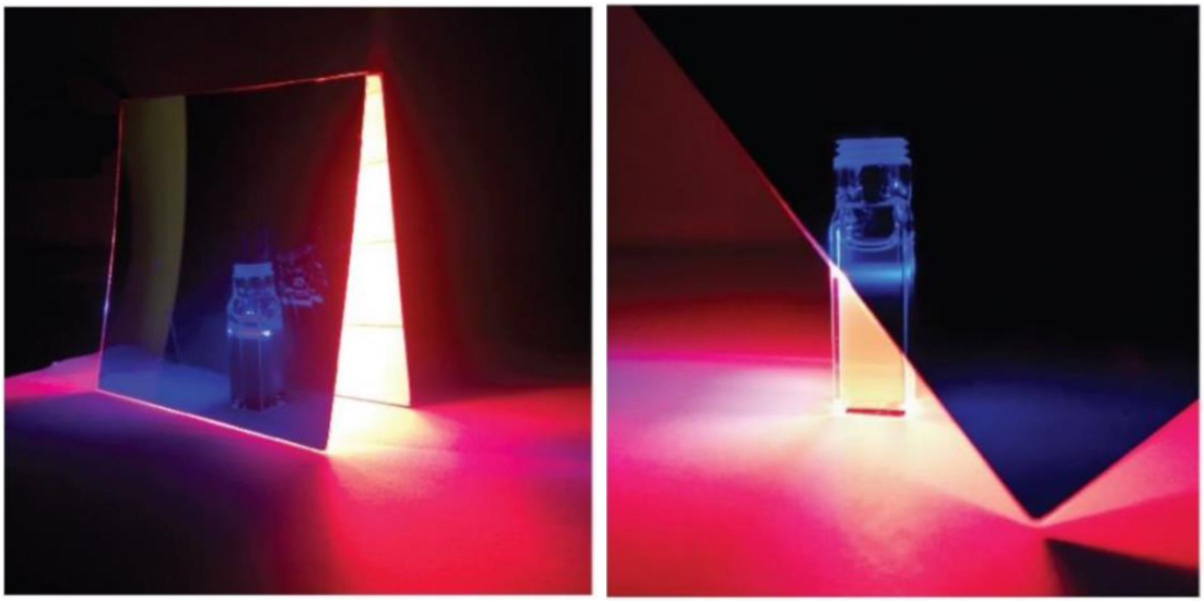

Figure 3.13 Photographs of the QD solution under blue laser illumination with photonic mirrors reflecting the luminesced red light.

Figure 3.14(a) shows the concentrator cavity, consisting of the wavelength-selective photonic mirror on top, a PLMA/QD waveguide with an embedded Si solar microcell, and a trench-shaped diffuse reflector that both enhances absorption of incident photons and recycles photons that escape through the bottom and edges of the waveguide. It is important to note that in this iteration the single Si microcell acts as a detector of the optical concentration. The overall EQE and collection efficiency of the device are low due to the small area covered by the single microcell. In the future, arrays of microcells could be integrated so as to capture more of the waveguided light with minimal shadowing. The best device performance under AM1.5G illumination is summarized in Table 3.3, with current density (J)-voltage (V) curves shown in Figure 3.14(b). Both the J_{sc} and the V_{oc} of the microcell increase significantly upon integration with the LSC including the trench reflector and increase further with the addition of the photonic mirror. The total J_{sc} of the Si microcell is 7.7 times higher after integration with the complete device. The spectral dependence of C is plotted in Figure 3.14(c) and shows that the current enhancement originates from concentration of blue photons, the spectral region where the nanocrystals absorb. From 550 to 800 nm C is greatly suppressed, as this spectral region is reflected by the photonic mirror and prevented from entering the LSC. This loss is outweighed by the improvement in the concentration of blue photons as demonstrated by the total current enhancement.

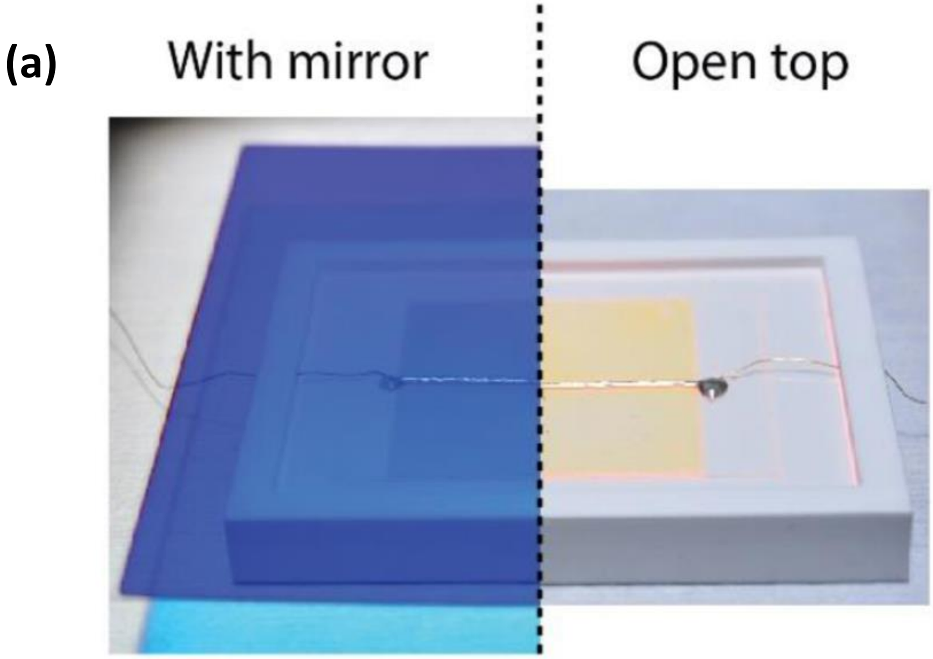

Figure 3.14

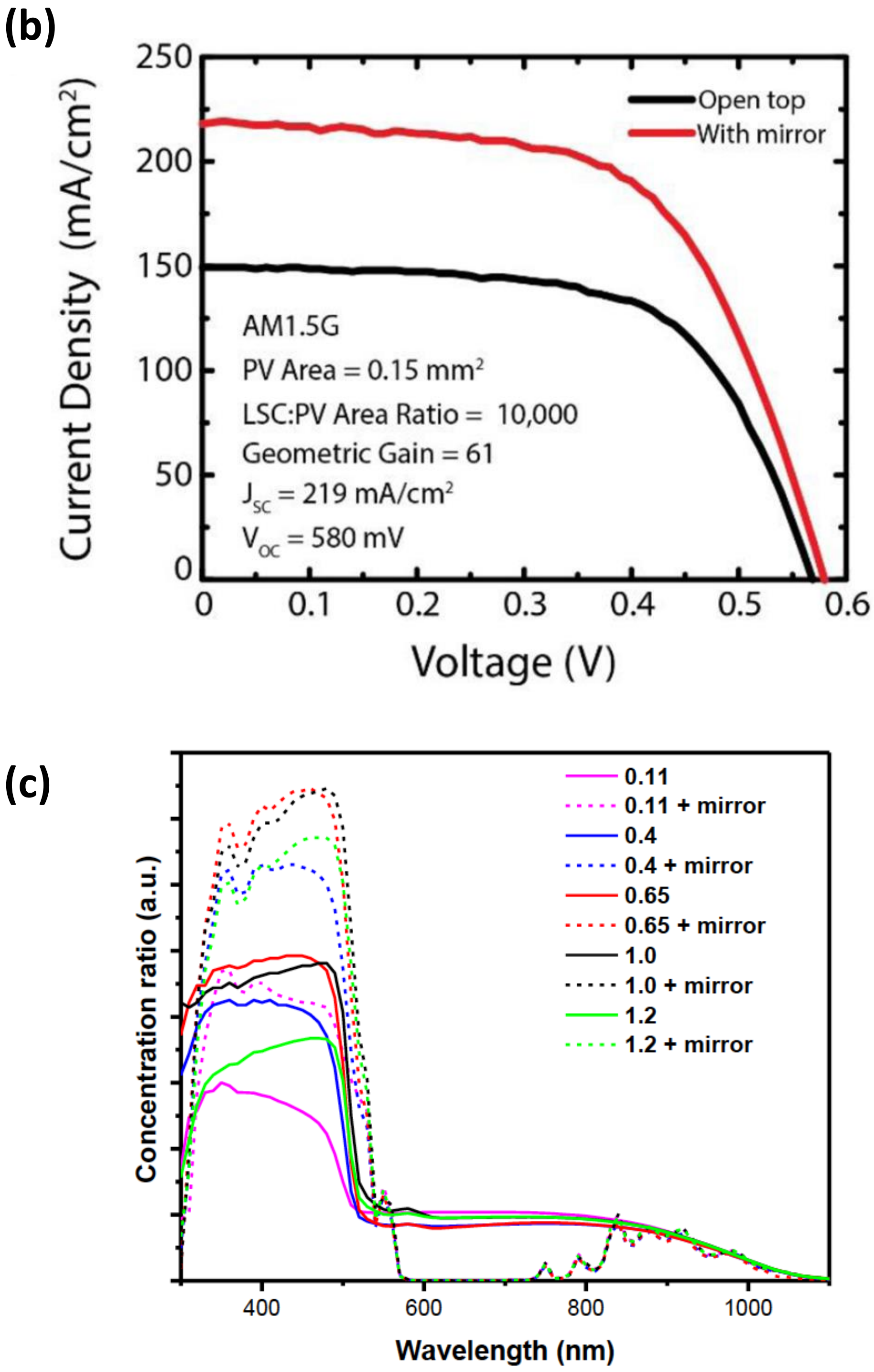

Figure 3.14 (cont.) (a) Photograph of a microcell-LSC integrated with a photonic mirror and a trench-shaped diffuse trench reflector; (b) Reflectance of the trench diffuse reflector; (c) concentration ratio as a function of excitation wavelength of the LSC-PV device with and without the photonic mirror.

Testing Condition	**J_{SC} (mA/cm^2)**	**Concentration 350-500 nm**	**V_{OC} (V)**	**Fill Factor**	**Power (mW/cm^2)**
μ-Si device	28.51	1	0.504	0.72	10.35
μ-Si device/LSC/trench reflector	149.3	18.9	0.569	0.64	54.37
μ-Si device /LSC/trench reflector/photonic mirror	218.7	30.3	0.580	0.61	77.38

Table 3.3 Summary of PV device performance before and after the integration with the LSC, trench reflector and photonic luminescence-trapping mirror under AM1.5G illumination.

The optical density (OD) at 450 nm of the QD-polymer films was then varied from 0.1 to 1.2 (Figure 3.15(a)), and the LSCs were characterized under blue-filtered illumination. The highest concentration factor occurs when OD = 0.65 (Figure 3.15(b)). At lower OD, absorption of incident sunlight in the blue portion of the spectrum is diminished, while at higher OD reabsorption and scattering of luminesced photons decrease the optical efficiency. All samples demonstrate more than 60% enhancement in C after applying the photonic mirror except the control device (no QDs added in the polymer). The optimum C under the blue-filter illumination with the photonic mirror reaches 30.3, a value unprecedented in the LSC literature.

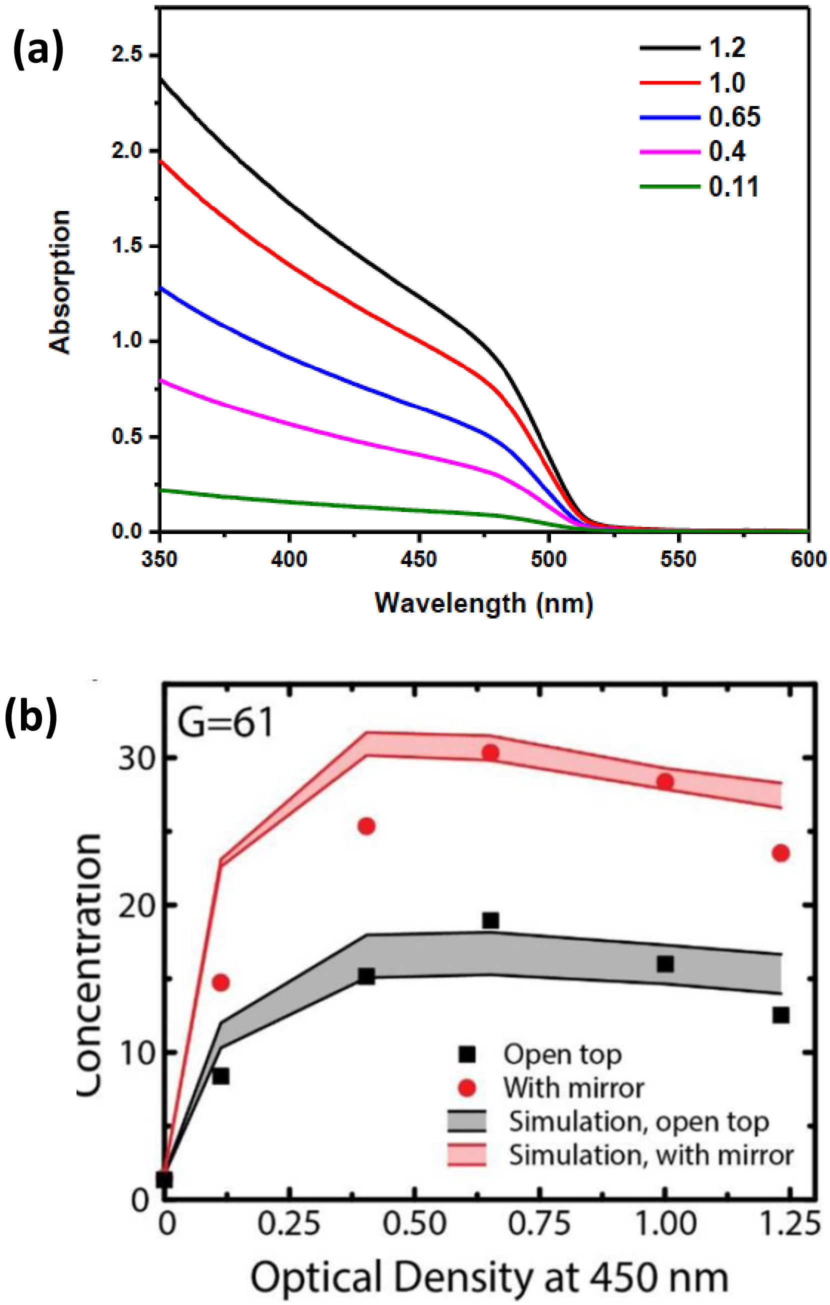

Figure 3.15 (a) Absorption spectrum of QD-polymer thin film with different QD loadings. (b) Experimental and simulated photon concentration ratios at different optical densities of QD, with a geometric gain (G) of 61.

To study the propagation of photons inside the LSC, we measured the propagating curve as a function of geometric gain G (the ratio of illuminated area to illuminated edge area) for all six samples. The results are shown in Figure 3.16. It can be seen that for all the samples the concentration ratios increase linearly. We also compared a sample with high internal scattering (Figure 3.17(a), due to the absence of thorough QD cleaning before polymerization) to one with low scattering (Figure 3.17(b)). Both samples had an optimal OD of 0.65 at 450 nm and were measured under blue-filtered illumination with a variable illumination spot diameter, resulting in variable geometric gain. Without the photonic mirror acting as a photon-recycling element, the sample with high scattering (Figure 3.17(a)) shows a limited growth of C that quickly plateaus with increasing G, as luminesced photons are scattered out of the waveguide and lost. In comparison, the sample with low scattering exhibits a quasi-linear increase of C with G (Figure 3.17(b)), as contributed by the uninterrupted TIR modes inside the waveguide.

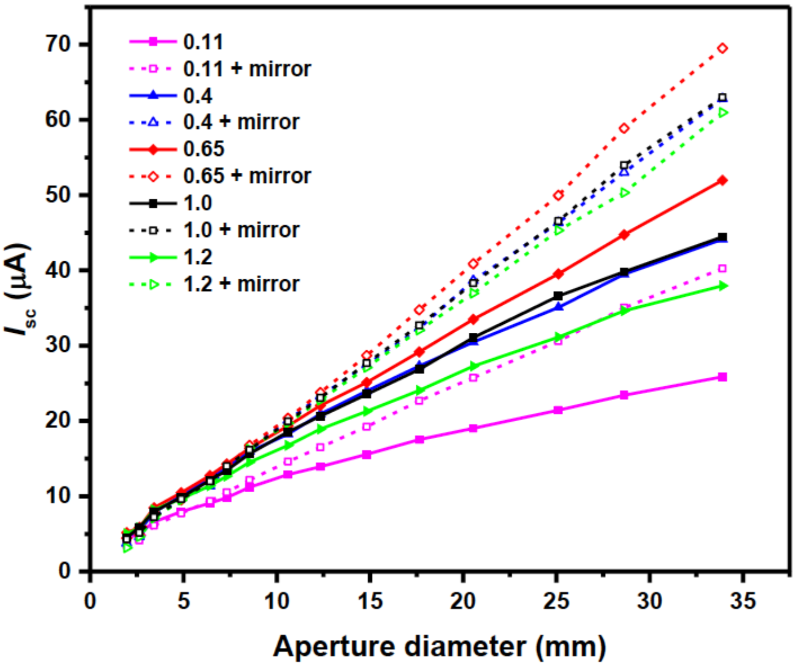

Figure 3.16 Photocurrent of the LSC device under the blue filtered illumination at various aperture size.

Adding the photonic mirror on top allows both non-TIR and scattered photons to be recycled and then to propagate inside the concentrator cavity before finally reaching the solar cell. As a result, the losses associated with scattering are strongly reduced, and photons are concentrated over distances much longer than the scattering length of the waveguide. In the high-scattering case (Figure 3.17(a)) C becomes quasi-linear with increasing G and reaches 16 at G = 37, nearly 5 times higher than without the mirror. This value is still smaller than that in the low-scattering case (C = 20), indicating that scattering loss is not completely mitigated as the mirror reflectivity diminishes at oblique angles. Measurement of the luminescent concentration factor of the high-scattering sample with the dielectric mirror at G = 61 resulted in C = 26, only slightly reduced from the best value of 30.3 for the nonscattering device. In the device with low scattering (Figure 3.17(b)), C increases superlinearly with the illumination diameter, increasing faster than the TIR limit imposed by Fresnel equation. This superlinearity marks the onset of a transition from ballistic, single-pass photon transport to diffusion-based transport afforded by photon recycling. Our results suggest that efficient trapping of luminescence with a dielectric mirror can keep the luminescence inside the cavity regardless of the optical clarity and smoothness of the waveguide. If the optical quality of the waveguide could truly be made irrelevant by the dielectric mirror, the fabrication of the devices could be simplified.

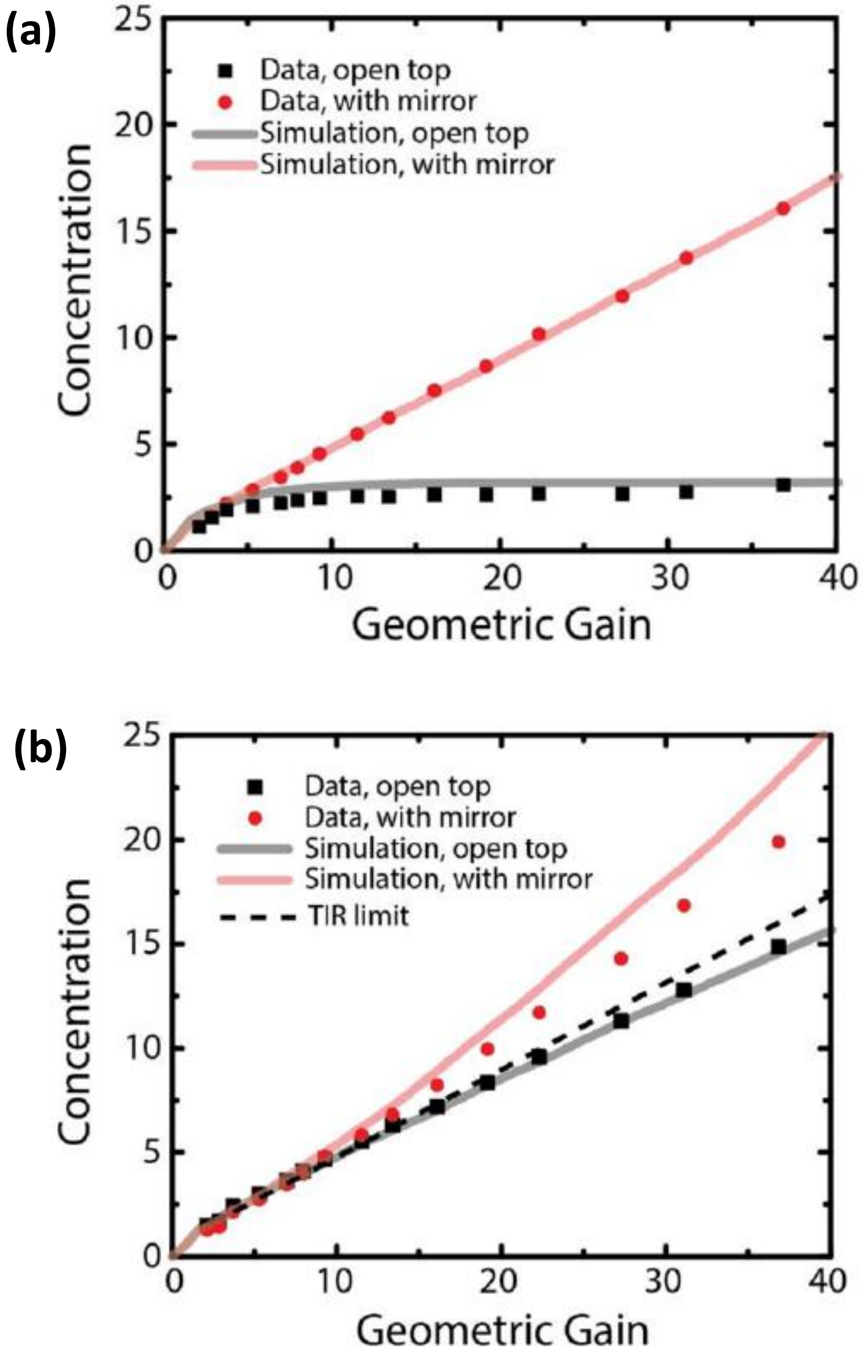

Figure 3.17 High scattering (a) and low scattering device (b) propagation curve with and without DBR.

To further investigate the connection between photon scattering, the photonic mirror, and C, we used a Monte Carlo ray tracing model. The mechanism of the ray tracing model will be discussed in detail in later chapter. These simulations assume that scattering derives from the refractive index contrast between the nanocrystals and the PLMA waveguide. For each device, a range of scattering lengths are simulated and fit to the experimental data. All other model inputs are measured experimentally. For the high- and low-scattering devices (Figure 3.17), the best fit is achieved with 0.18 and 3 mm scattering lengths. A scattering length of 3 mm corresponds to roughly one scattering event for a photon propagating at 19 mm from the edge of the waveguide to the solar cell.

3.5 Future directions

The device fabricated here is tuned to utilize the blue portion of the spectrum due to the choice of appropriate organic dye, as well as engineered absorption spectrum of the luminophore. The system efficiency remains limited, as only one silicon microcell is utilized to detect rather than fully convert the luminescence in the waveguide. Using transfer-printing-based assembly, however, arrays of these microscale devices could be embedded in the waveguide to dramatically enhance the PV conversion efficiency. Coupling with III–V (e.g., InGaP) microcell arrays with band gaps tailored to match the luminophore emission, a luminescent concentrator cavity module could be constructed with efficiencies comparable to conventional PV panels but with reduced materials consumption. Additionally, this LSC module can be potentially used as the top layer (e.g., over Si) in a mechanically stacked multijunction architecture for full spectrum conversion, utilizing both the high-energy photons in the LSC and the low-energy photons in the bottom photovoltaic. We expect that future devices will achieve even higher concentration ratios while maintaining high waveguide efficiency through improvements to the luminescence quantum yield, waveguide geometry, and photonic mirror design. Thus using a luminophore with a larger Stokes shift and narrower emission bandwidth (such as obtained with core-shell quantum dots or quantum rods) and selective, omnidirectional (e.g. meta-surface) reflectors could potentially lead to much higher photon recycling and conversion efficiencies for LSC-based solar concentrators.

CHAPTER 4: QUANTUM DOTS PHOTONIC CRYSTAL

In this work, we demonstrate an approach in which visible-wavelength-emitting quantum dots are integrated within a polymer-based photonic crystal and excited by an ultraviolet-emitting LED. The PC design incorporates two interleaved regions, each with distinct periods in orthogonal directions. The structure enables simultaneous resonant coupling of ultraviolet excitation photons to the QDs and visible QD emission at two different wavelengths to efficiently extract photons normal to the PC surface. The combined excitation and extraction enhancements result in a 5.8X increase in the QD output intensity. Further, we demonstrate multiple QD-doped PCs combined on a single surface to optimally couple with distinct populations of QDs, offering a means for blending color output and directionality of multiple wavelengths. Devices are fabricated upon flexible plastic surfaces by a manufacturable replica molding approach.

4.1 General introduction to photonic crystal

Usually, the conventionally structured white light-emitting-diodes (WLEDs) rely on a three-ways coupling techniques of GaN-based blue LEDs, yellow-red phosphors and organic materials encapsulation. But it often suffers from awkward predicaments, such as the relatively high fabrication cost of conventional yellow and red phosphors and comparatively low robustness due to peripherally organic encapsulating materials. These limitations greatly hampered the further commercially expanding of WLEDs. Various researchers have demonstrated an alternative approach for fabrication of high-performance phosphors-free WLEDs by using QD-polymer as color conversion layer. The narrow emission, high quantum yield, tunable emission spectrum and high photostability render QDs promising materials to achieve high quality WLEDs.[70-73]

A photonic crystal (PC) is a periodic optical nanostructure that affects the motion of photons in much the same way that ionic lattices affect electrons in solids (Figure 4.1). Photonic crystals occur in nature in the form of structural coloration-and, in different forms, promise to be useful in a range of applications. In 1887 the English physicist Lord Rayleigh experimented with periodic multi-layer dielectric stacks, showing they had a photonic band-gap in one dimension. Research interest grew with work in 1987 by Yablonovitch and John on periodic optical structures with more than one dimension-now called photonic crystals.[74-75]

When externally incident light interacts with PCs in the subwavelength regime, only the zeroth-order forward- and backward-diffracted waves can propagate. However, the periodicity also allows for phase-matching of higher (evanescent) orders to localized leaky modes supported by the PC. Once excited, the leaky modes, defined by a complex propagation constant, possess a finite lifetime as they are diffracted in both the forward (transmitted) and backward (specular) directions. The backward re-radiated waves are in phase and constructively interfere with the zeroth backward-diffracted order, whereas the forward re-radiated waves are out of phase with the zeroth forward-diffracted order by π radians, causing destructive interference and consequently zero transmission. Thus, the external excitation of leaky modes is associated with a 100% reflection phenomenon for a resonant wavelength, assuming a defect-free, lossless system. As the excited leaky modes are localized in space during their finite lifetimes, they can be engineered to have very high energy density within regions of the PC at resonance. The magnitude of this energy density is directly related to the resonant mode lifetime or Q-factor of resonance, which in turn can be controlled by adjusting the device parameters. The intensity of emission of fluorescent species (which are absorptive at the resonant wavelengths) can be greatly enhanced by placing them in proximity to regions where the resonant modes concentrate most of their energy.[76]

The existence of leaky modes overlapping the fluorescence emission spectrum opens up pathways for the emitted light to escape into free space. As well as direct emission, the fluorescence can now couple to the overlapping leaky modes and Bragg scatter out of the structure, thereby greatly reducing the amount of light trapped as guided modes compared with an unpatterned substrate.[77] If the dispersion of these overlapping leaky modes is close to the Γ-point band edge, that is, $K_{\parallel}$ (magnitude of the in-plane wave vector) ~ 0, most of the emitted light will be extracted within small angles to the surface normal. More generally, appropriately engineering the leaky dispersion of the PC facilitates the funneling of guided light into regions of space where it can be easily detected. It can thus be appreciated that enhancement of fluorescence can be achieved in two steps: enhanced excitation and enhanced extraction.

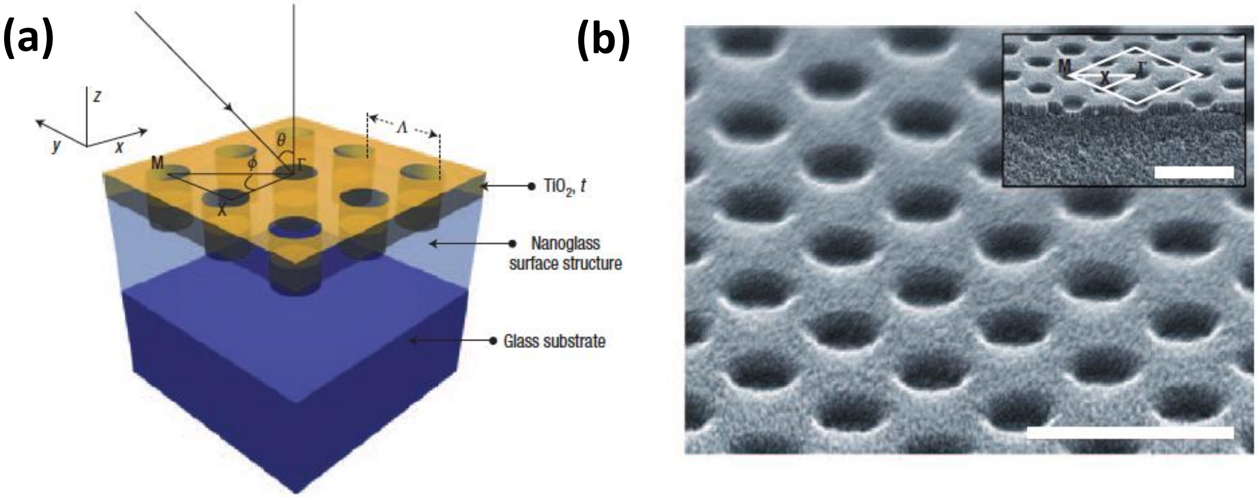

Figure 4.1 Visible-wavelength two-dimensional PC slab design and fabrication. (a) Layout of the two dimensional PC device. (b) Scanning electron microscope images of a sample fabricated by the nanoreplica molding approach. Scale bars are 500 nm.

Photonic crystals can be fabricated for one, two, or three dimensions. One-dimensional photonic crystals can be made of layers deposited or stuck together. Two-dimensional ones can be made by photolithography, or by drilling holes in a suitable substrate. Fabrication methods for three-dimensional ones include drilling under different angles, stacking multiple 2-D layers on top of each other, direct laser writing, or, for example, instigating self-assembly of spheres in a matrix and dissolving the spheres. Photonic crystals can, in principle, find uses wherever light must be manipulated. Existing applications include thin-film optics with coatings for lenses. Two-dimensional photonic-crystal fibers are used in nonlinear devices and to guide exotic wavelengths. Three-dimensional crystals may one day be used in optical computers.

Photonic crystals are attractive optical materials for controlling and manipulating light flow. One dimensional photonic crystals are already in widespread use, in the form of thin-film optics, with applications from low and high reflection coatings on lenses and mirrors to color changing paints and inks. Higher-dimensional photonic crystals are of great interest for both fundamental and applied research, and the two dimensional ones are beginning to find commercial applications.

The first commercial products involving two-dimensionally periodic photonic crystals are already available in the form of photonic-crystal fibers, which use a microscale structure to confine light with radically different characteristics compared to conventional optical fiber for applications in nonlinear devices and guiding exotic wavelengths. The three-dimensional counterparts are still far from commercialization but may offer additional features such as optical nonlinearity required for the operation of optical transistors used in optical computers, when some technological aspects such as manufacturability and principal difficulties such as disorder are under control.

There are a broad range of application-specific needs for lighting and display technologies, given their prevalence in our homes, workplaces, and pockets. Precisely engineered control of the output spectrum of lighting products is desired to match the requirements for color temperature and output directionality, while at the same time optimizing power efficiency and manufacturing cost. For video display applications, controlling the blend of primary colors in each pixel is necessary, while the control of pixel output directionality must be tailored for a range of viewing methods that may be either tightly confined (for privacy) or widely dispersed (for wide viewing angle).

Precisely engineered control of the output spectrum of lighting products is desired to match specific requirements for color temperature and output directionality, while at the same time optimizing power efficiency and manufacturing cost. As the effects of polarization, wavelength, and directionality within periodic dielectric structures are characterized, various applications continue to emerge for optical resonators using PC structures.[78-81] By varying the duty cycle, period, and refractive index, the resonant characteristics of a PC can be tuned to interact with wavelengths extending from the ultraviolet to the infrared. These properties have been used for a variety of applications including polarizers, filters, biosensors, optical communication components, displays, and lighting.[82-86] PCs have been incorporated into light emitting diodes (LEDs) in order to increase extraction efficiency, and to control the directionality of light output, either normal to the device or into angular sidelobes.[87-91]

With an appropriate choice of dielectric materials and dimensions, the resonant modes of a PC can be engineered to occur at specific combinations of angle and wavelength. This allows light of the selected wavelength and incident direction to couple to the PC and excite a highly localized electromagnetic standing wave with amplitude that is substantially greater than the original illumination source. Enhanced excitation will occur by placing emitters within the region with an increased electric field magnitude at their excitation wavelength. Because the guided modes will couple in and out of the PC under phase matching conditions for specific combinations of wavelength and incident angle, it is possible to collect light at the outcoupling angle more efficiently, and thus providing an enhanced extraction mechanism.[92] QDs that down-convert light from a broad band of excitation wavelengths to a very specific emission wavelength, have been successfully incorporated into PCs with specific resonances designed to couple to the relevant excitation and/or emission wavelengths of the QDs.[93-94] By introducing two-dimensional variation into the PC structure, through the use of different periods in orthogonal directions, a PC may incorporate multiple resonances at widely varied wavelengths so as to interact simultaneously with the excitation and emission spectra of the integrated QD emitters as a means of enhancing the number of photons generated by each QD, while increasing the efficiency of emitted photons that reach the viewer. In this work, we demonstrate an approach, shown in Fig. 1(a), which incorporates one or more types of QDs into a replica-molded flexible polymer-based PC structure that is excited by a UV backlight LED.

The UV excitation source couples to a resonant mode of the PC, which creates an enhanced excitation at the coupling wavelength by increasing the magnitude of the electric field experienced by the QDs in the PC, thus producing greater photon output than would occur without a PC structure. The rectangular lattice of the PC is designed to produce a resonance at the wavelength of QD emission, resulting in photon emission that is efficiently channeled normal to the PC surface. As shown in Figure 4.2, we designed and fabricated an interleaved surface in a checkerboard pattern, containing two PC designs. While both regions are designed to produce resonances for the same UV excitation wavelength, each region is optimized for a different QD emission wavelength. This is a novel device structure that allows multiple types of QDs to experience simultaneous enhancement in a single device structure. Such a structure can enable a customized output spectrum through control of the enhancement wavelengths and the relative surface area of each PC region.

4.2 Photonic crystal design

The device structure interleaves the regions of two distinct 2D PCs in a checkerboard pattern. Each region consists of rectangular cavities, as shown in Figure 4.2, with resonances created by the periodic variation in the orthogonal directions on the surface. Each region varies in one direction with dimensions selected to provide enhancement from the same UV excitation source (200 nm period with 40% and 70% duty cycles in Regions 1 and 2, respectively), while the orthogonal directions have larger feature sizes for producing resonances at visible wavelengths. The larger features in Region 1 have a lateral width of 250 nm to produce resonances at $\lambda = 490$ nm, while the features in Region 2 have a lateral width of 340 nm, designed to produce resonances at $\lambda = 590$ nm. For both regions, the structure is formed from a QD doped polymer with a grating depth of 80 nm that is coated with an 85 nm thin film of TiO_2. While the period of the structure is the main determinant of the resonant wavelength, the resonances can also be tuned via control of the TiO_2 thickness.

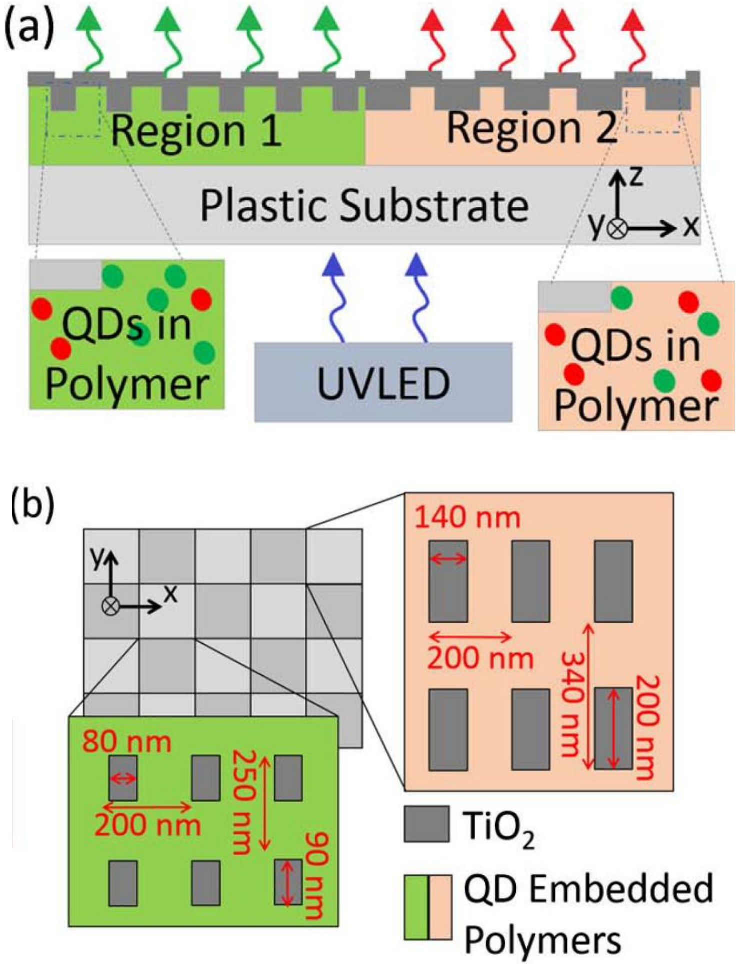

Figure 4.2 (a) A cross-sectional schematic of the device structure where a backlight UV LED source illuminate multiple regions. (b) A top down schematic of the two interleaved regions of the device with TiO_2 and their respective feature sizes.

4.3 Fabrication of quantum dots embedded photonic crystal device

A silicon wafer was fabricated to serve as a master mold template for the replica molding process. The master's grating structure was fabricated via electron beam lithography on a layer of thermal SiO_2 on a Si wafer, upon which reactive ion etching was used to produce 80 nm tall pillars. The patterned device area was 3 × 3 mm^2. The master wafer was cleaned with a piranha solution for 20 min, rinsed with DI water, and dried with N_2. Next, a vapor-phase deposition of (tridecafluoro-1,1,2,2-tetrahydrooctyl) trichlorosilane (no-stick) was performed by placing the wafer into an enclosed container with two drops of the No-Stick solution for 1 h.

CdSeS/ZnS alloyed QDs were purchased from Sigma-Aldrich (1 mg/mL in toluene, oleic acid as ligand), or synthesized for this application by collaborators. Lauryl methacrylate (LMA) and ethylene glycol dimethacrylate (EGDMA) were purified to remove the inhibitor with an inhibitor removal column before their use. The UV curable polymer, consisting of 182 µL of LMA and 18 µL of EGDMA, was mixed in a flask, and 4 mL of QD hexane solution and 8 µL oleic acid was added and mixed well, then 20 µL PLMA monopolymer solution was added to increase the solution viscosity. The remaining solvent was removed using a rotavap at room temperature and 2 µL of initiator (Darocur 1173) was added immediately before spin coating. The solution was spin coated onto the master wafer at 600 rpm for 30 s, then immediately polymerized by exposure to a high intensity UV lamp for 30 min in a nitrogen atmosphere glovebox. After the film was fully cured, a layer of NOA 61 was drop coated over the composite film. An acetate sheet substrate was then placed over the master wafer and brought into contact with the uncured NOA drops to form a thin continuous layer between the acetate sheet and the composite thin film. Next, the NOA was cured for 20 min using a UV lamp under ambient conditions. The acetate substrate, along with the NOA layer and composite thin film, was then released from the master wafer with the thin film of QD-PLMA containing the replicated 2D cavity structure. After replica molding, TiO2 is deposited by sputtering to the depth required for resonance at the desired wavelength. Deposition times were restricted to keep the substrate temperature from exceeding 40°C, to avoid thermally induced damage to the polymer materials. Figure 4.3 shows the top-down SEM photograph of the silicon master wafer and final devices.

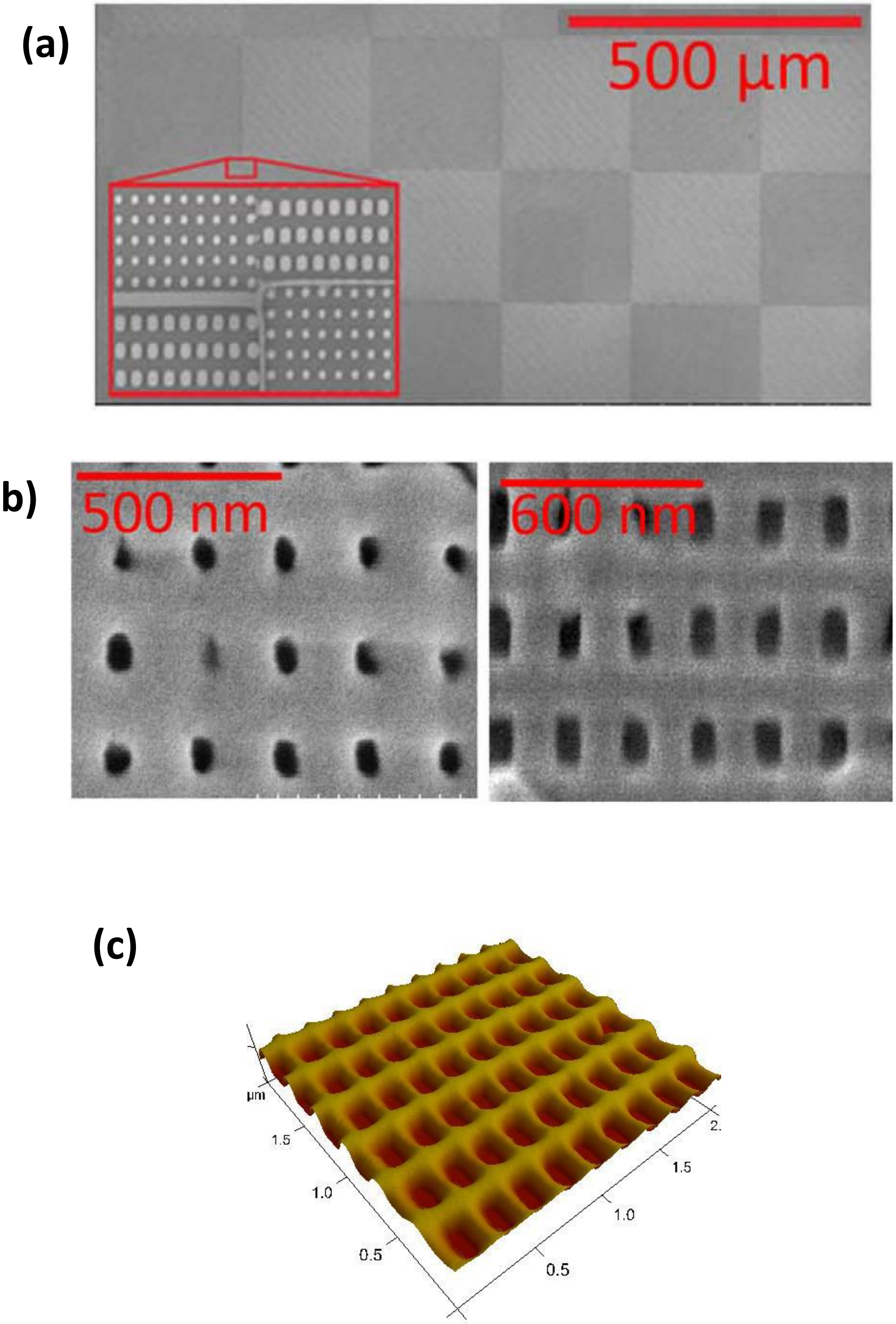

Figure 4.3 (a) An SEM of the replica molding master. The inset shows the pillars of the two regions at diagonal corners within the master structure. (b) SEM images of both Region 1 (left) and Region 2 (right) from the device after TiO_2 has been deposited to form the PC. (c) AFM images of PC surface.

The emission properties of the devices were measured using a UV LED centered at 375 nm with a 20 nm full-width half-maximum as the excitation source. A 350-390 nm bandpass filter was used to eliminate any non-UV emission from the LED. The LED output was collimated before illuminating the PC. The device was mounted over a cover with a 3 mm diameter aperture, assuring that only the patterned PC region was excited and measured.

4.4 Quantum dots output enhancement

The device under test was mounted to a motorized rotary stage, allowing the incident excitation angle to be varied. The output passed through a UV filter to eliminate any light from the excitation source, then was collected by a collimating lens attached to an optical fiber. The fiber was connected to a spectrometer (USB2000+, Ocean Optics) from which the emission can be measured and observed through the LabView OmniDriver software which also controlled the rotation position of the stage in 0.1 degree steps. To measure the impact of the extraction angle, the same equipment was used, but instead of mounting the PC sample to a rotation stage and varying the excitation angle, the PC sample position was fixed. The collimator coupled to the optical fiber was instead mounted on the stage and rotated around the PC, allowing extracted light to be collected over a range of angles with respect to the PC surface. The photonic band diagram of a device was determined using the same experimental setup as that to measure the excitation output, but the UV LED and associated bandpass filter were replaced with a tungsten-halogen lamp coupled to an optical fiber that outputs unpolarized light through a collimator, then the broadband transmission was measured across a range of angles.

In a sample with QDs emitting at a peak wavelength of $\lambda = 505$ nm, the extraction was measured before and after a deposition of 20 nm of TiO_2 to compare the output intensity with and without a photonic crystal structure, as shown in Figure 4.4. A narrow, angle-dependent extraction enhancement is shown, in addition to a broader excitation enhancement. In the inset, a scan of the output intensities for λ = 450-550 nm across a range of angles is shown in a device with a 20 nm TiO_2 thin film coating. In the main plot, the angle dependence of the output at λ = 505 nm is shown. With no PC present, the output emission of the quantum dots is lower. In the structure with the PC, there is a strong angle-dependent enhancement of a factor of 2X centered at -2 degree off normal incidence, representing the angle and wavelength combination at which the QD emission is enhanced through resonance with the PC.

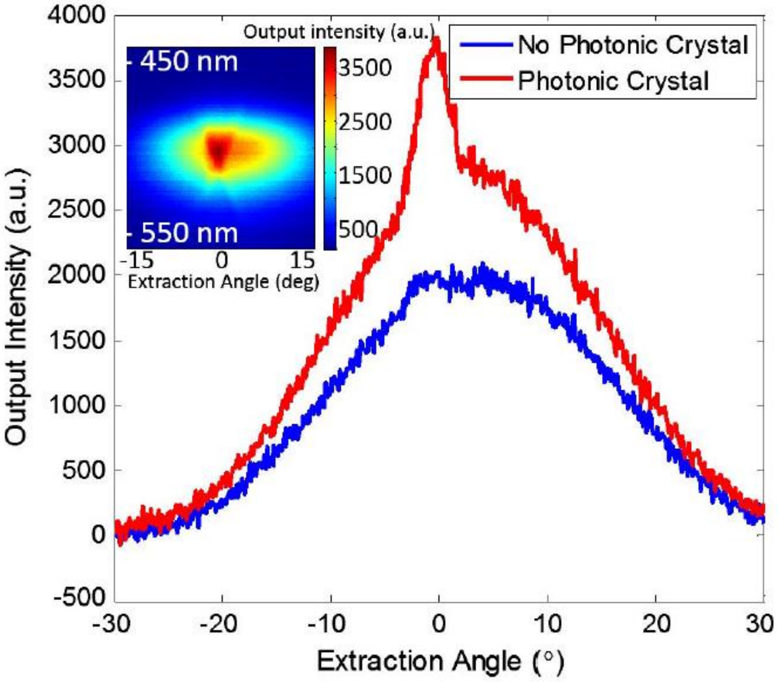

Figure 4.4 Impact of angle on QD extraction measured with and without a PC structure present.

Another sample was fabricated with a homogeneous mixture of QDs, with emissions centered at λ = 490 nm and λ = 585 nm. This mix demonstrated the ability of the PC to selectively enhance a subpopulation of embedded QDs. The emission was measured on a QD-doped grating structure without PC resonances by measuring the emission of a structure without TiO_2 (Figure 4.5(a)) and after the PC is formed by deposition of a 43 nm TiO_2 thin film. The maximum QD emission increased by 4 times for the

490 nm QDs and 5 times for the 585 nm QDs, shown in Figure 4.5(b), but only within the regions in which their emission matched their corresponding PC resonance. To adjust the resonance conditions of the PC for enhancing the emission wavelengths of both types of QDs, an additional 42 nm of TiO_2 was deposited, and that resulted in a total increase of 4.2X for the 490 nm QDs and 5.8X for the 585 nm QDs (Figure 4.5(c)), as the resonance conditions of the PC were redshifted by the thicker TiO_2 layer. After the final TiO_2 deposition, the band structure of the PC was measured using the broadband source, as shown in Figure 4.5(d).

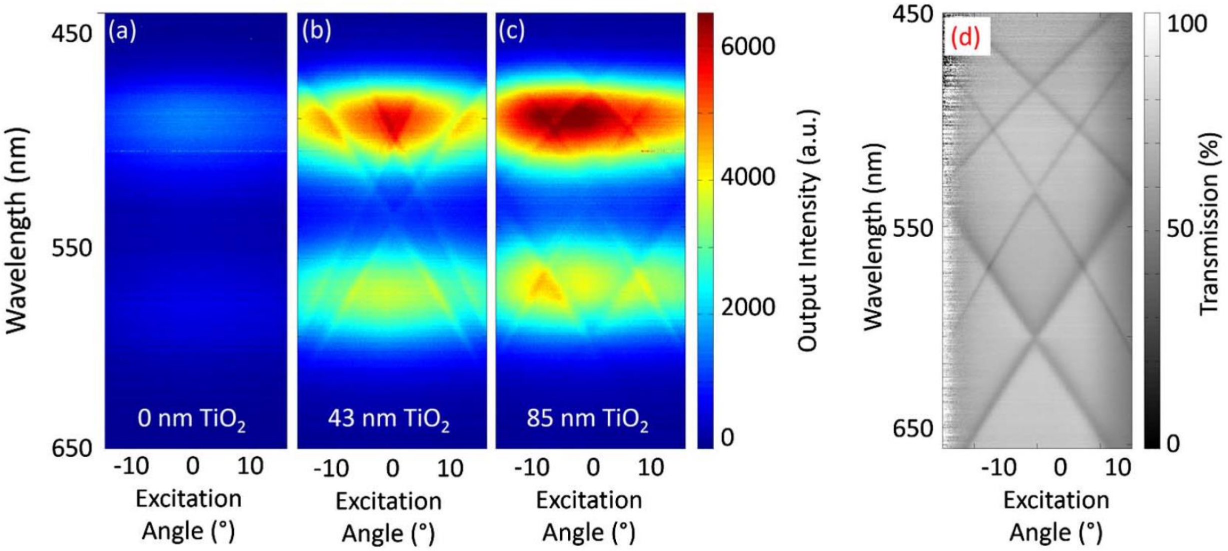

Figure 4.5 Comparison of the angle dependence of excitation at different stages of TiO_2 deposition, as the thickness enables tuning of the resonance conditions. (a) Measured output intensity with no PC structure. (b) Measured enhancement from a PC with a 43 nm thick TiO_2 layer. (c) Measured enhancement from a PC with an 85 nm think layer of TiO_2. (d) Transmission spectrum with an 85 nm think layer of TiO_2 confirms the locations of the peak resonance as measured by the varied excitation output intensity in (c).

Because the device structure has a different period in each orthogonal direction, the transmission efficiency can be measured over the range of angles across θ that vary with the shorter, UV resonant features or the Φ angle with the larger features that couple to visible wavelengths. The difference in the two photonic bands is shown in Figure 4.6. In Figure 4.6(a), the angle θ is varied, and there is an angle-dependent resonance in the UV, while the resonance in the visible is constant for all wavelengths, regardless of angle. This occurs because there is no angle variation experienced by the features responsible for coupling to those wavelengths. A similar situation occurs in Figure 4.6(b) with constant wavelength resonance occurring in the UV wavelengths, while varying the angle Φ experienced by the PC only changes its coupling to the larger PC features and shows angle-dependent variation at wavelengths greater than λ = 450 nm. The enhancement of QDs in a region with PC coupling is substantial enough to be easily visible to the naked eye. Figure 4.7 shows photographs of two dual region QD-doped PCs with emissions at from λ = 490 and λ = 590 nm. The brighter regions are providing both enhanced excitation and extraction for the embedded QDs. The alternate regions have a resonance condition of the PC that is coupling only to the excitation wavelength, and appears darker due to the lack of an extraction enhancement.

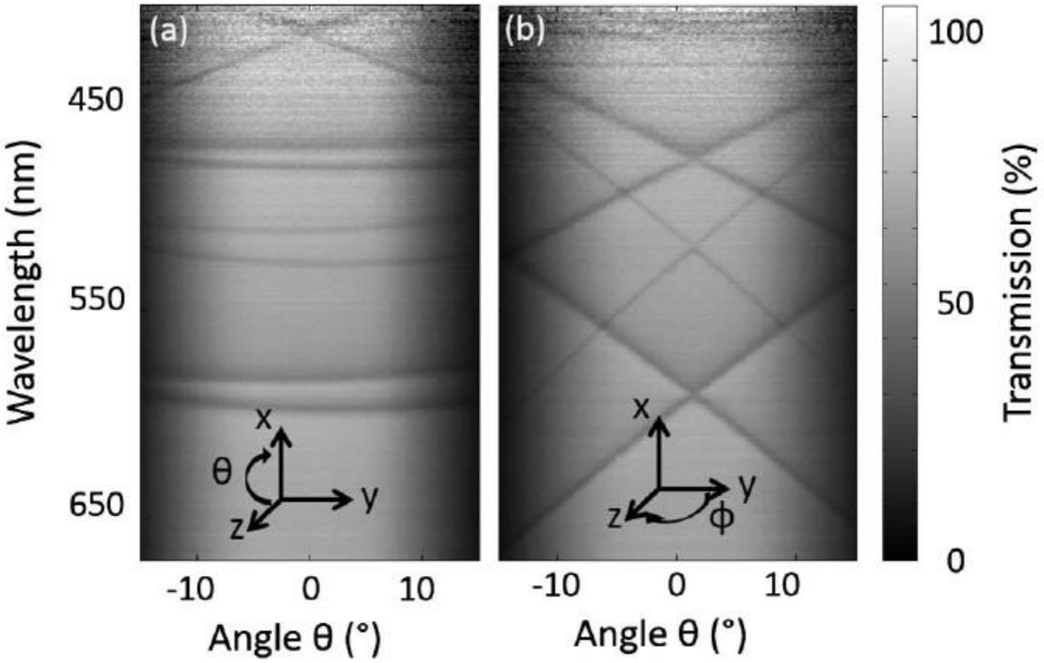

Figure 4.6

Figure 4.6 (cont.) (a) transmission measured only with angle variation along θ direction. (b) transmission measured only with angle variation along Φ direction.

The QD excitation measurements for structures with and without a PC structure all showed a slightly asymmetrical output, which corresponded to asymmetrical output intensity from the UV-LED source. This can be seen in Figure 4.4, where the peak extraction occurs at -2° from normal incidence. This narrow peak is angle dependent, and shows a factor of 2 enhancement in output emission with the photonic crystal present, while the broader enhancement across all measured angles is due to the enhanced excitation over the entire PC area. The extraction enhancement occurs only in the PC region, but both regions have resonances at the UV excitation wavelength and so contribute to the enhanced excitation. As shown in Figure 4.6, the UV and visible resonances show angle dependence in orthogonal directions, so it is expected that the enhanced excitation shows little angle dependence when varying the extraction angle.

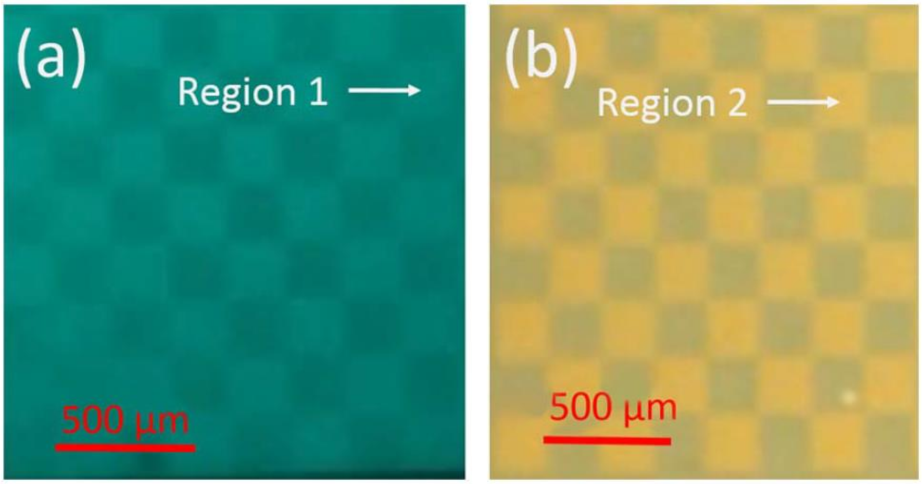

Figure 4.7 Photographs of quantum dot enhancement within the checkerboard of PC regions. (a) The QD emission at λ = 490 nm is brighter in Region 1, where both the excitation and extraction are being enhanced, compared to Region 2, in which only enhanced excitation occurs. (b) A sample with a mix of

Figure 4.7 (cont.)

QDs emitting at λ = 490 nm and λ = 590 nm. The yellow QDs in Region 2 dominate the output, because the peak extraction enhancement for λ = 490 nm in Region 1 is directed away from normal, resulting in reduced intensity when observed from above the PC.

By adjusting the thickness of the TiO_2 layer, the resonance conditions can be easily tuned. As shown in the varied depositions in Figure 4.5(a-c), a thicker layer redshifts the resonance wavelength of the structure. Figure 4.5(d) shows the photonic band diagram of the structure with the total 85 nm of TiO2, where the darker bands indicate the wavelength and angle coupling leading to resonance within the PC. These bands correspond to the bands of enhancement seen in Fig. 4.5(c) within the QD emission. Devices using the PC structure demonstrated in this work combine excitation and extraction enhancement for an increase of up to 5.8X as compared to the QD output produced with no PC structure present. There is an expected difference between the improvements in excitation and extraction, given that the QDs are dispersed through both regions of the PC structure. Therefore, the QDs in every region experience enhancement of the UV excitation wavelength, but the output wavelengths are enhanced only in one region, or half the total device area.

There are also a several mechanisms by which it will be possible to further improve the enhancements offered by this approach. By optimizing the feature sizes for specific colors, the PCs may be designed to better couple to the emission and excitation wavelengths of the desired QDs, increasing the local electric field within the PC, and thus the enhancement experienced in the QD output. This can also be accomplished by coupling QDs to only the TM mode, with higher Q-factor resonance conditions. In a 1D PC, the TM mode (which has electric field components in the x and z directions) can be isolated from the TE mode (with only y-directional electric field). However, in a 2D PC, the two polarizations cannot be separated and present as TE- and TM-like modes. These modes are similar to their 1D counterparts, with the TM-like mode occurring at a longer wavelength and having a narrower resonance than the TE-like mode, as shown in the band diagram in Figure 4.6.

In addition, the lattice structure in the PC has a dramatic effect on the possible enhancement, where square and hexagonal arrangements of circular cavities demonstrated enhancement factors of 100-200X. Specifically placing the QDs only in the PC pixel region where they would experience both excitation and extraction would decrease the quantities of QDs required and also extract light more effectively. With these improvements, it is likely that the PC enhancement would be even higher.

The devices in this work demonstrate the incorporation of QDs into a replica molded 2D PC. These structures have demonstrated combined excitation and extraction enhancements up to 5.8X output intensity. These structures also combine regions of PCs with different feature sizes, allowing different types of QDs to be embedded into the device and experiencing simultaneous enhancement from the same excitation source, but different extracted wavelengths. This creates a pixelated surface on a flexible substrate suitable for blending the color and directional output of multiple QD emission wavelengths for potential lighting or display applications.

4.5 Fabrication of photonic crystal with electrohydrodynamic jet printing

Due to high fabrication costs, there is a significant interest in improving the performance and efficiency of QDs within devices. In 1-D and 2-D PC slabs that serve as a quasi-planar device structure upon which QD-infused thin films can be readily applied, the optical coupling between PCs and QDs requires that the QDs reside within the resonant evanescent electric field volume, which decays exponentially away from the PC surface.[95] The evanescent field of a PC resonator extends from the PC surface and decreases to 1/e of the peak value at a depth ranging from 10% to 50% of the resonant wavelength. Therefore, for QDs designed to emit in the visible part of the optical spectrum, QDs should be located within a few hundred nanometers of the PC surface if they are to experience enhanced excitation and enhanced extraction. Methods used to apply QD-doped polymer thin films to PCs must therefore be capable of producing film thicknesses in the 10-500 nm range.

In our previous approach for QD-polymer thin film fabrication is spin coating, which results in substantial waste of QDs, because only a small fraction of the QD-polymer material is incorporated into the resulting thin film, while the remaining material is cast into the spinner bowl lining. Electrohydrodynamic jet (E-jet) printing is a recently developed approach for highly controlled spatial and volumetric deposition of liquids onto a variety of planar and nonplanar surfaces. E-jet printing uses a voltage difference between the printing nozzle and the substrate to create consistent, high resolution printed patterns (Figure 4.8).[96-98] E-jet printing has been used for semiconductor fabrication, biological sensing, and micro-optical devices.[99-100] QD-embedded polymer structures have been fabricated with ink jet printing for display applications, but E-jet printing is also capable of printing with multiple nozzles, and achieves finer resolution than ink jet printing, with features as small as 240 nm to 10 lm and linewidths as narrow as 25 nm.[101-105]

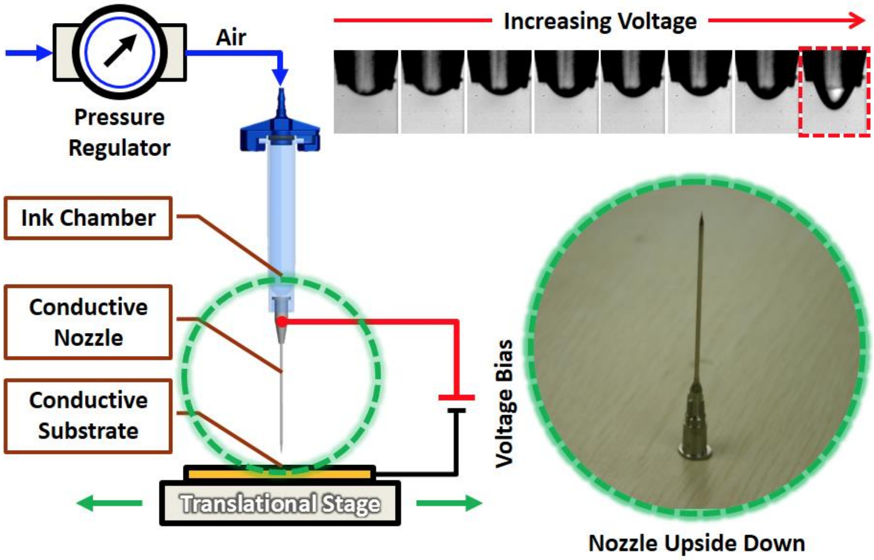

Figure 4.8 Schematic illustration of E-jet printing process.

In this continuation of previous work, we fabricated QD-embedded PCs by E-jet printing of a UV curable polymer onto a replica molding master and subsequent transfer to a substrate that supports the finished device structure. The QDs are placed inside the regions with the greatest electric field magnitude within the PC structure, resulting in a higher photon output than is produced without the PC structure. In addition, the targeted placement of the QDs to be in close proximity to the PC grating minimizes any QD emission outside the resonant evanescent field volume. The fabrication process was demonstrated in Figure 4.9. The PC structure consists of a linear grating formed by replica molding a polymer doped with QDs. The polymer mixture is E-jet printed over a master where the grating has a pitch of $\Lambda = 340$ nm with a 67% duty cycle and a depth $d = 120$ nm. The printed structure is then transferred to a plastic substrate, and a high refractive index layer of TiO_2 ($t = 105$ nm) is deposited over the surface of the polymer grating to create the periodic variation in the refractive index of the device.

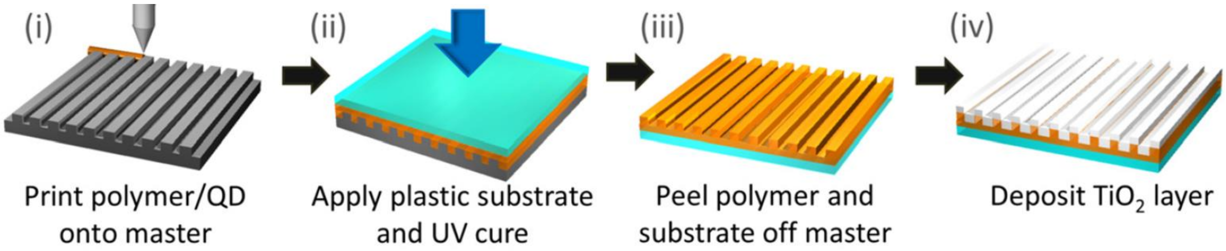

Figure 4.9 Photonic crystal fabrication process: (i) E-jet printing the QD embedded polymer over the silicon master, (ii) applying the plastic substrate and curing the polymer, (iii) peeling off the replica from the master, and (iv) depositing the TiO2 film over the cured polymer.

The E-jet printing process allows for precise placement of QDs on the PC patterned regions, to fabricate devices that show an 8X enhancement in output intensity. This capability is important in the context of creating a surface that contains an array of PCs in the form of red-green-blue emitting pixels, where individual PC regions may be optimized for a specific wavelength of QD emitter that would be selectively printed upon them. Figure 4.11 shows a fluorescence microscope image of the E-jet printed device. The top inset shows the clean edges printed by the system over the device regions. The bottom inset shows a duller edge where the printing was not perfectly aligned with the PC region. The fainter regions occur where there is no PC enhancement of the QD emission and show a clearly visible contrast in brightness between the planar region and the 8X enhancement provided by the PC structure, thus verifying the enhancement effect of the PC.

The enhanced emission is also polarized. The measured QD emission is shown for both the TM and TE polarizations in Figure 4.10 (a-b), respectively, where a polarizer has been added between the device and the measurement collection optics. The TM output intensity is 5X greater than the TE, and the TE output is comparable to the noise floor of the measurement system.

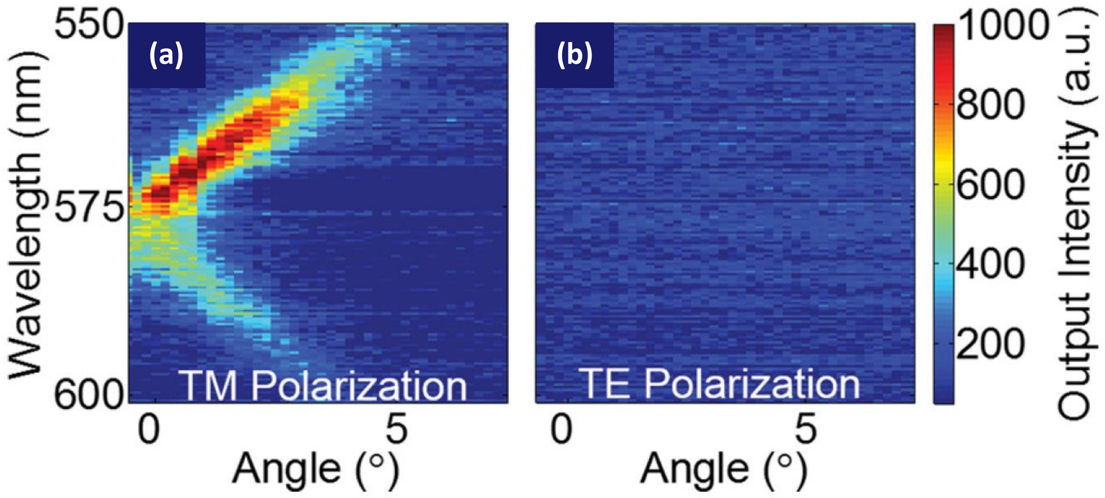

Figure 4.10 (a) TM and (b) TE polarized output from the PC figure. The TM polarized output demonstrates enhancement, while the output of the TE polarization is comparable to the measured background.

The E-jet printing process allows for precise placement of QDs on the PC patterned regions, to fabricate devices that show an 8X enhancement in output intensity. This capability is important in the context of creating a surface that contains an array of PCs in the form of red-green-blue emitting pixels, where individual PC regions may be optimized for a specific wavelength of QD emitter that would be selectively printed upon them. Figure 4.11 shows a fluorescence microscope image of the E-jet printed device. The top inset shows the clean edges printed by the system over the device regions. The bottom inset shows a duller edge where the printing was not perfectly aligned with the PC region. The fainter regions occur where there is no PC enhancement of the QD emission and show a clearly visible contrast in brightness between the planar region and the 8X enhancement provided by the PC structure, thus verifying the enhancement effect of the PC.

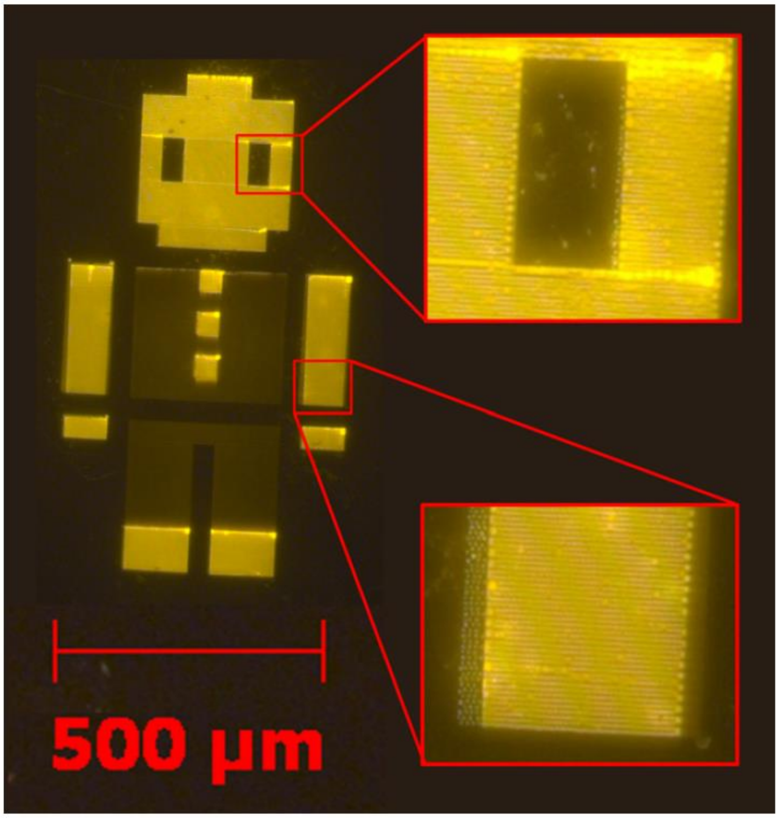

Figure 4.11 A fluorescence microscope image of the E-jet printed device.

The cost improvements offered by the use of E-jet printing are substantial. The precise placement of the QDs eliminates the waste of spin-casting or loading QDs into device regions where there is no need for emitters. In addition, the 600 nm film thickness, compared to the 8 µm thick layer produced with spin-casting, concentrates the emitters in the high enhancement regions of the photonic crystal and reduces the required volume of QD-polymer solution for the film by over 90%. There are minimal regions in which the QD emitters experience no enhancement and this drastically increases the total emission efficiency.

4.6 Future directions

Future devices may be designed to utilize a non- UV excitation source simply by adjusting the design parameters to couple to a different wavelength. Pixel patterning can also create regions with no PC structure at all, allowing only the excitation source light to pass through, thus increasing the flexibility of color mixing options for lighting.

The use of nanoreplica molding for fabrication makes it possible to scale up to large area fabrication on flexible substrates. With appropriate materials, large area, flexible displays and light sources can be constructed to use pixelated PC enhancement. The use of PCs in lighting and displays gives the advantage of angle steering possible with PC enhancement to broaden or narrow the output angles and control the directivity of light output in both lighting and displays. Polarization control is also possible with a PC, and could eliminate the 50% loss of backlight power by providing an initially polarized output in display technology.

The technological opportunities afforded by PCs combined with the levels of enhancement possible using QD-embedded PC devices may be a key enabler for the affordable incorporation of QDs into novel lighting and display applications. The enhancements require lower concentrations of QDs and could advance the color purity and performance of QD-based light sources toward consumer applications.

Future improvements for the E-jet printed device include increasing the printing speeds and printing red-green-blue specific device regions would improve the viability for scalable display production. If coupled with thin film transistors for switching, then E-jet printed PC regions would provide pixelated control of color and polarization for use in screen displays for computers, televisions, and other devices that require the high color purity of QDs.

CHAPTER 5: LED DISPLAY PIXEL CAVITY

This chapter proposes a new design architecture for backlit LED display devices that utilize a luminescent concentrator cavity to produce color output, where a QD-polymer thin film is surrounded by high reflective photonic mirror and sputtering silver, and the top surface is coated with black absorber with a small aperture. This pixel design eliminates the need for color filters and polarization filters, achieving high power conversion efficiency and high ambient contrast at the same time.

5.1 General introduction to LED display

While the advent of OLED devices has introduced attractive features to optical displays such as wide, vibrant color gamut and mechanical flexibility, LED-backlit LCD devices are less expensive and more reliable to produce, and therefore continue to dominate the color display market. Despite their competitive advantage, conventional LED displays are hampered by poor efficiencies and severe limitations to the accessible range of emitted colors. In order for LED-backlit displays to maintain their competitive advantage, new innovations must be pursued in order to improve their contrast, color gamut, and power consumption. The left schematic of Figure 5.1(a) illustrates a conventional LED-backlit display, which produces color by filtering white light through color filters placed on top of each sub-pixel. Devices utilizing white backlights with even the purest red, blue and green components, over two-thirds of the photons which transmit through the underlying LCD device are lost in each color filter. Figure 5.1(b) shows transmission profile of a commercial (CF-60 type) color filter used in optical displays. These color filters impose major limitations on the accessible color gamut and output efficiency. Additional losses reduce the overall light usages to only 6-7% for conventional displays, and as low as 4% for touch panel displays.

Each sub-pixel of a conventional LED-backlit liquid crystal display (LCD) contains a color filter to output either red, green or blue light. Each color filter eliminates 2-out-of-3 colors of the RGB spectrum, resulting in massive losses of optical intensity, which means the display requires more power.

Another main issues regarding LED-backlit display devices is their low ambient contrast. This issues is especially serious for mobile displays. When you try to look at the display screen under direct sunlight, the reflection intensity at each interfaces sum up to so high intensity that it overwhelms the display intensity. One solution to reduce the ambient contrast is by apply multiple circular polarizers to suppress ambient reflection (Figure 5.1(c)). But it would further reduce the display intensity of the LED backlight.

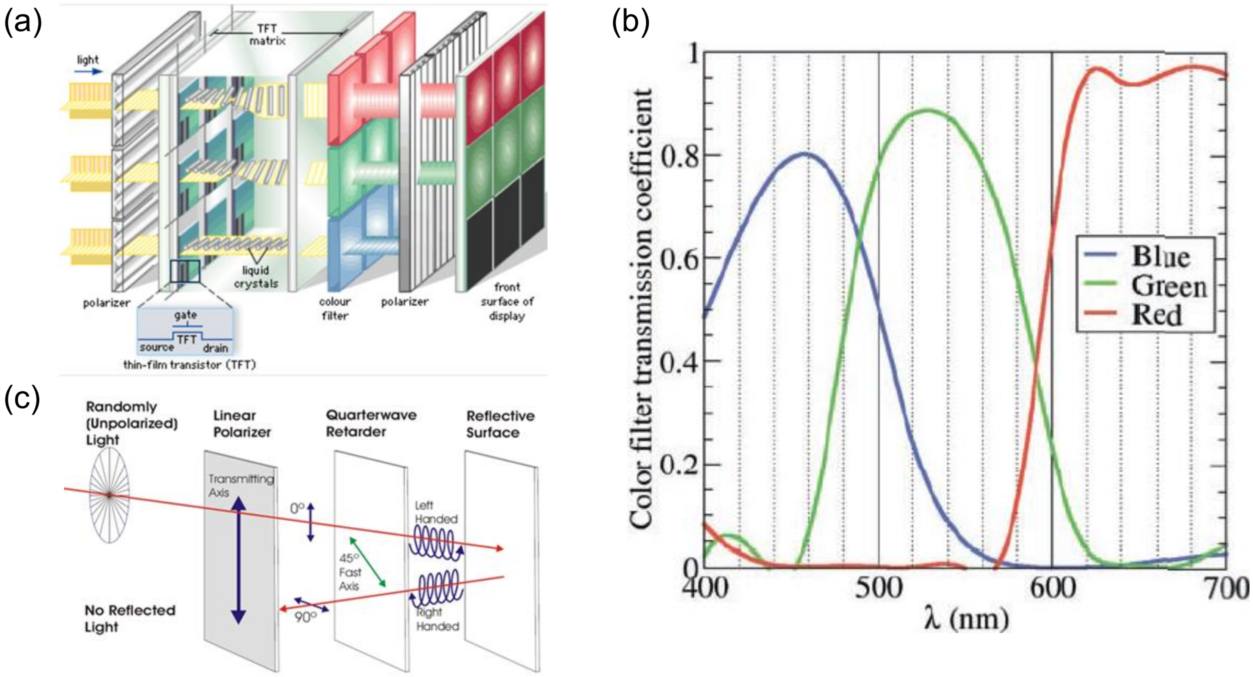

Figure 5.1 (a) Schematic illustrating the components of a conventional LCD device. Linear polarizers and color filters both result in significant loss of output. (b) Transmission profile of a commercial (CF-60 type) color filter used in optical displays. Even using a narrow linewidth light sources with equal distributions of red, green and blue, each color filter discards over two-thirds of incident light, resulting in major losses

Figure 5.1 (cont.)

of efficiency. (c) Schematic showing the function of circular polarizers in high ambient contrast optical displays. While a circular polarizer/quarterwave plate reduces back-reflection of ambient light, it also results in additional (≥50%) loss of output.

5.2 Pixel design

For decades, luminescent concentrators have been explored as a potential way to increase the output efficiency of solar cells. Here, we propose a novel optical display architecture that integrates a luminescent concentrator to achieve more efficient utilization of source light, and high ambient contrast without any need for circular polarizers.

The current design provides a new design architecture for backlit LCDs that uses a luminescent concentrator to produce color output. Our proposed design eliminates the need for color filters (which tend to be a major detriment to optical efficiencies in conventional backlit LCDs), and polarization filters used to enhance the ambient contrast as well as enable access to wider color gamut on par with emerging OLEO technologies. The combination of these attributes is very attractive as it reduces the required power, and improves the viewing experience. The concept is a new display design that can be formed using known materials.

The design is a luminescent concentrator waveguide and outcoupling device that emits narrow-linewidth visible light for pixelated displays from small openings in an otherwise black top surface. The salient features of the invention are luminescent materials (e.g. quantum dots or organic luminophores) and an optical microcavity containing high reflectivity mirrors and notch filters that prevent leakage of emitted light between sub-pixels.

As shown by the right schematic of Figure 5.2, our proposed design replaces traditional color filters with a luminescent concentrator micro-cavity, which is aligned directly above the top polarizer of an LCD panel. Each 25 µm by 25 µm sub-pixel contains a transparent polymer film embedded with quantum dots (QDs) that absorb photons from a single-wavelength (e.g. deep blue) source and emit light of a particular visible wavelength (such as green as shown in Figure 5.2). A combination of air gaps and high reflectivity mirrors create a cavity that concentrates the emitted light toward a small (4 µm diameter) outcoupler, which efficiently extracts light out the top of the device. A black absorber completely surrounds the outcoupler; the black absorber comprising 98% of the top surface area, resulting in high ambient contrast. Such a design may also find application for OLED displays, as it would eliminate the need for the circular polarizers required for such displays. The bottom DBR strongly reflects the emitted light from the QDs while acting as a deep-blue pass filter, thereby concentrating light towards the outcoupler and side mirrors, preventing leakage of light into adjacent sub-pixels. A green absorbing filter (not shown) will be added below the bottom DBR to minimize cross-talk between adjacent sub-pixels if green leakage through the bottom DBR is noticeable. We note that since the light in each subpixel will be produced by narrow linewidth QDs rather than a wide-band white light source, our design has the potential to achieve color gamut on par with emerging OLED displays.

We anticipate that the reflectivity values of the mirrors shown in Figure 5.2 (98% averaged all incident angles for the top DBR, 96% for the side silver mirrors, and 95% for the UV-pass DBR filter) are attainable through extensive research, and we note that the efficiency of the device shown can be improved even more by including air gaps on the top and bottom of the luminescent concentrator as well as by increasing the size of the outcoupler at the top. Finally, we also plan to explore methods of tapering the side edges of the luminescent concentrator as a potential route towards simplifying subsequent fabrication steps while potentially reducing losses through the edges of the device.

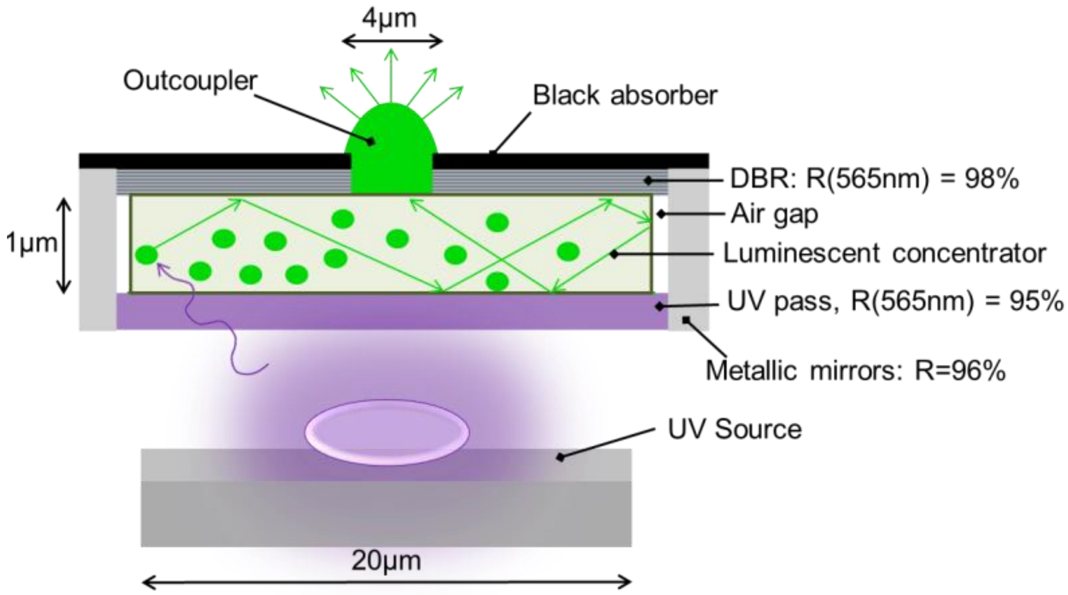

Figure 5.2 (a) Schematic of our proposed design for a green sub-pixel. The UV source backlight excites polymer embedded QD luminophores which emit light at visible wavelengths. The emitted light is concentrated, via reflections at the cavity edges, towards a 4 μm diameter outcoupler. 98% of the total top surface area is coated with a black absorber, resulting in a high ambient contrast with no need for circular polarizers.

5.3 Device fabrication

In order to demonstrate the feasibility of the pixel array design, we firstly fabricated a larger scale single pixel module for ease of measurement. Experimentally, the UV curable polymer, consisting of 91 μL of LMA and 9 μL of EGDMA, was mixed in a vial, and certain amount of QD hexane solution and 4 μL TOP was added and mixed well. The remaining solvent was removed by placing the vial inside the glovebox for several hours. Due to the low boiling point of hexane, the solvent will be fully evaporated without the use of rotavap. 0.05 μL of initiator (Darocur 1173) was added and mixed well with the solution. Then the solution was capillary filled between two quartz plate with 500 um spacers in between, then immediately polymerized by exposure to a high intensity UV lamp for 40 min inside glovebox.

The DBR mirror was purchased from Optical Filter Source, LLC (Austin, TX, USA). The aluminum cap was custom made by the machine shop at University of Illinois at Urbana-Champaign. The cap interior was then sputtered with 100 nm thick silver. The photographs of the silver coated cap and the fabricated QD-polymer slab are shown in Figure 5.3(b). The module was assembled by directly putting the QD-polymer slab on DBR with the cap on top. The 3D illustration graph of the final device is shown in Figure 5.3(a). The power conversion efficiency of the device was measured by placing the device at the front aperture of an integrating sphere, with the outcoupler side facing the integrating sphere. A 440 nm single wavelength light source was used to illuminate the whole polymer slab. The incident photon counts and QD emitted photon counts were collected to calculate the power conversion efficiency.

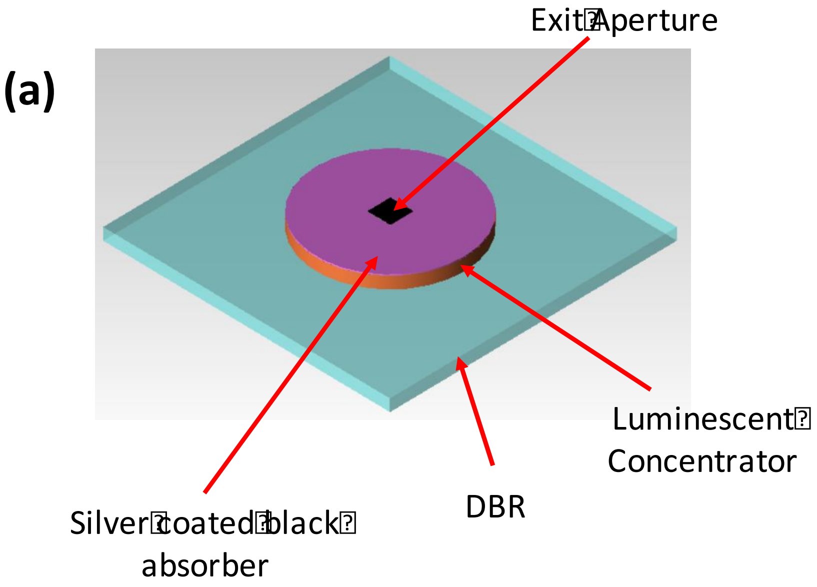

Figure 5.3

Figure 5.3 (cont.) (a) 3D schematic of the large scale pixel module. (b) Photograph of custom-made aluminum cap and QD-polymer slab.

5.4 Device performance

5.4.1 High reabsorption quantum dots

In this part of the project, we used commercial CdSeS/ZnS alloyed QDs from Sigma-Aldrich (Product #753785). The QDs are dissolved in toluene at 1 mg/mL concentration. The quantum yield of the QDs embedded in the polymer is 70%. We used these commercial QDs as the benchmark luminophores.

The power conversion efficiency measurement result is shown in Figure 5.4. In Figure 5.4(a), the source illumination without any samples or DBR is plotted in blue curve, and the source illumination with the device module in front of the integrating sphere is plotted in black curve. From the signals we can conclude that over 99.9% of the incident blue light is absorbed by the QDs, which eliminates the need for additional color filters to block the blue spectrum. The emission from QDs is shown in Figure 5.4(b), where the signal around 630 nm is purely coming from QDs emission, and it can be calculated that the power conversion efficiency is 17.7%. This number is already significantly higher than traditional display devices.

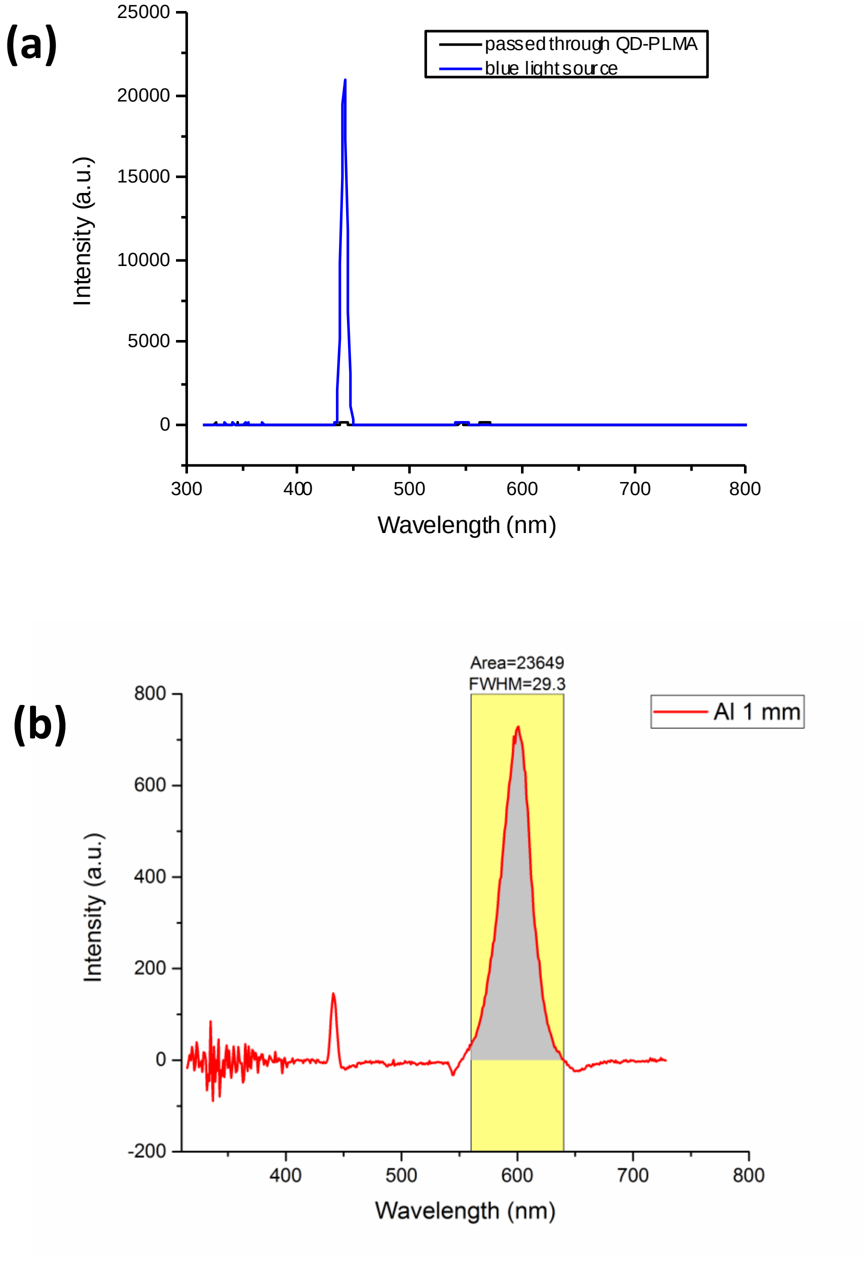

Figure 5.4 Power conversion efficiency measurement result. (a) Illumination source with and without sample. (b) QD emission when illuminated with blue light.

5.4.2 Low reabsorption quantum dots

Aside from commercial QDs, we also used self-synthesize CdSe/CdS QDs as luminophore materials. The structure of these QDs is tuned to suppress the CdSe absorption peak by growing much larger CdS shells. By comparing the absorption spectrum of the commercial and synthesized QDs in Figure 5.5, it is obvious that the synthesized QDs exhibit a much lower reabsorption. The quantum yield of these QDs is the same as commercial QDs (70%), which enables very good side-by-side comparison.

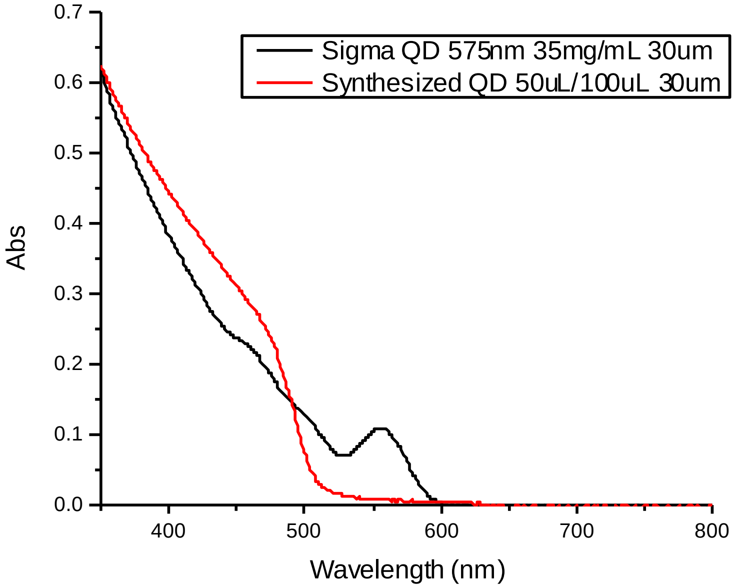

Figure 5.5 Absorption profile comparison between commercial QDs and synthesized QDs

The power conversion efficiency result is shown in Figure 5.6. The optical density of the synthesized QDs slab is kept the same as commercial QDs at 440 nm. First of all, we can see that there is minimal leakage of blue light at 440 nm, which means that the majority portion of the incident photons are absorbed by the QD-polymer layer. Secondly, the power conversion efficiency calculated here is as high as 34%, almost twice of the commercial QDs sample. Since absorption emission overlap is the only difference between the two samples, it is clear evidence that QDs reabsorption is a major factor in luminescent material performance.

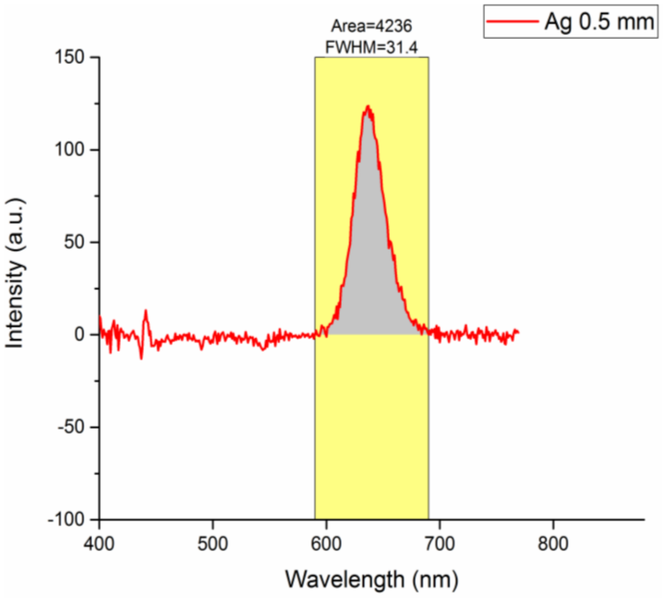

Figure 5.6 QD-polymer concentrating cavity emission by using synthesized QD.

5.5 Ray tracing simulation

In order to better understand the photon propagation behavior inside the device and provide insight into the designing rules, a Monte-Carlo ray tracing simulation program was developed. Monte-Carlo ray-tracing simulations have been previously shown to be accurate if accurate physical parameters are used.[106-107] In general, they are highly accurate and can model a wide variety of LSC shapes, sizes, and designs.

5.5.1 Simulation method

The method treats each incident photon as a classical geometric ray. At the scale we are interested in, wave optic effects are negligible. In addition, the incident light source is incoherent and so wave effects are minimized. The challenge, however, is in the treatment of absorption and fluorescence. As commercial, geometric ray tracing software does not emphasize fluorescent emission using any of those software packages would require introducing many light sources according to the incident photon distribution. So our Monte Carlo simulation code precisely traces each photon in a fashion similar to traditional ray tracing for reflection and refraction, but also allows for absorption and fluorescent emission inside the media. Additionally, instead of doing ray splitting at interfaces, a probability is given according to the reflection coefficient to determine if the ray is reflected or refracted to reduce the computational cost. This does not sacrifice accuracy, as the ensemble average of these probability reflections is effectively the same as ray splitting when the number of rays sampled is large. In the regime of ray optics, diffraction and interference are not considered. Since the purpose of this study is to understand and optimize solar concentrator design each ray is characterized with its starting location, propagation direction, and intensity.

Reflection off of a smooth surface is modeled using simple law of reflection. The field reflection coefficient r is calculated for perpendicular and parallel polarization respectively.

$$r_s = \frac{n_i cos\theta_i - n_i cos\theta_t}{n_i cos\theta_i + n_t cos\theta_t}$$

$$r_p = \frac{n_i cos\theta_t - n_t cos\theta_i}{n_i cos\theta_t + n_t cos\theta_i}$$

The subscript *i* refers to incident side and t refers to transmission side, and θ is the angle between the ray and interface norm. The amplitude reflection coefficient is the norm squared of the field reflection coefficient.

The propagation direction after reflection is determined by rotating the original direction 180° around the surface normal direction by the incidence angle. Refraction is modeled according to Snell's law.

$$\frac{sin\theta_1}{sin\theta_2} = \frac{n_2}{n_1}$$

Upon ray incidence onto a surface, a reflection coefficient R is calculated from the materials property at the interface, and then a random number is generated and compared with R. If it is greater than R the ray is transmitted and otherwise the ray is reflected.

In ray optics regime, absorption can be modeled as isotropic, uniformly distributed absorbers in a transparent matrix. The measured absorption and emission profiles of the luminophore are used as input parameters. After a photon is absorbed by a luminophore, the photon is excited into a higher energy state, and then relaxes to ground state via a number of channels, emitting a photon with a new random wavelength based on the emission profile of the fluorophore, and traveling in a new random direction. Due to the quantum yield being less than unity, a random number is introduced in the simulation to better represent the process. Every time a photon is absorbed by a luminophore, a random number between 0 and 1 is generated. And if the random number value is larger than 0.7, it means that the photon will not converted to low energy photon. On the other hand, if the value is equal to or smaller than 0.7, it means that the luminophore will emit a low energy photon. The wavelength at which the luminophore emits is determined by the input emission profile of the luminophore. For this study, Monte-Carlo ray-tracing simulations are performed by collecting statistics on large numbers of photons incident on the QD-polymer slab. The logic flow of the simulation is shown in Figure 5.7.

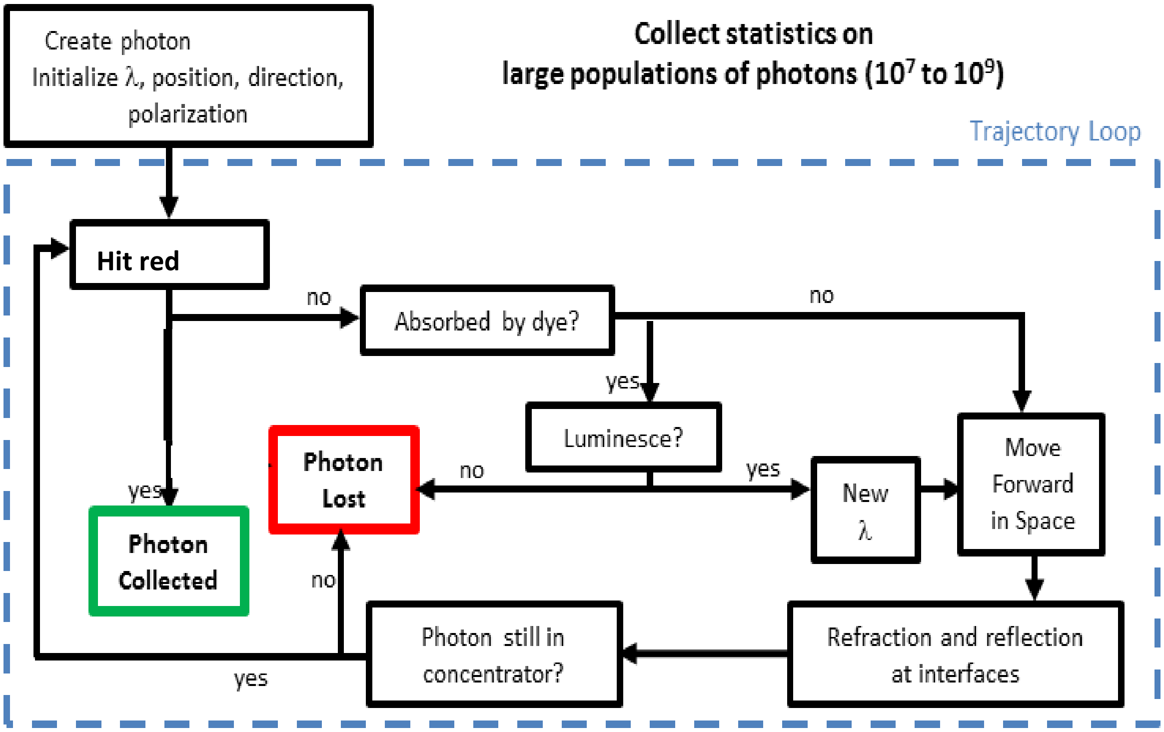

Figure 5.7 Trajectory loop of ray tracing simulation.

First of all, a photon is created immediately above the polymer sheet, with designated wavelength, position, direction and polarization. When the program starts, the photon starts moving directly downward into the sheet. The photon is moved forward 5.01 μm at a time, and then a series of checks are performed. The photon can be absorbed or scattered, and at every interface it can be reflected or refracted. Absorbed photons can be luminesced, or they can be lost to nonradiative events. As mentioned before, luminescence, scattering, and reflection are all treated probabilistically with a random number generator initiated to the computer epoch. The polarization of the photon is maintained until a scattering or luminescence event allows it to randomize. The checking loop stops only when this particular photon is collected or lost. And then the program moves on to the next photon. The overall efficiency of the device is calculated when all the photons have been analyzed. The size of the device is set as the same as experimental device (Figure 5.8). Photons are created at every point in a rectangular grid with 50 μm spacing. Additionally, every grid-point is populated with photons at 440 nm.

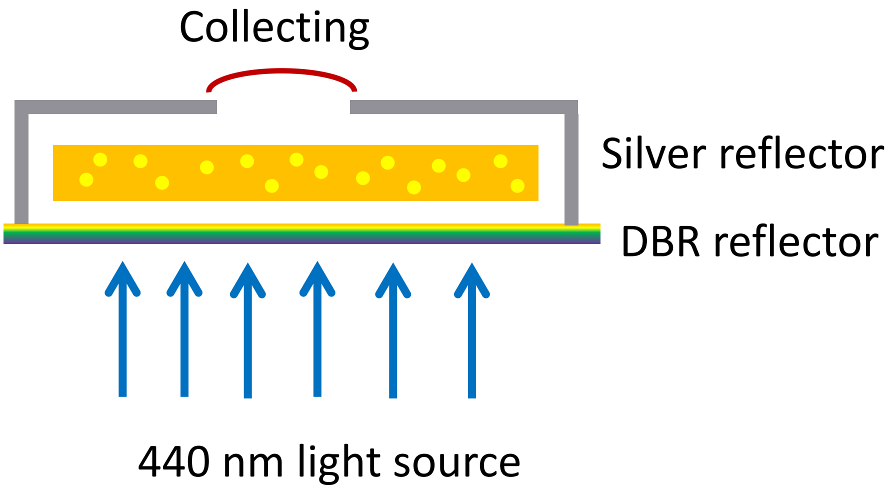

Figure 5.8 Schematic cross-section view of the device geometry in simulation.

5.5.2 Simulation results

The simulated typical spectrum output is shown in Figure 5.9(a). The illumination source is set as single wavelength (440 nm), thus displaying a single peak value. The QD emission very much resembles the experimental results. The simulated power conversion efficiency of the device varying the quantum yield value is shown in Figure 5.9(b). As we can see, at 70% quantum yield, the simulated efficiency is only several percent higher than experimental value. Considering the fact that the small defect in DBR mirror or silver mirror reflectivity is not accounted for in the simulation, the simulation result is very trustworthy. And if we extend the quantum yield both higher and lower, the curve exhibits an exponential function shape. It provided us with a clear route for higher device efficiency. If we could improve the quantum yield of the QDs from 70% up to 90%, then we could expect over 50% output efficiency.

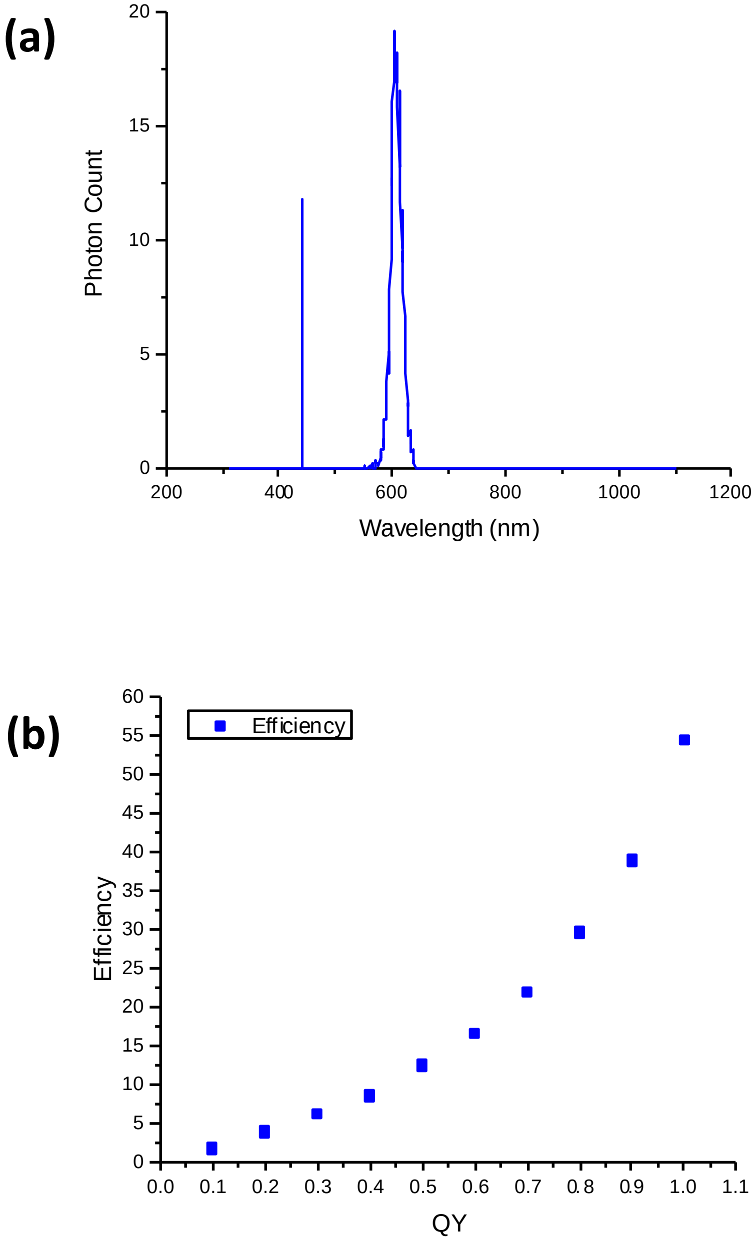

Figure 5.9 (a) Simulated spectrum with QD-polymer concentrating cavity module. (b) Simulated power conversion efficiency by varying quantum yield.

Another factor that is important in the performance if the concentrating device is the transparency of the polymer slab. In previous chapter, we have proved that scattering inside the polymer layer disrupts the TIR mode of the photon traveling inside, and diminishes the photon collection efficiency to the micron silicon solar cell embedded. However, in our pixel design, the goal is to extract more light out of the concentrating cavity towards the front outcoupler, thus it is potentially beneficial to introduce scattering inside the polymer to promote more light output. In order to test this theory, we tuned the scattering probability inside the polymer from 0 up to 0.01, and the result is shown is Figure 5.10. As we can see, when the scattering is relatively small, the output efficiency fluctuates on a very small scale, which means scattering doesn't affect the light extraction process. But when the scattering probability increases further, the efficiency drops significant to essentially negligible photon output. Similar to precious LSC simulation result, when scattering events happen frequently inside the polymer, photons are subjected to more loss mechanisms such as reabsorption, reflection and refraction. In conclusion, Monte-Carlo ray tracing simulation provides us with a functional tool for predicting device performance and optimizing device geometry and material designs.

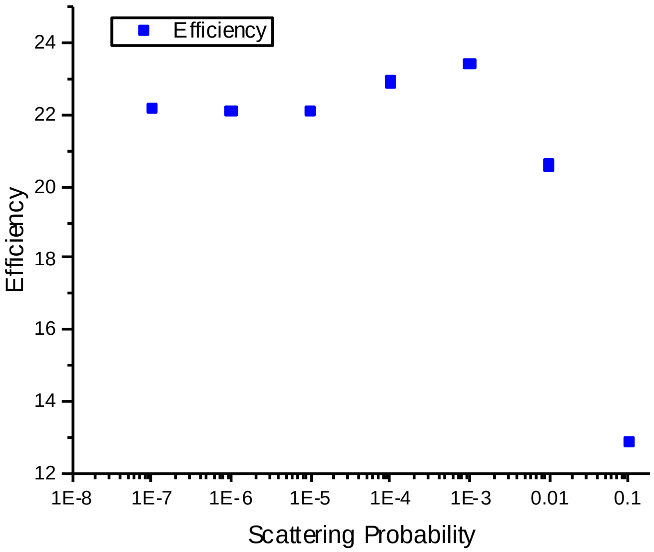

Figure 5.10 Simulated power conversion efficiency by varying scattering probability.

5.6 Future direction

In this part of work, we have successfully demonstrated the plausibility of designing such a pixel cavity to achieve high power conversion efficiency and high ambient contrast. Currently our experimental results were still collected with millimeter scale devices. Our future step will be focused on reducing device size to micron size, which is comparable to that of commercial display devices. One way to do so is to fabricate pixel arrays using photolithography method, creating a top cover with micron-sized aperture arrays (Figure 5.11).

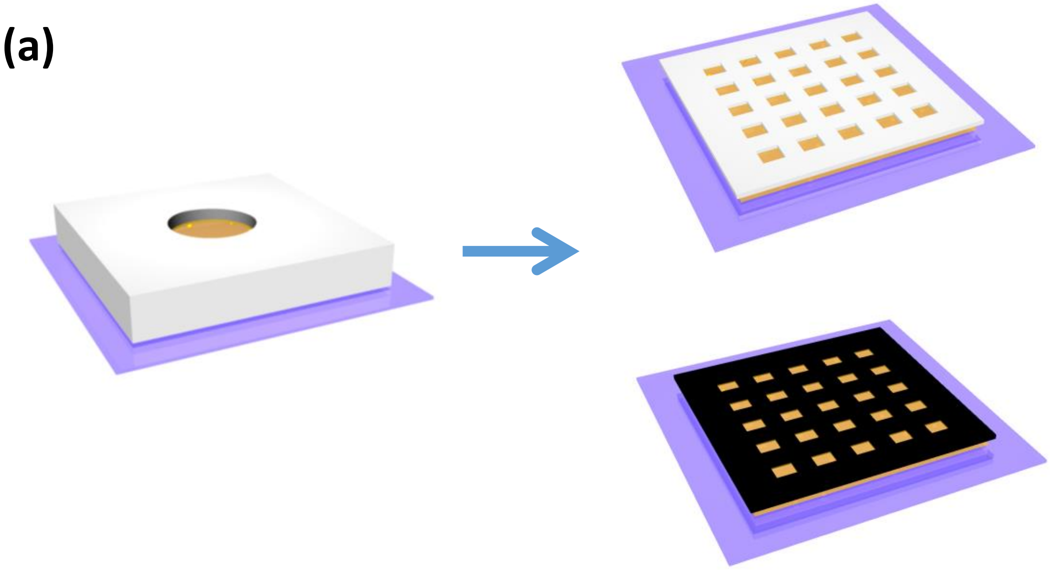

Figure 5.11

(b)

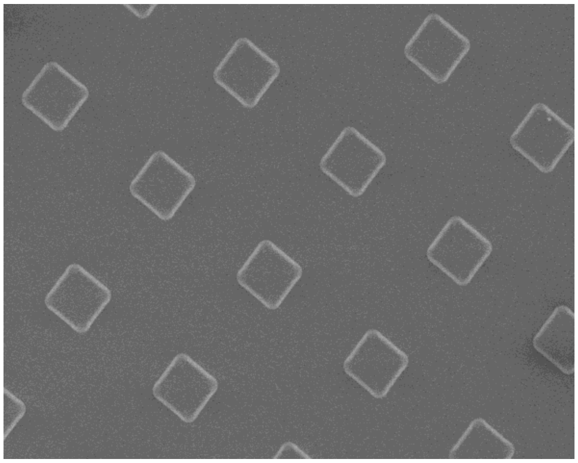

Figure 5.11 (cont.) (a) Schematic drawing of pixel arrays module. (b) SEM image of patterned silicon surface with 10 μm hole arrays.

CHAPTER 6: CONCLUDING REMARKS

With the advantage of a micro solar cell capable of being distributed into the LSC, dimensions on the order of a millimeter can be accessed to achieve optimal concentration ratio, while a millimeter sized LSC for a typical centimeter sized solar cell is incommensurate. A concentration ratio of 31 was demonstrated with a LSC device with DBR mirror, a result unprecedented in previous literature. Key parameters affecting LSC performance are identified and each investigated for their contribution. It is found that luminophore reabsorption plays a dominant role. It is concluded that to achieve higher concentration ratio, large Stokes shift is required, agreeing with previously developed theory according to thermodynamics by E. Yablonovitch.

There are additional aspects that could be explored to further optimize the system. The micro solar cells studied in this work were silicon solar cells. It is possible to achieve higher efficiency both from the micro solar cell itself and the concentrators, by using a higher efficiency material such as GaAs. For a high concentration ratio especially, the quality of the solar cell is more important. For a low concentration ratio, silicon PV is good candidate. Another area of improvement is the design of DBR to better match the absorption and emission profile of QDs.

For QDs or nanorods, there are great opportunities to explore other luminophores that cover a broader spectral range than the CdSe/CdS structure, yet still maintain a large Stokes shift. One possible pair of materials is PbSe/PdS and InCuP/ZnS. Current materials that absorb in the visible and emit in the NIR all suffer from stability issues. With advancements in this area possible in the future, a LSC or LED using more optimized quantum dots could achieve large improvements in terms of collector efficiency.

REFERENCES

1. Ashoori, R. C., Electrons in artificial atoms. *Nature* **1996,** *379* (6564), 413-419.

2. Ornes, S., Core Concept: Quantum dots. *Proceedings of the National Academy of Sciences of the United States of America* **2016,** *113* (11), 2796-2797.

3. and, C. B. M.; Kagan, C. R.; Bawendi, M. G., Synthesis and Characterization of Monodisperse Nanocrystals and Close-Packed Nanocrystal Assemblies. *Annual Review of Materials Science* **2000,** *30* (1), 545-610.

4. Alivisatos, A. P., Perspectives on the Physical Chemistry of Semiconductor Nanocrystals. *The Journal of Physical Chemistry* **1996,** *100* (31), 13226-13239.

5. Alivisatos, A. P., Semiconductor Clusters, Nanocrystals, and Quantum Dots. *Science* **1996,** *271* (5251), 933-937.

6. Yoffe, A. D., Semiconductor quantum dots and related systems: Electronic, optical, luminescence and related properties of low dimensional systems. *Advances in Physics* **2001,** *50* (1), 1-208.

7. Coe-Sullivan, S.; Steckel, J. S.; Woo, W. K.; Bawendi, M. G.; Bulović, V., Large-Area Ordered Quantum-Dot Monolayers via Phase Separation During Spin-Casting. *Advanced Functional Materials* **2005,** *15* (7), 1117-1124.

8. Zhao, Y.; Burda, C., Development of plasmonic semiconductor nanomaterials with copper chalcogenides for a future with sustainable energy materials. *Energy & Environmental Science* **2012,** *5* (2), 5564-5576.

9. Medintz, I. L.; Uyeda, H. T.; Goldman, E. R.; Mattoussi, H., Quantum dot bioconjugates for imaging, labelling and sensing. *Nat Mater* **2005,** *4* (6), 435-446.

10. Chapin, D. M.; Fuller, C. S.; Pearson, G. L., A New Silicon p-n Junction Photocell for Converting Solar Radiation into Electrical Power. *Journal of Applied Physics* **1954,** *25* (5), 676-677.

11. Shockley, W.; Queisser, H. J., Detailed Balance Limit of Efficiency of p-n Junction Solar Cells. *Journal of Applied Physics* **1961,** *32* (3), 510-519.

12. Kim, D.-H.; Ahn, J.-H.; Choi, W. M.; Kim, H.-S.; Kim, T.-H.; Song, J.; Huang, Y. Y.; Liu, Z.; Lu, C.; Rogers, J. A., Stretchable and Foldable Silicon Integrated Circuits. *Science* **2008,** *320* (5875), 507-511.

13. Mack, S.; Meitl, M. A.; Baca, A. J.; Zhu, Z.-T.; Rogers, J. A., Mechanically flexible thin-film transistors that use ultrathin ribbons of silicon derived from bulk wafers. *Applied Physics Letters* **2006,** *88* (21), 213101.

14. Meitl, M. A.; Zhu, Z.-T.; Kumar, V.; Lee, K. J.; Feng, X.; Huang, Y. Y.; Adesida, I.; Nuzzo, R. G.; Rogers, J. A., Transfer printing by kinetic control of adhesion to an elastomeric stamp. *Nat Mater* **2006,** *5* (1), 33-38.

15. Shurcliff, W. A., Radiance Amplification by Multi-Stage Fluorescence System. *J. Opt. Soc. Am.* **1951,** *41* (3), 209-209.

16. Goetzberger, A.; Greube, W., Solar energy conversion with fluorescent collectors. *Applied physics* **1977,** *14* (2), 123-139.

17. Batchelder, J. S.; Zewai, A. H.; Cole, T., Luminescent solar concentrators. 1: Theory of operation and techniques for performance evaluation. *Appl. Opt.* **1979,** *18* (18), 3090-3110.

18. Batchelder, J. S.; Zewail, A. H.; Cole, T., Luminescent solar concentrators. 2: Experimental and theoretical analysis of their possible efficiencies. *Appl. Opt.* **1981,** *20* (21), 3733-3754.

19. Weber, W. H.; Lambe, J., Luminescent greenhouse collector for solar radiation. *Appl. Opt.* **1976,** *15* (10), 2299-2300.

20. Yablonovitch, E., Thermodynamics of the fluorescent planar concentrator. *J. Opt. Soc. Am.* **1980,** *70* (11), 1362-1363.

21. Smestad, G.; Ries, H.; Winston, R.; Yablonovitch, E., The thermodynamic limits of light concentrators. *Solar Energy Materials* **1990,** *21* (2), 99-111.

22. Debije, M. G.; Verbunt, P. P. C., Thirty Years of Luminescent Solar Concentrator Research: Solar Energy for the Built Environment. *Advanced Energy Materials* **2012,** *2* (1), 12-35.

23. Chatten, A. J.; Barnham, K. W. J.; Buxton, B. F.; Ekins-Daukes, N. J.; Malik, M. A., A new approach to modelling quantum dot concentrators. *Solar Energy Materials and Solar Cells* **2003,** *75* (3–4), 363-371.

24. Earp, A. A.; Smith, G. B.; Franklin, J.; Swift, P., Optimisation of a three-colour luminescent solar concentrator daylighting system. *Solar Energy Materials and Solar Cells* **2004,** *84* (1–4), 411-426.

25. Slooff, L. H.; Bende, E. E.; Burgers, A. R.; Budel, T.; Pravettoni, M.; Kenny, R. P.; Dunlop, E. D.; Büchtemann, A., A luminescent solar concentrator with 7.1% power conversion efficiency. *physica status solidi (RRL) – Rapid Research Letters* **2008,** *2* (6), 257-259.

26. Yoon, J.; Li, L.; Semichaevsky, A. V.; Ryu, J. H.; Johnson, H. T.; Nuzzo, R. G.; Rogers, J. A., Flexible concentrator photovoltaics based on microscale silicon solar cells embedded in luminescent waveguides. *Nature Communications* **2011,** *2*, 343.

27. Semichaevsky, A. V.; Johnson, H. T.; Yoon, J.; Nuzzo, R. G.; Li, L.; Rogers, J., Theory for optimal design of waveguiding light concentrators in photovoltaic microcell arrays. *Appl. Opt.* **2011,** *50* (17), 2799-2808.

28. Bomm, J.; Büchtemann, A.; Chatten, A. J.; Bose, R.; Farrell, D. J.; Chan, N. L. A.; Xiao, Y.; Slooff, L. H.; Meyer, T.; Meyer, A.; van Sark, W. G. J. H. M.; Koole, R., Fabrication and full characterization of state-of-the-art quantum dot luminescent solar concentrators. *Solar Energy Materials and Solar Cells* **2011,** *95* (8), 2087-2094.

29. Hyldahl, M. G.; Bailey, S. T.; Wittmershaus, B. P., Photo-stability and performance of CdSe/ZnS quantum dots in luminescent solar concentrators. *Solar Energy* **2009,** *83* (4), 566-573.

30. Pal, B. N.; Ghosh, Y.; Brovelli, S.; Laocharoensuk, R.; Klimov, V. I.; Hollingsworth, J. A.; Htoon, H., 'Giant' CdSe/CdS Core/Shell Nanocrystal Quantum Dots As Efficient Electroluminescent Materials: Strong Influence of Shell Thickness on Light-Emitting Diode Performance. *Nano Letters* **2012,** *12* (1), 331-336.

31. Chen, O.; Zhao, J.; Chauhan, V. P.; Cui, J.; Wong, C.; Harris, D. K.; Wei, H.; Han, H.-S.; Fukumura, D.; Jain, R. K.; Bawendi, M. G., Compact high-quality CdSe–CdS core–shell nanocrystals with narrow emission linewidths and suppressed blinking. *Nat Mater* **2013,** *12* (5), 445-451.

32. Lee, J.; Sundar, V. C.; Heine, J. R.; Bawendi, M. G.; Jensen, K. F., Full Color Emission from II–VI Semiconductor Quantum Dot–Polymer Composites. *Advanced Materials* **2000,** *12* (15), 1102-1105.

33. Bomm, J.; Büchtemann, A.; Fiore, A.; Manna, L.; Nelson, J. H.; Hill, D.; van Sark, W. G. J. H. M., Fabrication and spectroscopic studies on highly luminescent CdSe/CdS nanorod polymer composites. *Beilstein Journal of Nanotechnology* **2010,** *1*, 94-100.

34. Yoon, J.; Baca, A. J.; Park, S.-I.; Elvikis, P.; Geddes, J. B.; Li, L.; Kim, R. H.; Xiao, J.; Wang, S.; Kim, T.-H.; Motala, M. J.; Ahn, B. Y.; Duoss, E. B.; Lewis, J. A.; Nuzzo, R. G.; Ferreira, P. M.; Huang, Y.; Rockett, A.; Rogers, J. A., Ultrathin silicon solar microcells for semitransparent, mechanically flexible and microconcentrator module designs. *Nat Mater* **2008,** *7* (11), 907-915.

35. Yao, Y.; Brueckner, E.; Li, L.; Nuzzo, R., Fabrication and assembly of ultrathin high-efficiency silicon solar microcells integrating electrical passivation and anti-reflection coatings. *Energy & Environmental Science* **2013,** *6* (10), 3071-3079.

36. Reisfeld, R.; Shamrakov, D.; Jorgensen, C., Photostable solar concentrators based on fluorescent glass films. *Solar Energy Materials and Solar Cells* **1994,** *33* (4), 417-427.

37. Sheng, X.; Shen, L.; Kim, T.; Li, L.; Wang, X.; Dowdy, R.; Froeter, P.; Shigeta, K.; Li, X.; Nuzzo, R. G.; Giebink, N. C.; Rogers, J. A., Doubling the Power Output of Bifacial Thin-Film GaAs Solar Cells by Embedding Them in Luminescent Waveguides. *Advanced Energy Materials* **2013,** *3* (8), 991-996.

38. Bronstein, N. D.; Li, L.; Xu, L.; Yao, Y.; Ferry, V. E.; Alivisatos, A. P.; Nuzzo, R. G., Luminescent Solar Concentration with Semiconductor Nanorods and Transfer-Printed Micro-Silicon Solar Cells. *ACS Nano* **2014,** *8* (1), 44-53.

39. McDowall, S.; Butler, T.; Bain, E.; Scharnhorst, K.; Patrick, D., Comprehensive analysis of escape-cone losses from luminescent waveguides. *Appl. Opt.* **2013,** *52* (6), 1230-1239.

40. Peters, M.; Goldschmidt, J. C.; Löper, P.; Bläsi, B.; Gombert, A., The effect of photonic structures on the light guiding efficiency of fluorescent concentrators. *Journal of Applied Physics* **2009,** *105* (1), 014909.

41. Giebink, N. C.; Wiederrecht, G. P.; Wasielewski, M. R., Resonance-shifting to circumvent reabsorption loss in luminescent solar concentrators. *Nat Photon* **2011,** *5* (11), 694-701.

42. Erickson, C. S.; Bradshaw, L. R.; McDowall, S.; Gilbertson, J. D.; Gamelin, D. R.; Patrick, D. L., Zero-Reabsorption Doped-Nanocrystal Luminescent Solar Concentrators. *ACS Nano* **2014,** *8* (4), 3461-3467.

43. Meinardi, F.; Colombo, A.; Velizhanin, K. A.; Simonutti, R.; Lorenzon, M.; Beverina, L.; Viswanatha, R.; Klimov, V. I.; Brovelli, S., Large-area luminescent solar concentrators based on /`Stokes-shift-engineered/' nanocrystals in a mass-polymerized PMMA matrix. *Nat Photon* **2014,** *8* (5), 392-399.

44. Coropceanu, I.; Bawendi, M. G., Core/Shell Quantum Dot Based Luminescent Solar Concentrators with Reduced Reabsorption and Enhanced Efficiency. *Nano Letters* **2014,** *14* (7), 4097-4101.

45. Bradshaw, L. R.; Knowles, K. E.; McDowall, S.; Gamelin, D. R., Nanocrystals for Luminescent Solar Concentrators. *Nano Letters* **2015,** *15* (2), 1315-1323.

46. Meinardi, F.; McDaniel, H.; Carulli, F.; Colombo, A.; Velizhanin, K. A.; Makarov, N. S.; Simonutti, R.; Klimov, V. I.; Brovelli, S., Highly efficient large-area colourless luminescent solar concentrators using heavy-metal-free colloidal quantum dots. *Nat Nano* **2015,** *10* (10), 878-885.

47. Goldschmidt, J. C.; Peters, M.; Gutmann, J.; Steidl, L.; Zentel, R.; Bläsi, B.; Hermle, M. In *Increasing fluorescent concentrator light collection efficiency by restricting the angular emission characteristic of the incorporated luminescent material: the 'Nano-Fluko' concept*, 2010; pp 77250S-77250S-11.

48. Rau, U.; Einsele, F.; Glaeser, G. C., Efficiency limits of photovoltaic fluorescent collectors. *Applied Physics Letters* **2005,** *87* (17), 171101.

49. Goldschmidt, J. C.; Peters, M.; Prönneke, L.; Steidl, L.; Zentel, R.; Bläsi, B.; Gombert, A.; Glunz, S.; Willeke, G.; Rau, U., Theoretical and experimental analysis of photonic structures for fluorescent concentrators with increased efficiencies. *physica status solidi (a)* **2008,** *205* (12), 2811-2821.

50. Peters, M.; Goldschmidt, J. C.; Löper, P.; Groß, B.; Üpping, J.; Dimroth, F.; Wehrspohn, R.; Bläsi, B., Spectrally-Selective Photonic Structures for PV Applications. *Energies* **2010,** *3* (2), 171.

51. Nina, P. M. H.; Ilja, S.; Alexandre, T.; Dick, K. G. d. B., Light Polarization by Cholesteric Layers. *Japanese Journal of Applied Physics* **2003,** *42* (8R), 5189.

52. Jeong, S. M.; Sonoyama, K.; Takanishi, Y.; Ishikawa, K.; Takezoe, H.; Nishimura, S.; Suzaki, G.; Song, M. H., Optical cavity with a double-layered cholesteric liquid crystal mirror and its prospective application to solid state laser. *Applied Physics Letters* **2006,** *89* (24), 241116.

53. Jeong, S. M.; Takanishi, Y.; Ishikawa, K.; Nishimura, S.; Suzaki, G.; Takezoe, H., Sharply directed emission in microcavity organic light-emitting diodes with a cholesteric liquid crystal film. *Optics Communications* **2007,** *273* (1), 167-172.

54. de Boer, D. K. G.; Lin, C.-W.; Giesbers, M. P.; Cornelissen, H. J.; Debije, M. G.; Verbunt, P. P. C.; Broer, D. J., Polarization-independent filters for luminescent solar concentrators. *Applied Physics Letters* **2011,** *98* (2), 021111.

55. Ng, H. M.; Moustakas, T. D.; Chu, S. N. G., High reflectivity and broad bandwidth AlN/GaN distributed Bragg reflectors grown by molecular-beam epitaxy. *Applied Physics Letters* **2000,** *76* (20), 2818-2820.

56. Wu, Z.; Lee, D.; Rubner, M. F.; Cohen, R. E., Structural Color in Porous, Superhydrophilic, and Self-Cleaning SiO2/TiO2 Bragg Stacks. *Small* **2007,** *3* (8), 1445-1451.

57. Colodrero, S.; Ocaña, M.; Míguez, H., Nanoparticle-Based One-Dimensional Photonic Crystals. *Langmuir* **2008,** *24* (9), 4430-4434.

58. Gonzalez-Garcia, L.; Lozano, G.; Barranco, A.; Miguez, H.; Gonzalez-Elipe, A. R., TiO2-SiO2 one-dimensional photonic crystals of controlled porosity by glancing angle physical vapour deposition. *Journal of Materials Chemistry* **2010,** *20* (31), 6408-6412.

59. Gunning, W. J.; Hall, R. L.; Woodberry, F. J.; Southwell, W. H.; Gluck, N. S., Codeposition of continuous composition rugate filters. *Appl. Opt.* **1989,** *28* (14), 2945-2948.

60. Abu-Safia, H. A.; Al-Sharif, A. I.; Abu Aljarayesh, I. O., Rugate filter sidelobe suppression using half-apodization. *Appl. Opt.* **1993,** *32* (25), 4831-4835.

61. Lee, C.-C.; Tang, C.-J.; Wu, J.-Y., Rugate filter made with composite thin films by ion-beam sputtering. *Appl. Opt.* **2006,** *45* (7), 1333-1337.

62. Nolte, A. J.; Rubner, M. F.; Cohen, R. E., Creating Effective Refractive Index Gradients within Polyelectrolyte Multilayer Films: Molecularly Assembled Rugate Filters. *Langmuir* **2004,** *20* (8), 3304-3310.

63. Lorenzo, E.; Oton, C. J.; Capuj, N. E.; Ghulinyan, M.; Navarro-Urrios, D.; Gaburro, Z.; Pavesi, L., Porous silicon-based rugate filters. *Appl. Opt.* **2005,** *44* (26), 5415-5421.

64. Kosten, E. D.; Kayes, B. M.; Atwater, H. A., Experimental demonstration of enhanced photon recycling in angle-restricted GaAs solar cells. *Energy & Environmental Science* **2014,** *7* (6), 1907-1912.

65. de Boer, D. K. G. In *Optimizing wavelength-selective filters for luminescent solar concentrators*, 2010; pp 77250Q-77250Q-9.

66. Goldschmidt, J. C.; Peters, M.; Bösch, A.; Helmers, H.; Dimroth, F.; Glunz, S. W.; Willeke, G., Increasing the efficiency of fluorescent concentrator systems. *Solar Energy Materials and Solar Cells* **2009,** *93* (2), 176-182.

67. Slooff, L. H.; Burgers, A. R.; Debije, M. G. In *Reduction of escape cone losses in luminescent solar concentrators with cholesteric mirrors*, 2008; pp 704306-704306-7.

68. Debije, M. G.; Van, M.-P.; Verbunt, P. P. C.; Kastelijn, M. J.; van der Blom, R. H. L.; Broer, D. J.; Bastiaansen, C. W. M., Effect on the output of a luminescent solar concentrator on application of organic wavelength-selective mirrors. *Appl. Opt.* **2010,** *49* (4), 745-751.

69. Puzzo, D. P.; Bonifacio, L. D.; Oreopoulos, J.; Yip, C. M.; Manners, I.; Ozin, G. A., Color from colorless nanomaterials: Bragg reflectors made of nanoparticles. *Journal of Materials Chemistry* **2009,** *19* (21), 3500-3506.

70. Yang, W.; Liu, Z.; Chen, J.; Huang, L.; Zhang, L.; Pan, H.; Wu, B.; Lin, Y., A high-performance white-light-emitting-diodes based on nano-single crystal divanadates quantum dots. *Scientific Reports* **2015,** *5*, 10460.

71. Woo, J. Y.; Kim, K.; Jeong, S.; Han, C.-S., Enhanced Photoluminance of Layered Quantum Dot–Phosphor Nanocomposites as Converting Materials for Light Emitting Diodes. *The Journal of Physical Chemistry C* **2011,** *115* (43), 20945-20952.

72. Song, W.-S.; Yang, H., Efficient White-Light-Emitting Diodes Fabricated from Highly Fluorescent Copper Indium Sulfide Core/Shell Quantum Dots. *Chemistry of Materials* **2012,** *24* (10), 1961-1967.

73. Moazzam, A.; Soma, C.; Angshuman, N.; Akshay, K.; Sameer, S.; Chakraborty, S.; Sarma, D. D., White-light emission from a blend of CdSeS nanocrystals of different Se:S ratio. *Nanotechnology* **2007,** *18* (7), 075401.

74. Yablonovitch, E., Inhibited Spontaneous Emission in Solid-State Physics and Electronics. *Physical Review Letters* **1987,** *58* (20), 2059-2062.

75. John, S., Strong localization of photons in certain disordered dielectric superlattices. *Physical Review Letters* **1987,** *58* (23), 2486-2489.

76. Ganesh, N.; Zhang, W.; Mathias, P. C.; Chow, E.; Soares, J. A. N. T.; Malyarchuk, V.; Smith, A. D.; Cunningham, B. T., Enhanced fluorescence emission from quantum dots on a photonic crystal surface. *Nat Nano* **2007,** *2* (8), 515-520.

77. Boroditsky, M.; Vrijen, R.; Krauss, T. F.; Coccioli, R.; Bhat, R.; Yablonovitch, E., Spontaneous Emission Extraction and Purcell Enhancement from Thin-Film 2-D Photonic Crystals. *J. Lightwave Technol.* **1999,** *17* (11), 2096.

78. Hessel, A.; Oliner, A. A., A New Theory of Wood's Anomalies on Optical Gratings. *Appl. Opt.* **1965,** *4* (10), 1275-1297.

79. Ding, Y.; Magnusson, R., Band gaps and leaky-wave effects in resonant photonic-crystal waveguides. *Opt. Express* **2007,** *15* (2), 680-694.

80. Ding, Y.; Magnusson, R., Resonant leaky-mode spectral-band engineering and device applications. *Opt. Express* **2004,** *12* (23), 5661-5674.

81. Magnusson, R.; Wang, S. S., New principle for optical filters. *Applied Physics Letters* **1992,** *61* (9), 1022-1024.

82. Rippa, M.; Capasso, R.; Mormile, P.; De Nicola, S.; Zanella, M.; Manna, L.; Nenna, G.; Petti, L., Bragg extraction of light in 2D photonic Thue-Morse quasicrystals patterned in active CdSe/CdS nanorod-polymer nanocomposites. *Nanoscale* **2013,** *5* (1), 331-336.

83. Kodali, A. K.; Schulmerich, M.; Ip, J.; Yen, G.; Cunningham, B. T.; Bhargava, R., Narrowband Midinfrared Reflectance Filters Using Guided Mode Resonance. *Analytical Chemistry* **2010,** *82* (13), 5697-5706.

84. Ganesh, N.; Block, I. D.; Mathias, P. C.; Zhang, W.; Chow, E.; Malyarchuk, V.; Cunningham, B. T., Leaky-mode assisted fluorescence extraction: application to fluorescence enhancement biosensors. *Opt. Express* **2008,** *16* (26), 21626-21640.

85. Herrnsdorf, J.; Guilhabert, B.; McKendry, J. J. D.; Gong, Z.; Massoubre, D.; Zhang, S.; Watson, S.; Kelly, A. E.; Gu, E.; Laurand, N.; Dawson, M. D., Hybrid organic/GaN photonic crystal light-emitting diode. *Applied Physics Letters* **2012,** *101* (14), 141122.

86. Cho, K.-S.; Lee, E. K.; Joo, W.-J.; Jang, E.; Kim, T.-H.; Lee, S. J.; Kwon, S.-J.; Han, J. Y.; Kim, B.-K.; Choi, B. L.; Kim, J. M., High-performance crosslinked colloidal quantum-dot light-emitting diodes. *Nat Photon* **2009,** *3* (6), 341-345.

87. Elison, M.; Claude, W., Impact of photonic crystals on LED light extraction efficiency: approaches and limits to vertical structure designs. *Journal of Physics D: Applied Physics* **2010,** *43* (35), 354005.

88. McGroddy, K.; David, A.; Matioli, E.; Iza, M.; Nakamura, S.; DenBaars, S.; Speck, J. S.; Weisbuch, C.; Hu, E. L., Directional emission control and increased light extraction in GaN photonic crystal light emitting diodes. *Applied Physics Letters* **2008,** *93* (10), 103502.

89. Khokhar, A. Z.; Parsons, K.; Hubbard, G.; Watson, I. M.; Rahman, F.; Macintyre, D. S.; Xiong, C.; Massoubre, D.; Gong, Z.; Gu, E.; Johnson, N. P.; De La Rue, R. M.; Dawson, M. D.; Abbott, S. J.; Charlton, M. D. B.; Tillin, M., Emission characteristics of photonic crystal light-emitting diodes. *Appl. Opt.* **2011,** *50* (19), 3233-3239.

90. Englund, D.; Fattal, D.; Waks, E.; Solomon, G.; Zhang, B.; Nakaoka, T.; Arakawa, Y.; Yamamoto, Y.; Vučković, J., Controlling the Spontaneous Emission Rate of Single Quantum Dots in a Two-Dimensional Photonic Crystal. *Physical Review Letters* **2005,** *95* (1), 013904.

91. Yang, F.; Cunningham, B. T., Enhanced quantum dot optical down-conversion using asymmetric 2D photonic crystals. *Opt. Express* **2011,** *19* (5), 3908-3918.

92. Barth, M.; Gruber, A.; Cichos, F., Spectral and angular redistribution of photoluminescence near a photonic stop band. *Physical Review B* **2005,** *72* (8), 085129.

93. Petti, L.; Rippa, M.; Zhou, J.; Manna, L.; Zanella, M.; Mormile, P., Novel hybrid organic/inorganic 2D quasiperiodic PC: from diffraction pattern to vertical light extraction. *Nanoscale Research Letters* **2011,** *6* (1), 371.

94. Diana, F. S.; David, A.; Meinel, I.; Sharma, R.; Weisbuch, C.; Nakamura, S.; Petroff, P. M., Photonic Crystal-Assisted Light Extraction from a Colloidal Quantum Dot/GaN Hybrid Structure. *Nano Letters* **2006,** *6* (6), 1116-1120.

95. Ganesh, N.; Mathias, P. C.; Zhang, W.; Cunningham, B. T., Distance dependence of fluorescence enhancement from photonic crystal surfaces. *Journal of Applied Physics* **2008,** *103* (8), 083104.

96. Sutanto, E.; Tan, Y.; Onses, M. S.; Cunningham, B. T.; Alleyne, A., Electrohydrodynamic jet printing of micro-optical devices. *Manufacturing Letters* **2014,** *2* (1), 4-7.

97. Park, J.-U.; Hardy, M.; Kang, S. J.; Barton, K.; Adair, K.; Mukhopadhyay, D. k.; Lee, C. Y.; Strano, M. S.; Alleyne, A. G.; Georgiadis, J. G.; Ferreira, P. M.; Rogers, J. A., High-resolution electrohydrodynamic jet printing. *Nat Mater* **2007,** *6* (10), 782-789.

98. Mishra, S.; Barton, K. L.; Alleyne, A. G.; Ferreira, P. M.; Rogers, J. A., High-speed and drop-on-demand printing with a pulsed electrohydrodynamic jet. *Journal of Micromechanics and Microengineering* **2010,** *20* (9), 095026.

99. Onses, M. S.; Song, C.; Williamson, L.; Sutanto, E.; Ferreira, P. M.; Alleyne, A. G.; Nealey, P. F.; Ahn, H.; Rogers, J. A., Hierarchical patterns of three-dimensional block-copolymer films formed by electrohydrodynamic jet printing and self-assembly. *Nat Nano* **2013,** *8* (9), 667-675.

100. Shigeta, K.; He, Y.; Sutanto, E.; Kang, S.; Le, A.-P.; Nuzzo, R. G.; Alleyne, A. G.; Ferreira, P. M.; Lu, Y.; Rogers, J. A., Functional Protein Microarrays by Electrohydrodynamic Jet Printing. *Analytical Chemistry* **2012,** *84* (22), 10012-10018.

101. Wood, V.; Panzer, M. J.; Chen, J.; Bradley, M. S.; Halpert, J. E.; Bawendi, M. G.; Bulović, V., Inkjet-Printed Quantum Dot–Polymer Composites for Full-Color AC-Driven Displays. *Advanced Materials* **2009,** *21* (21), 2151-2155.

102. Khan, A.; Rahman, K.; Kim, D. S.; Choi, K. H., Direct printing of copper conductive micro-tracks by multi-nozzle electrohydrodynamic inkjet printing process. *Journal of Materials Processing Technology* **2012,** *212* (3), 700-706.

103. Sutanto, E.; Shigeta, K.; Kim, Y. K.; Graf, P. G.; Hoelzle, D. J.; Barton, K. L.; Alleyne, A. G.; Ferreira, P. M.; Rogers, J. A., A multimaterial electrohydrodynamic jet (E-jet) printing system. *Journal of Micromechanics and Microengineering* **2012,** *22* (4), 045008.

104. Barton, K.; Mishra, S.; Alex Shorter, K.; Alleyne, A.; Ferreira, P.; Rogers, J., A desktop electrohydrodynamic jet printing system. *Mechatronics* **2010,** *20* (5), 611-616.

105. Kim, B. H.; Onses, M. S.; Lim, J. B.; Nam, S.; Oh, N.; Kim, H.; Yu, K. J.; Lee, J. W.; Kim, J.-H.; Kang, S.-K.; Lee, C. H.; Lee, J.; Shin, J. H.; Kim, N. H.; Leal, C.; Shim, M.; Rogers, J. A., High-Resolution Patterns of Quantum Dots Formed by Electrohydrodynamic Jet Printing for Light-Emitting Diodes. *Nano Letters* **2015,** *15* (2), 969-973.

106. Earp, A. A.; Smith, G. B.; Swift, P. D.; Franklin, J., Maximising the light output of a Luminescent Solar Concentrator. *Solar Energy* **2004,** *76* (6), 655-667.

107. Chatten, A. J.; Barnham, K. W. J.; Buxton, B. F.; Ekins-Daukes, N. J.; Malik, M. A., Quantum dot solar concentrators. *Semiconductors* **2004,** *38* (8), 909-917.